

**THREE-DIMENSIONAL INTEGRAL
IMAGING BASED CAPTURE AND DISPLAY
SYSTEM USING DIGITAL
PROGRAMMABLE FRESNEL LENSLET
ARRAYS**

A DISSERTATION SUBMITTED TO
THE DEPARTMENT OF ELECTRICAL AND ELECTRONICS
ENGINEERING
AND THE GRADUATE SCHOOL OF ENGINEERING AND SCIENCE
OF BILKENT UNIVERSITY
IN PARTIAL FULFILLMENT OF THE REQUIREMENTS
FOR THE DEGREE OF
DOCTOR OF PHILOSOPHY

By
Ali Özgür YÖNTEM
December, 2012

I certify that I have read this thesis and that in my opinion it is fully adequate, in scope and in quality, as a dissertation for the degree of Doctor of Philosophy.

Prof. Dr. Levent ONURAL(Advisor)

I certify that I have read this thesis and that in my opinion it is fully adequate, in scope and in quality, as a dissertation for the degree of Doctor of Philosophy.

Assoc. Prof. Dr. Hilmi Volkan DEMİR

I certify that I have read this thesis and that in my opinion it is fully adequate, in scope and in quality, as a dissertation for the degree of Doctor of Philosophy.

Assoc. Prof. Dr. Uğur GÜDÜKBAY

I certify that I have read this thesis and that in my opinion it is fully adequate, in scope and in quality, as a dissertation for the degree of Doctor of Philosophy.

Prof. Dr. Enis ÇETİN

I certify that I have read this thesis and that in my opinion it is fully adequate, in scope and in quality, as a dissertation for the degree of Doctor of Philosophy.

Prof. Dr.Hakan ÜREY

Approved for the Graduate School of Engineering and Science:

Prof. Dr. Levent Onural
Director of the Graduate School

ABSTRACT

THREE-DIMENSIONAL INTEGRAL IMAGING BASED CAPTURE AND DISPLAY SYSTEM USING DIGITAL PROGRAMMABLE FRESNEL LENSLET ARRAYS

Ali Özgür YÖNTEM

PhD. in Electrical and Electronics Engineering

Supervisor: Prof. Dr. Levent ONURAL

December, 2012

A Fresnel lenslet array pattern is written on a phase-only LCoS spatial light modulator device (SLM) to replace the regular analog lenslet array in a conventional integral imaging system. We theoretically analyze the capture part of the proposed system based on Fresnel wave propagation formulation. Due to pixelation and quantization of the lenslet array pattern, higher diffraction orders and multiple focal points emerge. Because of the multiple focal planes introduced by the discrete lenslets, multiple image planes are observed. The use of discrete lenslet arrays also causes some other artefacts on the recorded elemental images. The results reduce to those available in the literature when the effects introduced by the discrete nature of the lenslets are omitted. We performed simulations of the capture part. It is possible to obtain the elemental images with an acceptable visual quality. We also constructed an optical integral imaging system with both capture and display parts using the proposed discrete Fresnel lenslet array written on a SLM. Optical results, when self-luminous objects, such as an LED array, are used indicate that the proposed system yields satisfactory results. The resulting system consisting of digital lenslet arrays offers a flexible integral imaging system. Thus, to increase the visual performance of the system, previously available analog solutions can now be implemented digitally by using electro-optical devices. We also propose a method and present applications of this method that converts a diffraction pattern into an elemental image set in order to display them on a display-only integral imaging setup. We generate elemental images based on diffraction calculations as an alternative to commonly used ray tracing methods. Ray tracing methods do not accommodate the interference and diffraction phenomena. Our proposed method enables us to obtain elemental images from a holographic recording of a 3D object/scene. The diffraction pattern can be either numerically generated or digitally acquired from optical input. The

method shows the connection between a hologram (diffraction pattern) of a 3D object and an elemental image set of the same 3D object. We obtained optical reconstructions with a display-only integral imaging setup where we used a digital lenslet array. We also obtained numerical reconstructions, again by using the diffraction calculations, for comparison. The digital and optical reconstruction results are in good agreement. Finally, we showed a method to obtain an orthoscopic image of a 3D object. We converted an elemental image set that gives real pseudoscopic reconstruction into another elemental image set that gives real orthoscopic reconstruction. Again, we used wave propagation simulations for this purpose. We also demonstrated numerical and optical reconstructions from the obtained elemental image sets for comparison. The results are satisfactory given the physical limitations of the display system.

Keywords: Imaging systems, multiple imaging, three-dimensional image acquisition.

ÖZET

SAYISAL PROGRAMLANABİLİR FRESNEL MERCEKCİK DİZİLERİNİN KULLANILDIĞI İNTEGRAL GÖRÜNTÜLEME TABANLI ÜÇ-BOYUTLU GÖRÜNTÜ ÇEKİM VE GÖSTERİM SİSTEMİ

Ali Özgür YÖNTEM

Elektrik ve Elektronik Mühendisliği, Doktora

Tez Yöneticisi: Prof. Dr. Levent ONURAL

Aralık, 2012

Geleneksel integral görüntüleme sistemlerinde analog mercekcik dizileri kullanılır. Biz analog mercekcik dizileri yerine, ışığın yalnızca evresini değiştirebilen silikon üzerine sıvı kristal uzamsal ışık modülatörüne yazılmış sayısal Fresnel mercekcik dizisi örüntüsü kullandık. Böylece, önerilen sistemin çekim kısmını Fresnel dalga yayılımı ilintisi kullanarak kuramsal olarak çözümledik. Çözümün sonuçları, mercekcik dizisi örüntüsünün pikselizasyonuna ve nicemlendirilmesine bağlı olarak, yüksek kırınım basamaklarının ve çoklu odak noktalarının ortaya çıktığını gösteriyor. Ayrık mercekciklerin neden olduğu çoklu odak düzlemlerinden dolayı, çoklu görüntü düzlemleri gözlenmektedir. Ayrıca bu mercekcik dizileri, kaydedilen imgecikler üzerinde başka bozulmalara da neden olmaktadır. Bu mercekciklerin kullanımından doğan etkiler ihmal edildiğinde, sonuçlar literatürde bulunanlara indirgenmektedir. Görüntü çekim kısmının benzetimlerini gerçekleştirdik. İmgecikleri, kabul edilebilir görüntü kalitesinde elde etmek mümkün olduğu görülüyor. Belirtilen ayrık mercekcik dizisini hem çekim hem de gösterim kısımlarında kullanarak, görünür ışıkta çalışan bir integral görüntüleme sistemi de kurduk. Kurulan bu sistemde, ışıklı cisimler (örneğin bir LED dizisi) kullanılarak görünür ışıkta tatmin edici sonuçlar elde ettik. Ayrık mercekcik dizisinden oluşan bu yeni sistem, integral görüntüleme sistemlerine esneklik getirmektedir. Böylece, sistemin görsel performansını artırmak için, daha önceki analog çözümler şimdi elektro-optik aygıtlarla sayısal olarak daha kolay gerçekleştirilebilecektir. Bir kırınım örüntüsünü, bir imgecik kümesine çeviren bir yöntem ve bu yöntemin uygulamalarını da inceledik. Belirtilen yöntemi kullanarak, kırınım örüntüsünden elde edilen imgecik kümelerini bir integral görüntü

gösterim düzeneğine yazarak 3B görüntü elde ettik. Imgecik kümeleri, genellikle ışın izleme yöntemi kullanılarak elde edilir. Biz ise, buna bir alternatif olarak, imgecikleri kırınım hesaplayarak elde ediyoruz. Işın izleme yöntemleri, ışığın girişimi ve kırınımı olgularını gösteremezler. Önerdiğimiz bu yöntem, 3B bir cismin veya sahnenin görünür ışıktaki holografik kaydından, imgeciklerini elde etmemize olanak sağlamaktadır. Kırınım örüntüsü sayısal olarak üretilmiş ya da görünür ışıktaki sayısal olarak çekilmiş veriler olabilir. Bu yöntem, 3B bir cismin hologram (kırınım örüntüsü) ile aynı cismin bir imgecik kümesi arasındaki bağıntıyı göstermektedir. Sayısal mercekcik dizisi ile çalışan bir integral görüntü gösterim düzeneğinde, geriçatımlar elde ettik. Karşılaştırma amacıyla, yine kırınım hesaplamaları kullanarak, sayısal geriçatımlar da elde ettik. Sayısal ve optik geriçatım sonuçlarının birbirleri ile uyumlu olduğu gözlemlendi. Son olarak, 3B bir cismin ortoskopik derinlik görüntüsü veren görüntü geriçatımını elde etmek için başka bir yöntem daha geliştirdik. Bu yöntem ile, yalnız derinlik görüntüsü veren (psedoskopik) geriçatım oluşturan bir imgecik kümesini, ortoskopik geriçatım oluşturan başka bir imgecik kümesine çevirdik. Yine, bu amaçla dalga yayılımı benzetimlerini kullandık. Sayısal ve görünür ışıktaki geriçatım sonuçlarını da karşılaştırdık. Sonuçların kalitesinin, görüntüleme sisteminin fiziksel sınırları dahilinde, yeterli olduğu gözlemlendi.

Anahtar sözcükler: Görüntüleme sistemleri, çoklu görüntüleme, üç-boyutlu görüntü çekimi.

Acknowledgement

“Our whole universe was in a hot dense state, then nearly fourteen billion years ago expansion started. Wait... The Earth began to cool, the autotrophs began to drool, Neanderthals developed tools. We built a wall (we built the pyramids). Math, science, history, unraveling the mysteries, That all started with the big bang!”

Well yes, everything has started with the Big Bang. However, this study of mine is sparkled with the dream when I was a little kid that I can build something like in the Star Wars movie. When I first saw R2D2, “a long time ago in a galaxy far, far away”, projecting the hologram of Princess Leia I was amazed by the “fictitious” technology which George Lucas made popular. The dream continued when I was watching the cartoon series where there was the holographic assistant “Jarvis” of Tony Stark, who is also known as Iron Man. Finally, the technology became so popular that it is used almost in every science fiction based cartoons and films. So, first of all I should thank those people who inspired our childhood with science fiction. The fictitious thoughts now became the actual science. Since it is a continuing process like passing of the Olympics fire from hand-to-hand, each era influenced the proceeding one. So, I should also thank Galileo, Kepler, Leonardo da Vinci, Jules Verne, Wheatstone, Rayleigh, Einstein, Gabor and many others...

It was not an easy decision for me that if I should take the “Stairway to Academia” or continue with the “Highway to Private Companies” after I got my B.S. I give my sincere thanks to my supervisor Prof. Dr. Levent Onural for his advices, so that, I chose to continue to study on my childhood dream. I also thank him for endless discussions on our studies and guidance on me. I thank my instructors, who will be my colleagues from now on but always be advisors for me, Prof. Dr. Orhan Arıkan, Assoc. Prof. Hilmi Volkan Demir, Assoc. Prof. Uğur Güdükbay.

During my studies, I realized that “one does not simply walk into life. Its closed gates hide more than just small surprises. The future is uncertain that

you cannot foresee anything, and the Great Eye is ever watchful. It is a barren wasteland, riddled with fire and ash and dust, the very air you breathe is a poisonous fume”. Well, Boromir of Tolkien may not be talking of the future and I might have rephrased some of these words but our journey in life is not much different from the journey of “Frodo the ring bearer”. We should walk through these wastelands of life before we finally accomplish something in life and face lots of difficulties. At this point, I should thank my parents, Necmettin and Naciye, that they gave all their love and support during my life and especially “in my time of need” during my university life. I feel grateful if my presence helped even a little bit to my father in the heaven to ease his pain during his fight against ALS, which is also known as Lou Gehrig’s disease. I think at least I had the chance to show my gratitude to him even if there is nothing to stop the decease. And there is my sister, Özlem, who had thanked me in her M.S. thesis for my assistance as “very special thanks to”, especially with the good old Pentium 166 MMX PC. I think this is my time to thank (payback:)) her, for her endless support.

During this journey called “life”, no matter how hard it is, it is good to know that I have fellows standing by me to carry this burden. I want to thank my friends who supported me for all these years. There are those, who are like blood brothers to me, I had the bond through FRP games. I have Okan “Olath the Ranger”, Özgün “Narth Velard the Paladin”, Berkay “Xfel the Thief” and our Okan with the new alias “Tank”, and there is also Murat “the Barbarian of Diablo”. I always loved to play as a Wizard with them, and now I think, I am a *contemporary wizard of the universe: an engineer* with a PhD degree! I thank the James Cook crew that they stand as a beacon at the coordinates $N39^{\circ}54'40.5''E32^{\circ}51'23.4''$ and helped my navigation. I also thank many other friends and also my colleagues in the department which I have not mentioned here name by name. However, they are already in my Facebook friendlist:)

All of these are so “preciousss” to me! “May the force be with you” all!

I would like to thank the Department of Electrical and Electronics Engineering at Bilkent University for their support throughout my thesis study. This work is supported by EC within FP6 under Grant 511568 with acronym 3DTV and

within FP7 under Grant 216105 with the acronym Real 3D. I also would like to thank TÜBİTAK (The Scientific and Technological Research Council of Turkey) for the financial support.

Contents

1	INTRODUCTION	1
2	PRELIMINARIES: SAMPLING OF DIFFRACTION FIELD AND DIGITAL FRESNEL LENS ARRAYS	13
2.1	Discrete Quadratic Phase Array Patterns	18
2.2	Multiple Focal Points	21
2.3	Numerical Results	29
3	ANALYSIS OF INTEGRAL IMAGING CAPTURE SYSTEM WITH DIGITAL LENS ARRAY	42
3.1	Capture System Analysis	42
3.2	Display System	49
3.3	Optical Results	49
4	DISPLAY OF HOLOGRAPHIC RECORDING USING INTEGRAL IMAGING SYSTEM WITH DIGITAL LENS ARRAY	58
4.1	The Method	59

<i>CONTENTS</i>	xii
4.2 The Algorithm	63
4.3 The Examples	66
4.4 The Optical Setup	77
4.5 Numerical and Optical Results	80
5 OBTAINING ORTHOSCOPIC ELEMENTAL IMAGES FROM PSEUDOSCOPIC ELEMENTAL IMAGES	92
5.1 The Pseudoscopic-Orthoscopic Conversion Method	92
5.2 Examples and Results	95
6 CONCLUSIONS	98
BIBLIOGRAPHY	102
APPENDICES	110
A Evaluation of Eq. (2.16)	110
B Evaluation of Eq. (3.6)	113
C Derivation of 1D impulse response of the LSI system that repre- sents free-space propagation between two parallel planes	117

List of Figures

2.1	Calculation of the diffraction field of a sliced 3D field.	14
2.2	3×5 Lenslet array phase profile on the SLM, each lens has $f = 43.3mm$. There are equal number of unused pixels both at left and right edges. (Reprinted from “Integral imaging using phase-only LCoS spatial light modulators as Fresnel lenslet arrays,” Ali Özgür Yöntem and L. Onural, J. Opt. Soc. Am. A vol. 28, no. 11, pp.2359-2375, 2011. ©2011 OSA.)	24
2.3	Illustration of a quadratic phase function and its sampled and quantized version. Vertical axis shows the phase, mod 2π , while the horizontal axis shows the spatial extent of the function. (Revised from “Integral imaging using phase-only LCoS spatial light modulators as Fresnel lenslet arrays,” Ali Özgür Yöntem and L. Onural, J. Opt. Soc. Am. A vol. 28, no. 11, pp.2359-2375, 2011. ©2011 OSA.)	25

- 2.4 Multiple focal points and higher diffraction orders. The focal points are shown by small circles. Dashed lines show the converging waves towards multiple focal points from a single lenslet. Solid lines show the converging waves towards higher diffraction orders at the fundamental focal plane. (Not all lines are shown in order not to clutter the drawing.) (Reprinted from “Integral imaging using phase-only LCoS spatial light modulators as Fresnel lenslet arrays,” Ali Özgür Yöntem and L. Onural, *J. Opt. Soc. Am. A* vol. 28, no. 11, pp.2359-2375, 2011. ©2011 OSA.) 28
- 2.5 Pixelated and quantized lens with $f = 14.4mm$. Sampling period is $8\mu m$, $\lambda = 532nm$ and array dimension is 120×120 pixels. (Reprinted from “Integral imaging using phase-only LCoS spatial light modulators as Fresnel lenslet arrays,” Ali Özgür Yöntem and L. Onural, *J. Opt. Soc. Am. A* vol. 28, no. 11, pp.2359-2375, 2011. ©2011 OSA.) 33
- 2.6 Magnitude square of the cross-section of the field due to the pixelated and quantized lenslet, with $f = 14.4mm$, under plane wave illumination. The SLM is on the left. The bright areas indicate the multiple focal points and higher diffraction orders. The brightest area on the right is the fundamental focal point. (For visual purposes, we adjusted the brightness of the figure.) (Reprinted from “Integral imaging using phase-only LCoS spatial light modulators as Fresnel lenslet arrays,” Ali Özgür Yöntem and L. Onural, *J. Opt. Soc. Am. A* vol. 28, no. 11, pp.2359-2375, 2011. ©2011 OSA.) 34
- 2.7 Sampled lens with $f = 43.3mm$. Sampling period is $8\mu m$, $\lambda = 532nm$ and array dimension is 360×360 pixels. (Reprinted from “Integral imaging using phase-only LCoS spatial light modulators as Fresnel lenslet arrays,” Ali Özgür Yöntem and L. Onural, *J. Opt. Soc. Am. A* vol. 28, no. 11, pp.2359-2375, 2011. ©2011 OSA.) 35

- 2.8 Magnitude square of the cross-section of the field due to the pixelated and quantized lenslet, with $f = 43.3mm$, under plane wave illumination. The bright areas indicate the multiple focal points and higher diffraction orders. The brightest area on the right is the fundamental focal point. (For visual purposes, we adjusted the brightness of the figure.) (Reprinted from “Integral imaging using phase-only LCoS spatial light modulators as Fresnel lenslet arrays,” Ali Özgür Yöntem and L. Onural, J. Opt. Soc. Am. A vol. 28, no. 11, pp.2359-2375, 2011. ©2011 OSA.) 36
- 2.9 Array of lenslets consisting of pixelated lenslets with $f = 14.4mm$. Total array size is 360×360 pixels. Each lenslet in the array has the same properties defined as in Fig. 2.5. The array can be obtained either by replicating a single lenslet in both directions or by intentionally introducing an aliasing in the calculation of a pattern for an array with dimensions having 360×360 pixels and a focal length of $14.4mm$. (Reprinted from “Integral imaging using phase-only LCoS spatial light modulators as Fresnel lenslet arrays,” Ali Özgür Yöntem and L. Onural, J. Opt. Soc. Am. A vol. 28, no. 11, pp.2359-2375, 2011. ©2011 OSA.) 37
- 2.10 Magnitude square of the cross-section of the field due to the array of lenslets consisting of sampled lenslets, with $f = 14.4mm$, under plane wave illumination. Bright areas indicate the multiple focal points and higher diffraction orders. The brightest areas on the right are the fundamental focal points corresponding to each lenslet. (For visual purposes, we adjusted the brightness of the figure.) (Reprinted from “Integral imaging using phase-only LCoS spatial light modulators as Fresnel lenslet arrays,” Ali Özgür Yöntem and L. Onural, J. Opt. Soc. Am. A vol. 28, no. 11, pp.2359-2375, 2011. ©2011 OSA.) 38

2.11 Image of the absolute value of $d_3[\mathbf{n}]$. There are nine elemental images due to nine lenslets of the letter “A”. There is a background noise due to the random phase on the input mask plus the out of focus images introduced the multiple focal length properties of the lenslets. The noise do not effect the images’ visibility too much. (For visual purposes, we adjusted the brightness of the figure.) (Reprinted from “Integral imaging using phase-only LCoS spatial light modulators as Fresnel lenslet arrays,” Ali Özgür Yöntem and L. Onural, J. Opt. Soc. Am. A vol. 28, no. 11, pp.2359-2375, 2011. ©2011 OSA.) 39

2.12 Image of the absolute value of $d_4[\mathbf{n}]$. The elemental images, which are depicted inside the rectangles, of the letter “A” are seen together with the higher diffraction orders between the elemental images. A zoomed in version of the central elemental image is given in Fig. 2.13. We observe a similar background noise. However, the visibility of elemental images are now degraded significantly due to the noise. This is because of the smaller size elemental images with less power. (For visual purposes, we adjusted the brightness of the figure.) (Reprinted from “Integral imaging using phase-only LCoS spatial light modulators as Fresnel lenslet arrays,” Ali Özgür Yöntem and L. Onural, J. Opt. Soc. Am. A vol. 28, no. 11, pp.2359-2375, 2011. ©2011 OSA.) 40

2.13 (a) Zoomed in elemental image corresponding to the central part of Fig. 2.12. (b) Zoomed in elemental image corresponding to the image right to the central part of Fig. 2.12. (For visual purposes, we adjusted the brightness of the figure.) (Reprinted from “Integral imaging using phase-only LCoS spatial light modulators as Fresnel lenslet arrays,” Ali Özgür Yöntem and L. Onural, J. Opt. Soc. Am. A vol. 28, no. 11, pp.2359-2375, 2011. ©2011 OSA.) 41

- 3.1 Capture setup (Revised from “Integral imaging using phase-only LCoS spatial light modulators as Fresnel lenslet arrays,” Ali Özgür Yöntem and L. Onural, *J. Opt. Soc. Am. A* vol. 28, no. 11, pp.2359-2375, 2011. ©2011 OSA.) 44
- 3.2 Display setup (Reprinted from “Integral imaging using phase-only LCoS spatial light modulators as Fresnel lenslet arrays,” Ali Özgür Yöntem and L. Onural, *J. Opt. Soc. Am. A* vol. 28, no. 11, pp.2359-2375, 2011. ©2011 OSA.) 50
- 3.3 Experimental setup (Reprinted from “Integral imaging using phase-only LCoS spatial light modulators as Fresnel lenslet arrays,” Ali Özgür Yöntem and L. Onural, *J. Opt. Soc. Am. A* vol. 28, no. 11, pp.2359-2375, 2011. ©2011 OSA.) 53
- 3.4 Top view of the optical setup: upper rectangle shows the capture part and lower square shows the display part. In between, a small rectangle shows the diffuser, which acts as a capture and display device, on the elemental images plane. The object is behind the white cardboard on the right before the projector lens. The cardboard prevents the light from the LED array to spread everywhere. The vertical dashed line after the projector lens shows the object plane. Dashed lines with the arrows shows the optical path. The small diffuser after the mirror is used to show that the image at the calculated reconstruction distance is real. (Reprinted from “Integral imaging using phase-only LCoS spatial light modulators as Fresnel lenslet arrays,” Ali Özgür Yöntem and L. Onural, *J. Opt. Soc. Am. A* vol. 28, no. 11, pp.2359-2375, 2011. ©2011 OSA.) 54
- 3.5 LED array that we used as the object. We put a black mask over the inner LEDs to form a (mirror image) “C” shaped object. (Reprinted from “Integral imaging using phase-only LCoS spatial light modulators as Fresnel lenslet arrays,” Ali Özgür Yöntem and L. Onural, *J. Opt. Soc. Am. A* vol. 28, no. 11, pp.2359-2375, 2011. ©2011 OSA.) 55

- 3.6 An image of the LED array on the object plane: the object is first imaged onto this plane by a projector lens to control both the depth and the size of the object. (Reprinted from “Integral imaging using phase-only LCoS spatial light modulators as Fresnel lenslet arrays,” Ali Özgür Yöntem and L. Onural, *J. Opt. Soc. Am. A* vol. 28, no. 11, pp.2359-2375, 2011. ©2011 OSA.) 56
- 3.7 Optically captured elemental images (“Integral imaging using phase-only LCoS spatial light modulators as Fresnel lenslet arrays,” Ali Özgür Yöntem and L. Onural, *J. Opt. Soc. Am. A* vol. 28, no. 11, pp.2359-2375, 2011. ©2011 OSA. Reprinted with permission.) 56
- 3.8 Optical reconstruction (Reprinted from “Integral imaging using phase-only LCoS spatial light modulators as Fresnel lenslet arrays,” Ali Özgür Yöntem and L. Onural, *J. Opt. Soc. Am. A* vol. 28, no. 11, pp.2359-2375, 2011. ©2011 OSA.) 57
- 4.1 (a) A generic sketch of holographic recording. The diffraction pattern at $z = z_0$ is captured. (b) A generic sketch of 3D image reconstruction from the captured hologram. (Reprinted from “Integral imaging based 3D display of holographic data,” Ali Özgür Yöntem and L. Onural, *Opt. Express* vol. 20, no. 22, pp.24175-24195, 2012. ©2012 OSA.) 60

4.2 (a) A generic integral imaging data capture setup. The diffraction pattern in Fig.4.1 (a) is also depicted. For the same object with the same physical dimensions, the diffraction patterns in both systems are the same. (b) A generic Integral imaging display setup. The reconstruction is pseudoscopic due to employed direct pick-up method.(c) Designed model to calculate elemental images from diffraction (hologram) data. (Reprinted from “Integral imaging based 3D display of holographic data,” Ali Özgür Yöntem and L. Onural, Opt. Express vol. 20, no. 22, pp.24175-24195, 2012. ©2012 OSA.) 61

4.3 The algorithm to generate elemental images from a diffraction pattern. (Reprinted from “Integral imaging based 3D display of holographic data,” Ali Özgür Yöntem and L. Onural, Opt. Express vol. 20, no. 22, pp.24175-24195, 2012. ©2012 OSA.) 65

4.4 Computed and recorded elemental images of two letters at different depths and positions. (We enhanced the brightness of the figure for visual purposes. This is achieved by stretching the contrast. The figure is also used on the LCD display of the integral imaging setup as is. Similar enhancement procedure is used in Figs. 4.6, 4.8 and 4.17-4.20. In Figs. 4.17-4.20, we enhanced only the computer simulation results.) (Reprinted from “Integral imaging based 3D display of holographic data,” Ali Özgür Yöntem and L. Onural, Opt. Express vol. 20, no. 22, pp.24175-24195, 2012. ©2012 OSA.) 68

4.5 A sketch of the pyramid object. A square pyramid is sampled (sliced) over the z -axis. Base part is a square frame while the edges and the tip of the pyramid are small square patches. For display purposes we showed six slices of the object whereas in the simulations we used nine slices. (Reprinted from “Integral imaging based 3D display of holographic data,” Ali Özgür Yöntem and L. Onural, Opt. Express vol. 20, no. 22, pp.24175-24195, 2012. ©2012 OSA.) 69

- 4.6 Computed and recorded elemental images of the pyramid object. (We enhanced the brightness of the figure for visual purposes.) (Reprinted from “Integral imaging based 3D display of holographic data,” Ali Özgür Yöntem and L. Onural, *Opt. Express* vol. 20, no. 22, pp.24175-24195, 2012. ©2012 OSA.) 70
- 4.7 (a) The amplitude picture of the diffraction pattern of the epithelium cell. (b) The upsampled (interpolated and low pass filtered) version of (a). (The hologram data, from which this reconstruction was obtained, was courtesy of cole Polytechnique Fdrale de Lausanne within the Real 3D project.) (Reprinted from “Integral imaging based 3D display of holographic data,” Ali Özgür Yöntem and L. Onural, *Opt. Express* vol. 20, no. 22, pp.24175-24195, 2012. ©2012 OSA.) 73
- 4.8 Computed and recorded elemental images of the epithelium cell. (We enhanced the brightness of the figure for visual purposes.) (The hologram data, from which this reconstruction was obtained, was courtesy of cole Polytechnique Fdrale de Lausanne within the Real 3D project.) (Reprinted from “Integral imaging based 3D display of holographic data,” Ali Özgür Yöntem and L. Onural, *Opt. Express* vol. 20, no. 22, pp.24175-24195, 2012. ©2012 OSA.) 74
- 4.9 Toy object (The hologram data, from which this reconstruction was obtained, was courtesy of National University of Ireland, Maynooth within the Real 3D project.) 75
- 4.10 Reconstructed hologram of the toy object. (The hologram data, from which this reconstruction was obtained, was courtesy of National University of Ireland, Maynooth within the Real 3D project.) 76
- 4.11 Elemental images of the toy object. (The hologram data, from which this reconstruction was obtained, was courtesy of National University of Ireland, Maynooth within the Real 3D project.) . . . 76

- 4.12 The optical setup (Reprinted from “Integral imaging based 3D display of holographic data,” Ali Özgür Yöntem and L. Onural, Opt. Express vol. 20, no. 22, pp.24175-24195, 2012. ©2012 OSA.) 78
- 4.13 A Fresnel lenslet array pattern with 12×20 lenslets. Each lenslet has a focal length of $10.8mm$. We excluded the lenslet on either side of the array since they would be cropped if we have included them. Instead we left 60 pixels blank from either side of the array that is written on the 1920×1080 pixels phase only LCoS SLM. (Reprinted from “Integral imaging based 3D display of holographic data,” Ali Özgür Yöntem and L. Onural, Opt. Express vol. 20, no. 22, pp.24175-24195, 2012. ©2012 OSA.) 79
- 4.14 Picture of the entire optical setup. (Reprinted from “Integral imaging based 3D display of holographic data,” Ali Özgür Yöntem and L. Onural, Opt. Express vol. 20, no. 22, pp.24175-24195, 2012. ©2012 OSA.) 80
- 4.15 Top view of the optical setup. There is a wireframe pyramid object next to the reconstruction zone. It is used to compare the reconstructed 3D images of the pyramid object. (Reprinted from “Integral imaging based 3D display of holographic data,” Ali Özgür Yöntem and L. Onural, Opt. Express vol. 20, no. 22, pp.24175-24195, 2012. ©2012 OSA.) 81
- 4.16 The viewing zone of the optical setup. We placed cards labeled as “Bilkent University” at different distances in order to check the reconstruction distances. (Reprinted from “Integral imaging based 3D display of holographic data,” Ali Özgür Yöntem and L. Onural, Opt. Express vol. 20, no. 22, pp.24175-24195, 2012. ©2012 OSA.) 82

- 4.17 3D reconstruction from the elemental images of Fig. 4.4. At the top, digital reconstructions are shown while at the bottom we observe the optical counterparts. On the left side, the camera, which took this picture, was focused to a distance $8.4f$ and on the right side, it was at $13f$. (We enhanced the brightness of the computer simulation results for visual purposes.) (Reprinted from “Integral imaging based 3D display of holographic data,” Ali Özgür Yöntem and L. Onural, *Opt. Express* vol. 20, no. 22, pp.24175-24195, 2012. ©2012 OSA.) 83
- 4.18 3D reconstruction from the elemental images of Fig. 4.6. Images at the left are digital reconstructions. Images at the right are optical reconstructions. The top images are focused to the tip of the pyramid object and the images at the bottom are focused to the base of the object. It is clearly seen that the physical (wire) object and the reconstructed 3D images match. (We enhanced the brightness of the computer simulation results for visual purposes.) (Reprinted from “Integral imaging based 3D display of holographic data,” Ali Özgür Yöntem and L. Onural, *Opt. Express* vol. 20, no. 22, pp.24175-24195, 2012. ©2012 OSA.) 85
- 4.19 The pictures of the pyramid image taken from three different angles. (All are focused to the tip of the pyramid.) The pictures at the top are the digital reconstructions and the bottom ones are the optical reconstructions. The pictures show the parallax and the viewing angle. (We enhanced the brightness of the computer simulation results for visual purposes.) (Reprinted from “Integral imaging based 3D display of holographic data,” Ali Özgür Yöntem and L. Onural, *Opt. Express* vol. 20, no. 22, pp.24175-24195, 2012. ©2012 OSA.) 86

- 4.20 Reconstruction from the elemental images of Fig. 4.8. Top picture is the digital reconstruction whereas the bottom one shows the optical reconstruction. Since the object thickness is small relative to the reconstruction distance, a 3D depth is not perceived. However, the planar looking thin object still floats in 3D space. (We enhanced the brightness of the computer simulation results for visual purposes.) (The hologram data, from which this reconstruction was obtained, was courtesy of cole Polytechnique Fdrale de Lausanne within the Real 3D project.) (Reprinted from “Integral imaging based 3D display of holographic data,” Ali Özgür Yöntem and L. Onural, *Opt. Express* vol. 20, no. 22, pp.24175-24195, 2012. ©2012 OSA.) 87
- 4.21 Numerical reconstructions of the elemental images of the toy object. (The hologram data, from which this reconstruction was obtained, was courtesy of National University of Ireland, Maynooth within the Real 3D project.) 88
- 4.22 Optical reconstructions of the elemental images of the toy object. (The hologram data, from which this reconstruction was obtained, was courtesy of National University of Ireland, Maynooth within the Real 3D project.) 88
- 4.23 Digital reconstruction of the hologram of STAR WARS action figure: Storm Trooper. (The hologram data, from which this reconstruction was obtained, was courtesy of National University of Ireland, Maynooth within the Real 3D project.) 89
- 4.24 Elemental images obtained from the holographic data of the “Storm Trooper” action figure. (The hologram data, from which this reconstruction was obtained, was courtesy of National University of Ireland, Maynooth within the Real 3D project.) 90

4.25	Numerical reconstruction of the elemental images in Fig. 4.24. (The hologram data, from which this reconstruction was obtained, was courtesy of National University of Ireland, Maynooth within the Real 3D project.)	90
4.26	Optical reconstruction of the elemental images in Fig. 4.24. (The hologram data, from which this reconstruction was obtained, was courtesy of National University of Ireland, Maynooth within the Real 3D project.)	91
5.1	Orthoscopic reconstruction process	93
5.2	Orthoscopic elemental image generation process model	94
5.3	Pseudoscopic elemental images	95
5.4	Orthoscopic elemental images	96
5.5	In the first row, numerical reconstructions of the images of the letters using the elemental images in Fig. 5.3 are shown and in the second row, reconstructions of the elemental images in Fig. 5.4 are depicted. The first column is the focused images at $7f$ whereas the second column is the focused images at $10f$	96
5.6	Optical reconstructions of the elemental images in Fig. 5.3 and Fig. 5.4 are shown. The results are placed in the same way as in Fig. 5.5.	97

Dedicated to My Beloved Father in Heaven . . .

Chapter 1

INTRODUCTION

We live in a world of three dimensions if we exclude time and other hyper-dimensions. Historically, the perceived 3D scenes were painted or drawn on 2D surfaces. Only a very few people (artists) have the ability to reflect the scenes with perfect perspective and life-like images to visually please the onlookers. And only some brilliant ones, like Leonardo da Vinci and Giovanni Battista della Porta, realized the 3D perception can be reflected on the canvas [1]. However, the sculptors had the ability to replicate the scenes in 3D. After the invention of photography, it became possible for most of the people to capture scenes. Now, with the breakthroughs in the imaging systems, it is available for anyone to freeze the scene on 2D media. Moreover, we are able to record a series of these pictures to make movies. However, taking pictures and videos in two dimensions do not always satisfy us by the perceived reality as the original scene. We always want to perceive the image of the real scene with all of its details. Furthermore, animating the scene as if it is touchable will add more “reality” to the image. By replicating the original light distribution of the three dimensional scene, we would experience the excitement as if we were really there. Moreover, we can interact with this artificial yet the real replica. This is like sculpting the light. So, three dimensional imaging has always been an attractive field of study among display systems. There are various types of displays suggested to succeed this such as holography and stereoscopy [2].

Holography is an old technique to capture and display three dimensional scenes [3]. In this technique, the interference of a coherent reference light source and light scattered from the surface of an object under coherent illumination is recorded [4,5]. By this way, not only the amplitude but also the phase information, which inherently has the direction information, of the light is obtained. Even if the intensity of the complex field is recorded, the 3D information is still maintained. This is in fact like the modulation of a signal with a carrier signal [5]. This method exactly replicates the light distribution from the original scene. It aims to duplicate the light distribution scattered from the object, at the display end, as if the light is coming from the scene itself when the recorded data is illuminated by the same reference wave, creating a “true” 3D. Unfortunately, holography has many limitations and drawbacks. First of all, the method requires coherent illumination, that is, the light source should be based on lasers. This creates two practical problems: due to coherence, a diffusive surface illumination creates a random noise which is called the speckle. The direct optical reconstruction from the holographic data by holographic means has this problem. Thus, certain image processing techniques (filtering and averaging) are usually performed to remove the noise and to reconstruct the data digitally [6–8]. This way, the visibility in digital reconstructions can be improved. The other problem is the potential hazard that lasers might cause to human eye. So, it is not desirable to use lasers for the reconstruction, either. It may be possible to use LED illumination to avoid laser hazards while observing the optical holographic reconstructions [9,10]. However, the reconstruction quality would be lower due to spectral properties of the light source.

Another problem in holography is its high sensitivity to changes in phase. So, it is hard to manufacture a holographic recording camera for general purpose of use in our daily life. Thus, practical use of holographic displays in daily-life is not yet feasible. Digitally synthesized holograms are commonly used to display artificial three dimensional objects. Also, digitally recorded optical holograms can be displayed on holographic setups. However, these are limited to lab environments at present.

Stereoscopy, which is another three dimensional capture and display method,

is now a widely used method in theaters, home cinemas and computers; it is much older than holography. Stereoscopy is first devised by Charles Wheatstone in 1832 although Euclid defined the idea as “To see in relief is to receive by means of each eye the simultaneous impression of two dissimilar images of the same object” [1]. Stereoscopic techniques mimic the human visual system creating the illusion of 3D image perception while we are looking at a 2D surface. In these systems, two pair of images are displayed on a 2D media and the images are received by the observers’ eyes. To deliver the stereo pair of the images to the observers eyes’, one must wear a pair of special glasses. There are certain system configurations which use passive and active glasses. The type of the glasses used depend on the system choice. However, all of them irritate or are cumbersome for the users.

The stereo image pairs are captured from slightly different angles of a 3D object/scene. The resulting disparity correspond to the slightly different locations of the eyes. The perceived images are then interpreted by the brain as if the observer is looking at the original object. Certain problems arise while perceiving the tree dimensional reconstruction. One associated problem is the difficulty to adapt to the resultant three dimensional reconstruction. The adaptation problem is referred as the accommodation-convergence mismatch [11, 12]. It creates eye strain and fatigue in extended time of use. The other problem is the discomfort as a result of the limited parallax that the system delivers. The system can deliver a stereo pair of pictures that are horizontally aligned. Thus the system provides only horizontal parallax. However, this is limited to only a certain angle. Thus, the observer will only perceive in 3D from the same angle while moving horizontally around the display. This is a very unnatural discomfort inherited by the stereoscopic techniques [13].

To overcome the discomfort introduced by using the glasses, auto-stereoscopic displays are introduced [11]. The users do not need to wear such glasses. The idea is to put an optical structure on the display panel. There are mainly two methods to obtain auto-stereoscopic displays: a lenticular cylindrical lens array or a parallax barrier. In both methods, the idea is to display an interzigged image on the display panel and separate the left and the right images using the optical structures. In the lenticular version, the cylindrical lenses image the pixels

behind them to the corresponding eye as left and right images. In the barrier version, a fence structure with opaque and transparent stripes blocks or permits the pixels behind them to be seen as left and right images by the observer. The optical designs of the systems change according to the used method. However, the observer is required to be in a certain location (“sweet spot”) in front of the display to enjoy the 3D visualization [13]. These systems are still stereoscopic systems and inherit the same problem as the systems with glasses.

Another technique, which improves the horizontal parallax of stereoscopy, is the multi-view auto-stereoscopy. In stereoscopy we have two views and this limits the perceived parallax. In multi-view systems, we have more than two views, that is, there are more than two cameras, which are separated by a slightly different angle, facing the 3D object. So, each camera provides different perspectives of the same 3D object/scene. There exists eye-tracking systems and head-tracking systems [1, 12, 13]. So, depending on the position of the observer, the corresponding view of the 3D object/scene is imaged to the observer’s eyes.

Another method, which is now quite popular, used for multi-view auto-stereoscopic systems is integral imaging which is first proposed by Gabriel Lippmann [14]. These systems use a lens array to capture the three-dimensional scene on a two-dimensional capturing device. Each lens images a two-dimensional picture, which is called elemental image, of the three-dimensional scene. Since each lens images from a certain direction, the three-dimensional information is inherently obtained. When the captured elemental images are observed through the same lens array with proper imaging distances, one can observe the three-dimensional image reconstruction of the original object. Since an array of small spherical lenses are used instead of lenticular lenses, this method provides parallax also in the vertical direction.

Despite the popularity and availability of 3D displays with glasses, there is a strong urge to do more research on glasses-free 3D displays. Consumers demand to view 3D images without using any worn devices since it is the natural way to perceive in 3D. Among several approaches, we chose to work on integral imaging systems. This dissertation presents two novel integral imaging systems.

Long after Lippmann had proposed the integral imaging, it became a popular research topic [15] and now it is used as a 3D auto-stereoscopic capture and display method. As CCD arrays and LCDs emerged, digital implementations of Lippmann's original work are also reported [16]. Chemical photographic capture and display processes are now almost entirely replaced by these digital recording and display devices. Today, the resolution and size of these digital devices are sufficiently high for experimental capture and display of small sized 3D objects/scenes. Even if the resolution of these devices is not yet comparable to that of chemical photographic emulsions, the perceived 3D object quality is quite good. Such devices are getting more and more popular due to well known advantages such as flexibility and also due to the easy reproducibility, processing, storage and transmission of the data written on these devices.

In [17, 18], the optimum design parameters are studied extensively for the integral imaging method. The limitations of the method on the transversal and depth resolution are analyzed in those papers. The current research focus in integral imaging is mainly on quality improvements of perceived 3D objects/scenes by changing the physical properties of the lenslet arrays [19, 20].

There are certain problems associated with the nature of the integral imaging system. The system actually samples the scene by each lens in the array. While reconstructing, this causes a kind of aliasing, that is, we see more than one reconstruction at different angles. This also brings us the coupled problem, viewing angle. Since the system uses lenses with fixed physical parameters, the zone, which we can observe the three-dimensional reconstruction, is limited. A structure composed of a curved screen and a curved lenslet array is proposed [21] to overcome this problem. Since it is difficult to produce such lenses, placing a large aperture lens, which simulates a curved array, in front of a planar array of lenses was also proposed [22]. There are also solutions that improves the viewing angle by implementing lens switching by use of active devices like LCD panels [23]. This problem is also overcome by an all-optical solution with the use of telecentric relay system [24].

Limited depth of field is another issue. Lenses with fixed physical parameters

also result in limited depth of field. The lenses can image a certain depth of the scene in focus while other depths are out of focus. This is obviously natural and it limits the 3D volume that the system can capture. There are certain solutions to this problem in the literature. It is shown that by using amplitude masks the depth of focus of the system can be increased by trading-off lateral resolution and light throughput [19,25]. It is also possible to use phase masks on the lenslets to improve the depth range of the system [20]. There are also other approaches to overcome this issue. In one study, it is shown that the source of limited depth also comes from the pixelated structure of the CCD sensor and it is more restrictive compared to the diffraction limitations of the lenslets [26]. Another study proposes a non-uniform focal length and aperture sizes for the lenslets in a time-multiplexed scheme to improve the depth of focus [27]. It is also reported that the real and virtual image fields can be used to improve the depth of focus [28].

Another problem of integral imaging is pseudoscopic 3D object perceived at the display end. The simplest practical solution is to replicate the process once more to obtain an orthoscopic image [15]. However, this makes the system or the process cumbersome. There are digital methods which implements this idea by remapping the pixels of elemental images of a 3D object [29–31]. There is another method to solve this problem that can be implemented either digitally [16] or optically [32]. In this method, the elemental images are rotated around their own axes.

Even if those issues are fundamentally important to improve the perceived image quality, the generic system did not change much. The key element of the system, lenslet array, is still mostly an analog device. Usually, it is a fixed component with fixed physical parameters. Most of the solutions are related to designing the physical properties of the lenses. However, each design changes the entire setup. Moreover, manufacturing a new lens array for each setup is a cumbersome and expensive process. It is desirable to have a digitally controlled optical device, which will behave as a lens array, instead of a hard lens array. This way it is more practical to change the physical properties of the system. It is difficult to manufacture such special lenslet arrays. It would be much easier to

program an electronic device which would act as an electronic lenslet array.

Fortunately, it is shown that programmable lenslet arrays can easily be implemented using LCoS phase-only spatial light modulators (SLMs) for adaptive optics, as used in Hartmann-Shack sensors [33, 34]. SLMs are tiny displays with high pixel count with small pixel size. Such devices can work in phase-only mode so that Fresnel lenses can be written on them [35–37]. In some early studies, magneto-optic SLMs are used to write binary Fresnel lens patterns [38]. Moreover, it is shown that, it is possible to generate such lenslet arrays [39]. It is also mentioned in [39] that a generated lenslet array is used to image a 3D object. However, experimental results were not given. In [40], it is presented that electronically synthesized Fresnel lenslet arrays can be encoded on an LCD panel for integral imaging. In that paper, they showed the potential of the idea by applying it to their previous setup which increases the viewing angle by mechanically moving the lenslet array. In theory, the electronic lenslet array replaces the moving lenslet array. However, because of the physical limitations of the LCD panel, it is reported that such lenslet arrays were not used in the optical experiments of the pick-up process. It is also reported that perceived resolution of the 3D reconstruction with bare eye with the above-mentioned system was very low. They suggested that smaller pixel size would give better results.

We improved the idea by using LCoS phase-only SLMs instead of a LCD panel or other type of SLMs. The diffraction efficiency is higher than that of a LCD panel. Furthermore, since the SLM is phase-only, it will behave as a real lens when a Fresnel lens pattern is written on it. Of, course, we cannot write a continuous function, in this case the Fresnel lens pattern, on a SLM. Thus, we first sample and then quantize the resulting function and program the SLM with these pixel values through its driving circuitry. We analyze the effects of using pixelated and quantized lenslet arrays in an integral imaging system and found physical parameters which affect the design of integral imaging systems using digital lenses. Specifically, we find the analytical results for the output elemental images of the capture stage with a self luminous 3D point cloud input. We carried the analysis as if the source points are coherent sources. The pixelated and quantized lenslet arrays introduce some artefacts. Two of these are multiple focal lengths due to

quantization and, higher-order diffractions due to the pixelated structure of the lenslets. There is also inherent apodization due to the finite pixel size [41]. We carry out the analysis by taking into consideration these features of pixelated and quantized lenslet arrays and, show that when these effects are ignored, the results simplify to the previous results given in the literature [19,25]. We run simulations to confirm the theoretical results and they are in good agreement. Furthermore, we show that we can construct a versatile integral imaging system by using a programmable lenslet array which is formed by writing an array of Fresnel lenslet phase profiles on a high definition (1920×1080) reflective phase-only LCoS SLM (Holoeye HEO 1080P); this replaces the conventional lenslet array. Furthermore, we present theoretical background for the system. In our system we use a similar scheme as in, [42], since our SLM device is also reflective type. In that system, a concave mirror array replaces the lenslet array and the image is formed by the help of a half mirror. The elemental images on a 2D display are integrated at the reconstruction distance that is not on the same optical axis with the elemental images. The half mirror folds the optical axis by 90 degrees. The reconstructed 3D object is formed away from the half mirror. Both of the capture and display parts of our system work with half mirrors. The elemental images and the reconstructed images of the capture and the display systems are formed away from the half mirrors. However, we use a 2D lenslet array phase profile which is written on the SLM electronically instead of a concave mirror array. This way we succeeded to implement the entire integral imaging structure as a digital system. We believe that this approach increases the capability and flexibility of the system, significantly. Thus all subsequent improvements to increase the system quality can be implemented easily by electronically changing the lenslet array structure using digital means. For example, to increase the depth of field of the system, it is possible to generate lenslets with phase apodizations and implement the digital counterpart of the analog solution given in [20] using phase-only SLMs. Also, it is much easier to generate lenslets with different physical properties and use them in the same lenslet array. Analog version of such a scheme is discussed in [27]. It is also shown that irregularly placed lenslets increase the spatial and lateral resolution [43]. Again, it is more practical to implement irregularly arranged lenslet arrays digitally using SLMs.

We also implemented the idea of using digital lenslet arrays for a display-only setup. Integral imaging is a promising 3D capture and display system for the next generation 3D displays. As it is mentioned above, the conventional integral imaging systems are composed of two stages: a pick-up system to obtain elemental images of a 3D object/scene and a display stage which integrates the elemental images for reconstruction [14]. These parts are physical optical setups. These setups are usually not end-to-end, that is, two setups are separate. In the capture part, the elemental images are imaged by means of a series of lenses and a lenslet array, on a CCD array or a digital camera. In the display setup, the obtained elemental images are displayed on a LCD and the reconstruction is observed through a lenslet array. It is necessary to match the size of the captured elemental images on the CCD to the displayed ones on the LCD in the display setup since the physical sizes of the devices are usually different. Furthermore, the pixel size and number of the CCD sensor matter since the quality of the reconstruction depends on these parameters. Finally, the LCD panel in the display setup should be able to accommodate all of the captured elemental images. To display a good quality still 3D image or a video sequence, both setups require usual adjustments and alignments (imaging distances, magnification ratios, etc.) of optical elements. Such a work is studied rigorously in [16]. That work is an example for the case where optically captured elemental images of a physical 3D object are reconstructed optically at the display end. Such integral imaging systems consist of decoupled capture and display units, and therefore, both units need careful adjustments. For applications such as 3D gaming, 3D modeling, animation, etc., the only physically needed part is the display. In those systems, the elemental images are digitally obtained for synthetic 3D objects and then displayed on an optical display setup. Digital techniques are more flexible compared to optical capture processes. If the elemental images are obtained by computation, optical adjustments are needed only for the display part. Ray tracing methods can be used to generate elemental images. There are many reported methods using ray tracing techniques to obtain elemental images for computer generated integral imaging systems [44–48]. The capture process, for computer generated integral imaging systems, is performed using certain computer graphics algorithms such

as point retracing rendering, multiple viewpoint rendering, parallel group rendering, viewpoint vector rendering, etc., [49]. All of these algorithms are based on ray tracing.

In our work, as an alternative method to generate elemental images, we performed diffraction calculations using wave propagation methods based on the Fresnel kernel. To the best of our knowledge, such an approach is not reported before. One can compute the scalar field distribution in the space using the Fresnel propagation model [50, 51]. We can generate elemental images by first modeling the optical system with image processing tools and then by applying optical wave propagation principles [52]. This method enables us to implement the “correct” simulation of optical integral imaging capture systems, since, the wave propagation models accommodate diffraction and interference phenomena whereas ray models do not [5, 53]. Wave propagation models are especially useful for the cases where we have holographic data of a 3D object/scene. This is in fact an inverse problem of hologram generation from elemental images [46, 54, 55]; that is, we obtain elemental images from a holographic recording as in [56].

As mentioned above there are problems in the optical reconstruction of thin holograms since lasers are used to illuminate the setups. On the other hand, integral imaging works primarily with incoherent illumination. It may be desirable to reconstruct holographic data by an integral imaging display. A conversion from holographic data to elemental image data is needed to reconstruct the 3D image using incoherent light and integral imaging techniques. Such an idea is studied in [56]. In that work, first a series of images are reconstructed at different depths, creating a set of slices of 3D data. Then, the elemental images are generated using another process which maps each slice to the elemental image plane. Instead of such an approach, we directly use holographic data to display 3D images on an integral imaging setup. For this purpose, we designed a direct pick-up integral imaging capture system, [47]. This digital pick-up system is realized solely by a computer program that simulates wave propagation. Lenslet arrays that we used in the design are composed of digital synthetic Fresnel thin lenslets [52]. We processed the input holographic data with this simulator to obtain computer generated elemental images. This way, we generate the elemental images in one step.

We used these computer generated elemental images in a physical display setup to reconstruct optically 3D images. In our proposed display, we used a modified version of the setup given in [52] where we replaced the analog lenslet array with a digitally controlled synthetic Fresnel lenslet array written on a phase-only LCoS SLM. By this procedure, we can generate elemental images digitally from recorded holographic input data and optically reconstruct a 3D image from them on our integral imaging display. For example, our method can be used to generate elemental images from holograms captured within a diffraction tomography setup [57].

In some cases, diffraction calculation might be slower than ray tracing calculations. There are several fast algorithms which implement diffraction calculations based on the Fresnel kernel [58]. Even real-time diffraction calculations are possible [59]. Indeed, one of the implementations uses the Graphical Processing Unit (GPU) to further increase the computation speed [60]. Our elemental image generation method is quite similar to techniques used in digital hologram generation procedures. We calculated the diffraction fields using DFT. We computed the DFT using an FFT algorithm. It is possible to apply other abovementioned faster algorithms to our case, as well. However, the comparison of the effects of such different computational procedures to the performance is not a part of this study.

Presented numerical and optical results show that the computationally generated elemental images using wave propagation principles from synthetic or physical objects can be used to successfully reconstruct 3D images. Furthermore, a digitally controlled synthetic lenslet array can be used at the display stage setup of an integral imaging system [40, 52].

Finally, we presented a practical solution to pseudoscopic reconstruction problem. After generating the elemental images numerically, we further processed the elemental images. The input of this new process is the elemental images that give pseudoscopic reconstruction at the display end, and the output is the elemental images that give orthoscopic reconstruction. The conversion process achieved by using wave propagation tools for the simulation of the two-step optical conversion

system [15, 32, 61].

In Chapter 2, we give theoretical background for wave propagation and discretization of Fresnel lenses. We present the formulation for lenslet array patterns with certain focal lengths and describe the properties of such discrete lenslets. We review the multiple focal points issue due to quantization and multiple diffraction orders due to discretization. We have demonstrated the results of computer simulations and give correspondences to the theoretical results of an integral imaging system with digital lens arrays. In Chapter 3, we present the theoretical analysis of the capture part, of an integral imaging system with a digital lens array from a signal processing perspective and give a brief explanation for the display system. We also demonstrate the proposed systems for both capture and display parts of the integral imaging setup for specific physical parameters and describe the optical setup and present the optical experiment results. In Chapter 4, we explain the method to obtain elemental images from a holographic recording. Then, we present a display-only integral imaging based system which uses the described method. We also show the comparison of numerical and optical results. In Chapter 5, we demonstrate the pseudoscopic to orthoscopic conversion process together with the optical and numerical results. In the last chapter, we draw our conclusions.

Chapter 2

PRELIMINARIES: SAMPLING OF DIFFRACTION FIELD AND DIGITAL FRESNEL LENS ARRAYS

Before proceeding into the analysis of an integral imaging system with digital lenslet array, let us look at the basic tools that we used in the derivations in the following chapters. This chapter is dedicated to the discretization of the functions representing the propagation of light in free space and the functions representing the phase of a single lens and an array of such lenses. We will show the consequences of using the discrete versions in the equations. We will also discuss physical implications of the discretization of these equations. We will conclude this chapter with the numerical examples.

We mainly analyze the lens imaging. For this purpose, we need to choose a tool to explain the “true” optical behavior of the system. The simplest tool is the ray optics [5]. It explains the propagation of the light by defining rays from a source point through optical components to the imaging point. However, it ignores the diffraction phenomenon since the wavelength is considered to be

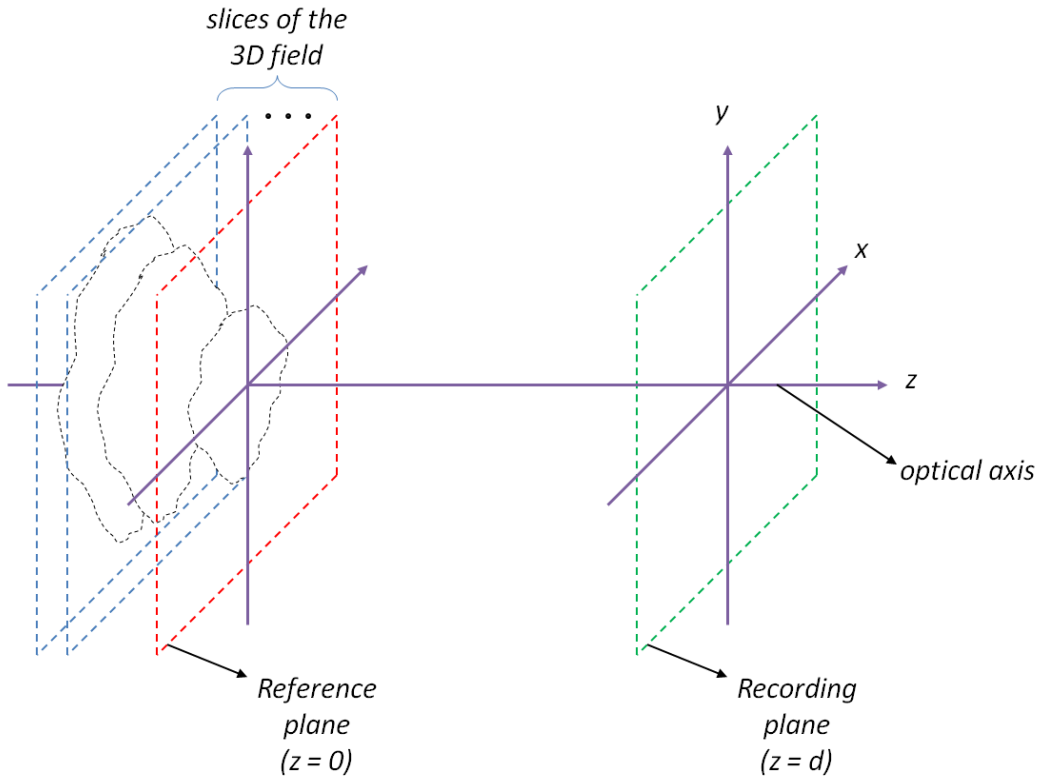


Figure 2.1: Calculation of the diffraction field of a sliced 3D field.

very small compared to the optical components [3, 5]. Although it is useful, this tool will not suffice our needs. We want to study the cases where we used diffractive optical components. We chose the wave optics tools as the best option considering our needs for the analysis [3, 5, 53]. There are also, electromagnetic and quantum optics tools. However, these tools are too complicated for the needs of our analysis. These tools provide the explanation of the effects of polarization of light and nature of light based on photons but we will deal only by employing scalar fields.

In wave optics, we have certain tools to explain the propagation of light in the free space. Based on these, it is possible to obtain input-output relations for a certain optical setup. Moreover, we can easily apply signal processing basics to obtain such relations. This is in fact known as Fourier optics [5, 53]. Furthermore, we can easily compute the output for a certain input with signal processing algorithms [3].

In the general sense, we deal with 3D light fields. Calculation of the optical field at a certain distance is always a challenge [3]. First of all, we need to find a way to represent the 3D field. Then, based on this representation, we need to find a good tool to calculate the field. In physical life, the 3D field is continuous in space. One way to represent the field is to slice the field by planes. So, we swap the continuous field with a set of 2D discrete slices as shown in Fig. 2.1. The way we slice the field is also an issue. We choose the optical axis to be along the z -direction. We also need to choose a reference plane. The simplest approach would be to choose a slice of the 3D field that is perpendicular to the optical axis as the reference plane, $z = 0$. The reference plane is shown as red in Fig. 2.1. The other slices of the set will be parallel to the reference plane. And we take many slices enough to cover the entire 3D field [62]. Here, we are interested in the total optical disturbance that is created by the sliced 3D field on a plane at a certain distance $z = d$. The relation between the field patterns on each slice and the recording plane (shown as green in Fig. 2.1) is given by the convolution of the input field and the impulse response of a linear shift invariant system that represents wave propagation in free space [3, 53, 63]. The impulse response of the system that gives the exact result for scalar fields by taking both propagating and evanescent waves into account is the Rayleigh-Sommerfeld diffraction kernel [53]. However, since we are interested in the propagating components of light, the convolution kernel for these components is defined as,

$$h_z^{RS}(x, y) = \frac{1}{j\lambda} \frac{\exp\left(j\frac{2\pi}{\lambda}\sqrt{x^2 + y^2 + z^2}\right)}{\sqrt{x^2 + y^2 + z^2}} \cos\theta \quad (2.1)$$

where $x, y \in \mathbb{R}$ are the transversal spatial domain variables and λ is the wavelength, [3]. Eq. (2.1) gives optical disturbance on a plane at a distance z due to a 2D impulsive source on a slice.

It is generally more practical and easy to interpret the Fourier transform of Eq. (2.1) [64, 65]. The Fourier transform of Eq. (2.1) can be found as

$$H_z^{RS}(f_x, f_y) = \begin{cases} \exp\left[j2\pi\left(\frac{1}{\lambda^2} - f_x^2 - f_y^2\right)^{1/2}z\right], & \sqrt{f_x^2 + f_y^2} \leq 1/\lambda \\ 0, & \textit{else} \end{cases} \quad (2.2)$$

where $f_x, f_y \in \mathbb{R}$ are the spatial frequency domain variables in cycles per unit

distance. Eq. (2.2) is known as the transfer function of the linear shift invariant system that represents free space propagation. We take $H_z^{RS}(f_x, f_y) = 0$ for $\sqrt{f_x^2 + f_y^2} > 1/\lambda$ since we keep all evanescent waves out of the analysis [5]. Eq. (2.2), is also known as the plane wave decomposition [3, 63]. Plane wave decomposition method is also used to obtain the diffraction field between two parallel planes. To find the, the input-output relation using the plane wave decomposition we compute

$$\psi_z(x, y) = \mathcal{F}^{-1} \{ \mathcal{F} \{ \psi_0(x, y) \} H_z^{RS}(f_x, f_y) \}$$

in [63], where $\psi_0(x, y)$ is the input field on the reference plane and $\psi_z(x, y)$ is the output field on another plane at a distance z . $\mathcal{F} \{ \psi(x, y) \} = \int_{-\infty}^{\infty} \psi(x, y) \exp[-j2\pi(xf_x + yf_y)] dx dy$ is the 2D Fourier transform and $\mathcal{F}^{-1}\{.\}$ is the inverse operator. In the spatial frequency domain, each frequency component of the input field, $\mathcal{F} \{ \psi_0(x, y) \}$, determines the coefficient of the propagating plane waves.

Even if Eq. (2.2) seems simple, we need to deal with a simpler version of this. This is because the function given by Eq. (2.2) is not separable (the square root inside the brackets do not allow separability), so, it complicates the analytic expressions. Moreover, when we try to find numerical results, this equation will increase the computation time, significantly. So, we need to approximate this equation.

Assume that we have propagating waves with frequencies much lower than the cut-off frequency $f_x^2 + f_y^2 \leq \frac{1}{\lambda^2}$ of the free space. These waves obey the paraxial approximation. If we apply Taylor series expansion and neglect the higher order terms in the expansion, we will eventually get the Fourier transform of continuous Fresnel kernel

$$H_z^{Fr}(\mathbf{f}) = \exp\left(j\frac{2\pi}{\lambda}z\right) \exp(-j\pi\lambda z \mathbf{f}^T \mathbf{f}) \quad (2.3)$$

where $\mathbf{f} = [f_x \ f_y]^T$ [51]. This is known as the Fresnel kernel [5]. We can safely use Fresnel diffraction, based on this kernel, for most of the optical cases. It is an approximation with the constraint that propagating waves do not spread too much around the optical axis as the light travels in space. Taking the inverse Fourier transform of Eq. (2.3), we can define the 2D impulse response of the

Fresnel diffraction from one plane to another plane as,

$$h_z^{2D}(\mathbf{x}) = \frac{1}{j\lambda z} \exp\left(j\frac{2\pi}{\lambda}z\right) \exp\left(j\frac{\pi}{\lambda z}\mathbf{x}^T\mathbf{x}\right) \quad (2.4)$$

where $\mathbf{x} = [x \ y]^T$, [51, 66]. For a definite distance that light travels in space between two parallel planes, the equivalent model for this equation, is a linear shift invariant system. So, we can use this equation to model the input-output relations and find the analytic expressions of our imaging system. The complex amplitude, $\frac{1}{j\lambda z} \exp\left(j\frac{2\pi}{\lambda}z\right)$, can be dropped from the computations whenever there are only two planes of interest (one input and one output plane). This is because z is a constant and therefore, this term is also constant. However, whenever there is a volume, the depth becomes a variable, and therefore, such simplifications require more care. For a rather thin volume the term $\frac{1}{j\lambda z}$ can still be approximated as a constant. However, the phase term $\exp\left(j\frac{2\pi}{\lambda}z\right)$ is sensitive to z and cannot be omitted for such cases. When the constants are dropped from Eq. (2.4), we are left with the 2D quadratic phase function which is given as

$$\begin{aligned} h_\alpha^{2D}(\mathbf{x}) &= \exp(j\alpha\mathbf{x}^T\mathbf{x}) \\ &= (j\lambda z) \exp\left(-j\frac{2\pi}{\lambda}z\right) h_z(\mathbf{x}) \Big|_{z=\frac{\pi}{\lambda\alpha}} \end{aligned} \quad (2.5)$$

We will use Eq. (2.5) to define Fresnel lenses and lens arrays. A lens phase function is defined as

$$l_{-\gamma}^{2D}(\mathbf{x}) \triangleq \exp(-j\gamma\mathbf{x}^T\mathbf{x}) = h_{-\gamma}^{2D}(\mathbf{x}) \quad (2.6)$$

where $\gamma = \frac{\pi}{\lambda f}$ and f is the focal length.

The purpose of the following sections is to form the theoretical background of a conventional integral imaging setup, where an analog lenslet array is replaced by an LCoS SLM which has an array of Fresnel lenslets written on it. Since the SLM has a discrete nature we need to determine the 2D discrete array that will be written on the SLM. The 2D discrete pattern of Fresnel lenslet array written on the SLM is calculated by first sampling a quadratic phase function with certain parameters to represent a single Fresnel lenslet, and then, by quantizing the sample values to match the phase levels that the SLM can support, and

finally, by replicating as many single lenslets in 2D as the SLM dimensions can support. Before the analysis of the capture setup, we review the response of a single sampled and quantized lenslet and also an array of such lenslets to a plane wave illumination. For the continuous field propagation analysis, we converted the 2D discrete pattern to a continuous field by interpolating it with the pixel function related to the SLM.

2.1 Discrete Quadratic Phase Array Patterns

It is crucial to determine how we generate the lenslet array. Under the Fresnel approximation, the phase pattern of a thin lens is a quadratic phase function as given in Eq. (2.5). For the simplest case let us consider a sampled (discrete) thin lens phase pattern written on an SLM device. If we sample Eq. (2.5), we will obtain a generic function to represent Fresnel lenslets that can be used to program an SLM device. Substituting \mathbf{x} by $\mathbf{V}\mathbf{n}$ in Eq. (2.5), we get the 2D complex discrete quadratic phase pattern

$$\tilde{h}_{D,\alpha}[\mathbf{n}] \triangleq \tilde{h}_{\alpha}^{2D}(\mathbf{x}) \Big|_{\mathbf{x}=\mathbf{V}\mathbf{n}} = \exp(j\alpha\mathbf{n}^T\mathbf{V}^T\mathbf{V}\mathbf{n}) \quad (2.7)$$

where \mathbf{V} is the 2D-sampling matrix. For simplicity we chose a regular rectangular sampling matrix $\mathbf{V} = \begin{bmatrix} X & 0 \\ 0 & X \end{bmatrix}$ where X is the sampling period (pixel period of the SLM) and $\mathbf{n} = [n_1 \ n_2]^T$ where n_1, n_2 are integer variables in $(-\infty, \infty)$ [51,52].

The sampling of the quadratic phase function will cause a very specific type of aliasing and naturally generates an array of Fresnel lens patterns [67]. For the 1D case, it is shown in [67] that

$$\tilde{h}_{\alpha}(x) \sum_n \delta(x - nX) = \tilde{h}_{\alpha}(x) * \left[\sum_n \left(\frac{1}{X} C_{\alpha,2\pi n/X} \right) \delta \left(x + \frac{\pi}{\alpha X} n \right) \right] \quad (2.8)$$

where $C_{\alpha,2\pi n/X} = \exp \left[-j \frac{(2\pi n/X)^2}{4\alpha} \right]$ and

$$\tilde{h}_{\alpha}(x) = \exp(j\alpha x^2) = \sqrt{j\lambda z} \exp \left(-j \frac{2\pi}{\lambda} z \right) h_z(x) \Big|_{z=\frac{\pi}{\lambda\alpha}} \quad (2.9)$$

where

$$h_z(x) = \frac{1}{\sqrt{j\lambda z}} \exp\left(j\frac{2\pi}{\lambda}z\right) \exp\left(j\frac{\pi}{\lambda z}x^2\right) \quad (2.10)$$

is as given in Appendix C. Direct sampling of the quadratic phase function can be used to generate a lenslet array. In [39], lenslet arrays are generated using such a method. However, each lenslet in the generated array may have different phase variation relative to its neighbor lenslet due to the parameters of the designed array [39]. For a certain set of parameters in Eq. (2.8), the term $C_{\alpha,2\pi n/X}$ is constant. Thus, it creates a different modulation for each replica of the original Fresnel pattern. The circular profile of the Fresnel patterns do not change but they are modulated by a different complex number. It is shown in [67] that, by choosing the parameters properly, one can obtain a periodic phase pattern with no phase modulations on the lenslets, so that, each lenslet will have exactly the same Fresnel pattern as its neighbors. It is shown that, if the sampling period is chosen to be equal to $\left(\frac{\pi}{2\alpha r}\right)^{1/2}$ where r is an integer, then the constant $C_{\alpha,2\pi n/X}$ becomes equal to 1, $\forall n$ [67]. Furthermore, if the focal length is chosen as $f = N\frac{X^2}{\lambda}$ [52, 68] to cover the entire normalized local frequency range $[-\pi, \pi)$, in radians, then the impulse train will have a periodicity by a value of NX , where N is the number of pixels along one dimension of the finite 2D discrete array which represents a single lenslet [52]. Thus, we will have a lenslet array with identical lenslets. We want to use identical lenslets in the array because we want to first observe the imaging properties of a discrete lenslet. So, we need to eliminate any phase variations due to the generation of the lenslets.

For some cases we want the freedom of placing the lenslets in the array as we wish. Therefore, we designed a single lenslet pattern and then replicated this pattern one after another to cover the entire SLM surface, instead. Such an approach makes it easier to fit a certain array configuration over the finite size SLM. Even though this method may cause phase jumps at the borders of lenslets, and thus, some unwanted effects, such effects are negligible especially for larger array sizes. Furthermore, generation of lenslets with special phase patterns is easier by using this method [20].

To determine the number of lenslets, given the SLM size we need the discrete array size of a single lenslet pattern. So, when we limit n_1, n_2 in Eq. (2.7) to

be in the interval $[-\frac{N}{2}, \frac{N}{2} - 1]$, we will obtain a single lenslet. If the SLM has $N_1 \times N_2$ pixels, then the number of the lenslets will be $\frac{N_1}{N} \times \frac{N_2}{N}$, where $\frac{N_1}{N}$ and $\frac{N_2}{N}$ are integers [52].

For a setup which requires longer focal length lenslets, we can still use the same SLM with the same lenslet array size, by keeping the lenslet size $N \times N$ the same; thus the Fresnel pattern becomes cropped. Therefore, we will not be able to cover the full local frequency range of $[-\pi, \pi)$ for longer focal length lenslets for such a case. This will introduce blurriness since the light which would be coming from higher angles do not exist as a consequence of cropped lens pattern, and thus, will not be accumulated at the focal point. So, there is a trade-off between longer focal lengths and focused point sharpness if the size of the lenslet is kept fixed [52]. One can easily calculate the range of instantaneous frequencies, which the lenslet can accommodate with such a larger focal length, of the sampled quadratic phase function. For our experiments, we used several lenslet patterns with focal lengths equal to $N \frac{X^2}{\lambda}$ to cover the full local frequency range. In each such pattern, we determined the value of N , which specifies f since λ and X are fixed, and each lenslet is generated according to these parameters. Our device has 1920×1080 (HDTV) pixels with a $8\mu m$ pixel period in each direction. We were able to implement 3×5 , 6×10 and 12×20 element arrays of lenslets which have 360×360 , 180×180 and 90×90 pixels with $43.4mm$, $21.7mm$ and $10.8mm$ focal lengths, respectively, for the same wavelength of $532nm$ [52]. There are some unused pixels on the left and right sides of the SLM with the given size and array configurations; we evenly split this excess area to both ends. We were also able to generate shorter focal length lenslet arrays. However, the resultant imaging quality in the optical experiments with these lenslets were low. This is because the higher order effects (multiple focal points and higher diffraction orders) are dominant thus it does not behave as a good quality lens anymore [52].

2.2 Multiple Focal Points

The SLM acts as a diffractive optical element. The pixelated structure of the SLM causes higher diffraction orders; this is a well known effect [41,67]. However, this is not the only effect that we observe when a discrete quadratic phase function is written on the SLM. For writing any pattern onto the SLM we also need to quantize the sampled pattern. The quantization is a nonlinear process and its consequences are investigated in [69] for the quadratic phase function. Suppose that we have a sampled and quantized Fresnel lens pattern that we want to write on an SLM which has exactly the same number of pixels as the number of samples of the finite size pattern. The Fresnel pattern is like a discrete diffraction pattern of a point source at a distance f . We will call this distance the fundamental focal point. This distance from the lens is also referred as the reference focal [70] and it is also called the critical distance [38]. Between the lenslet and the fundamental focal point, we have to consider the effect of both sampling and quantization together. Quantization will cause multiple focal points over the z -axis. When such a discrete and quantized Fresnel pattern is illuminated by a plane wave and the modulated light is allowed to propagate along the z -axis the light will be concentrated on bright spots on these focal points [69]. So, quantization causes multiple focal planes while sampling causes higher diffraction orders [52,71].

Consider the case of an infinite array of such lenslets, the phase angle of the complex pattern, which is the sampled and quantized Fresnel lenslet array pattern as calculated in the previous section, is written on an hypothetical infinite size phase-only SLM. When the SLM is illuminated by a plane wave and the modulated light is allowed to propagate further away from the fundamental focal length on the z -axis, the periodic array of focused points will be repeated at certain distances [52]. This phenomenon is known as the Talbot effect [72]. When an infinite array of discrete lenslets, each with a size $N \times N$, is written on an infinite size SLM, so called self images of the lenslet array will periodically occur at multiples of Talbot distance given as $z_T = m \frac{(NX)^2}{\lambda} = mNf$ on the z -axis, where NX is the distance between two lenslets (lenslet period), and m is an even integer [72]. Since, the input pattern will be repeated at multiples of z_T ,

fundamental focal point will also be repeated at multiples of z_T . Furthermore, between each Talbot distance at mz_T and $(m + 1)z_T$, there exist other spots at fractions of the Talbot distance [52]. In real life, Talbot effect may or may not be visible physically depending on the length z_T and also on the lenslet array size, and thus on the SLM size. For a sufficiently large array and short z_T , it is possible to observe this effect. For example, in our setup, it is possible to observe the periodic focused spots created by a lenslet array pattern with a 24×40 lenslet array where each lenslet has 45×45 pixels, $f = 5.41\text{mm}$, and the first Talbot distance $z_T + f = 0.492m$ [52].

To relate the physical observations to theoretical analysis, let us consider a hypothetical case: an infinite size analog mask of periodic lenslets consisting of equally spaced impulsive elements is illuminated by a plane wave. We use the Fresnel transform as if it is a valid diffraction model. In reality, this model is valid only for small angle propagation (the paraxial approximation) and such a restriction will not support impulsive patterns since they imply high frequencies [52]. Even if the diffraction model is not the Fresnel model but the accurate Rayleigh-Sommerfeld model, the free space propagating waves still does not support an impulsive pattern, since the plane wave components which superpose to form an impulse should inevitably have both propagating and evanescent components. Frequency components with spatial frequencies (f_x, f_y) on the mask with $\sqrt{f_x^2 + f_y^2} > 1/\lambda$ will not propagate through the space. Therefore, impulsive function cannot be reconstructed by propagating waves. However, here we still conduct a mathematical exercise using impulsive inputs and Fresnel propagation to understand the associated concepts [52].

We start from a Fourier series expansion [69]. For the sake of simplicity, we look at the 1D version of the continuous lens phase function $h_{-\gamma}(x) = \exp(-j\gamma x^2)$ where $\gamma = \frac{\pi}{\lambda f}$. We will also use the Fourier transform of the quadratic phase function. So, we define it for a generic function $h_\alpha(x) = \exp(j\alpha x^2)$ as $\mathcal{H}_\alpha(f_x) = (j\frac{\pi}{\alpha})^{1/2} \exp\left[-j\frac{(2\pi f_x)^2}{4\alpha}\right]$, [67]. Consider that we make a change of variables $u = x^2$. The function $b(u) = \exp(-j\gamma u)$ is a periodic function of u . Now, we introduce a pointwise nonlinearity $\mathcal{T}\{\cdot\}$ to get another periodic function $\phi(u) = \mathcal{T}\{b(u)\}$ and then, we can make a Fourier series analysis of $\phi(u)$ to find a set of coefficients

as

$$a_k = \frac{1}{L} \int_0^L \phi(u) \exp\left(-j \frac{2\pi k}{L} u\right) du, \quad (2.11)$$

where L is the period $\frac{2\pi}{\gamma}$. A commonly used nonlinearity is the staircase function which is investigated in [69]. Following the similar steps in [69], and by substituting back for u , the Fourier synthesis can be written as

$$\begin{aligned} l^Q(x) \triangleq \phi(u)|_{u=x^2} &= \sum_k a_k \exp\left(-j \frac{2\pi k}{L} x^2\right) \\ &= \sum_k a_k \exp\left(-j \frac{\pi}{\lambda f_k} x^2\right) = \sum_k a_k \tilde{h}_{-\gamma_k}(x) \end{aligned} \quad (2.12)$$

where $\gamma_k = \frac{\pi}{\lambda f_k}$ and $l^Q(x)$ is the 1D quantized lenslet function. Eq. (2.12) can be interpreted as many superposed thin lenses with different focal lengths at $f_k = \frac{f}{k}$ and different transparencies indicated by the amplitude a_k . It is possible to design a nonlinear function to achieve a desired allocation of power among the terms of Eq. (2.12) by choosing a_k 's accordingly. Usually, it is desirable to emphasize a_1 and suppress other terms. For example, it is shown in [69] that by increasing the quantization level it is possible to increase the power contributed to the fundamental focal point (larger a_1 with respect to other a_k 's). However, there still exists power contributed to other focal points since a_k 's for $k \neq 1$ are not necessarily zero. Let us concentrate on the imaging properties of a quantized lens with arbitrary a_k 's. When we use such a lens to image an object, due to multiple focal lengths, not only the main image, which is formed by the lens with focal length f , is present, but also there exists images formed by the higher-order lenses with smaller focal lengths [52]. However, these images which are also smaller in size have less power as a consequence of distribution of a_k 's as discussed above, and quickly disperse when they propagate and reach the main image plane [52, 71]. These higher order image planes are referred as the ghosts in [71] and it is noted that $|a_1|^2$ gives the diffraction efficiency of a given SLM. We conducted simulations related to this observation and the results are presented in Sec. 2.3. In our experiments, the quantization is linear with equidistant 256-levels between 0 and 255 to cover the $[0, 2\pi)$ radians phase interval. Subsequently, we convert $l^Q(x)$ to a pixelated form by sampling (multiplying by an impulse train) it first and then convolving the result with a zero-order interpolator (hold) which

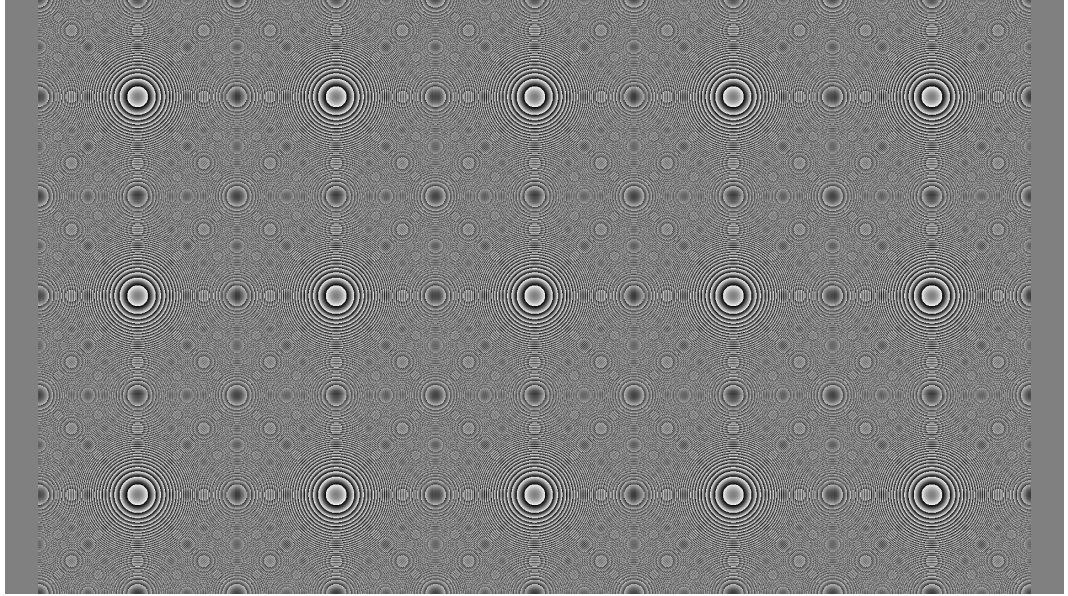


Figure 2.2: 3×5 Lenslet array phase profile on the SLM, each lens has $f = 43.3mm$. There are equal number of unused pixels both at left and right edges. (Reprinted from “Integral imaging using phase-only LCoS spatial light modulators as Fresnel lenslet arrays,” Ali Özgür Yöntem and L. Onural, J. Opt. Soc. Am. A vol. 28, no. 11, pp.2359-2375, 2011. ©2011 OSA.)

has a width equal to the sampling period X where we assumed that there are no gaps between the SLM pixels [52]. In case there are gaps, the analysis should be modified by starting as presented in [70], [41]. Therefore, we can write

$$l^S(x) = \left[p(x)l^Q(x) \sum_n \delta(x - nX) \right] * s(x) . \quad (2.13)$$

The finite size of a lenslet is represented by the aperture function $p(x) = \text{rect}(\frac{x}{NX} + \frac{1}{2})$. $s(x) = \text{rect}(\frac{x}{X})$ is the pixel function, where the rectangular function defined as $\text{rect}(x) = 1$ for $x \in [0, 1)$ and 0 otherwise. Fig. 2.3 shows the angle of $l^S(x)$, modulo 2π . To create the lenslet array, we replicate the function $p(x)l^Q(x)$ by convolving it with an impulse train; this shifts the center of each lenslet in the array such that each lenslet is positioned one next to another:

$$LA(x) = \left\{ \left[p(x)l^Q(x) * \sum_r \delta(x - rx_0) \right] \sum_n \delta(x - nX) \right\} * s(x) , \quad (2.14)$$

where n and r are integers [52]. In Eq. (2.14), we modeled the lenslet array such that there are no gaps between two consecutive lenslets, and thus, the lenslet

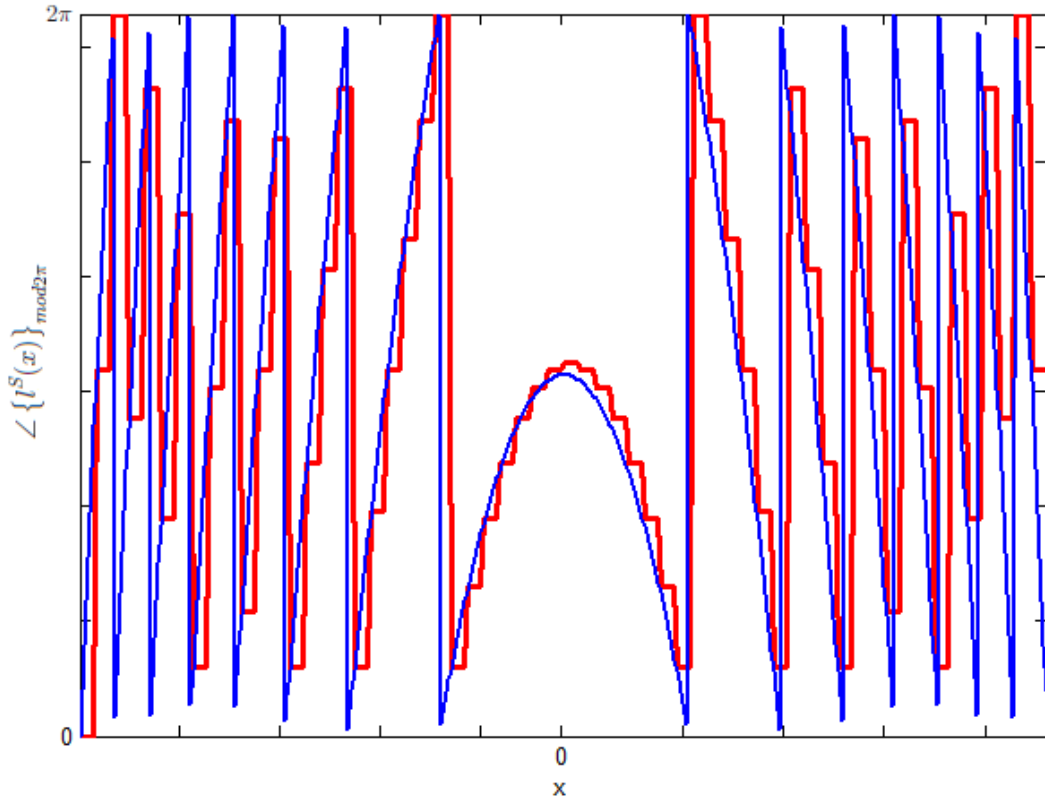


Figure 2.3: Illustration of a quadratic phase function and its sampled and quantized version. Vertical axis shows the phase, mod 2π , while the horizontal axis shows the spatial extent of the function. (Revised from “Integral imaging using phase-only LCoS spatial light modulators as Fresnel lenslet arrays,” Ali Özgür Yöntem and L. Onural, *J. Opt. Soc. Am. A* vol. 28, no. 11, pp.2359-2375, 2011. ©2011 OSA.)

period is equal to the lenslet size. There are N pixels in one direction from the center of one lenslet to next center of the next lenslet. Therefore, the lenslet array period is $x_0 = NX$. The reason for this choice is the finite SLM size: since we have a limited number of pixels, we want to generate as many lenslets as we can without wasting any pixels between the lenslets. Depending on the application, it might be desirable to have gaps between the lenslets. However, the relation between the pixel period and the lenslet period is critical: if this ratio is not an integer, then the focal points from higher diffraction orders, and the multiple focal points due to higher-order lenslets due to nonlinearity will not overlap. They do overlap in our choice as indicated above [52].

Now assume that the lenslet array is illuminated by a plane wave. Then, the complex field just after the infinite size SLM will be given by Eq. (2.14). Therefore, the field that propagates away from the SLM is

$$q(x) = LA(x) * h_z(x) = \int_{\eta} LA(\eta)h_z(x - \eta)d\eta. \quad (2.15)$$

There are two convolutions within the function $LA(x)$. Using the commutative property of the convolution operation we replace the order of the convolutions $s(x)$ and $h_z(x)$ in Eq. (2.15), [41]. So, above equation can be rewritten as,

$$q(x) = \left\{ \left[p(x)l^Q(x) * \sum_r \delta(x - rx_0) \right] \sum_n \delta(x - nX) \right\} * h_z(x) * s(x) \quad (2.16)$$

As a consequence, it is easier to observe the focusing properties of a sampled and quantized lenslet array and explain the effect of the rectangular pixels. Carrying out the convolution by $h_z(x)$ and the function inside the curly brackets, where the evaluation is given in Appendix A, we can rewrite Eq. (2.16) as,

$$q(x) = \sum_k \left\{ \left[P\left(\frac{x}{\lambda f_k}\right) * \frac{x_0}{k} \sum_n \delta\left(x - \frac{n}{k}x_0\right) \right] * \left[\sum_r c_{k,r}(x)\delta(x - rx_0) \right] \right\} * s(x) \quad (2.17)$$

where the distance parameter $z = -f_k$, (i.e. we have the field at the focal distances) to show the effect of multiple focal planes. $P\left(\frac{x}{\lambda f_k}\right)$ is the Fourier transform of the lenslet's pupil function scaled with $\frac{x}{\lambda f_k}$; so, for the 1D analysis we have been carrying out, it is given by $\frac{k}{X}\text{sinc}\left(\frac{x}{X}k\right)$ where $\text{sinc}(x) = \frac{\sin(x)}{x}$. It represents the effect on the diffraction due to the limited aperture size of the lenslet. The constants are given as $\frac{\lambda f_k}{X} = \frac{NX}{k} = \frac{x_0}{k}$ and $c_{k,r}(x) = a_k h_{f_k}(x - rx_0)$. It is shown in [41] that, the output of the diffraction from a single lenslet is the convolution of the Fourier transform of the pupil function and the pixel function, which introduces an inherent apodization [41]. This observation still holds for an array of lenslets shown by Eq. (2.17), as expected [52].

In Eq. (2.17), the impulse train indexed by n is due to the sampling of the lenslet and this introduces multiple diffraction orders. At the fundamental focal plane, that is when $k = 1$, we observe that the separation of higher diffraction orders of focused spots of a lenslet is x_0 . In our cases, this period matches

the impulse train indexed by r , which is present due to the separation of the lenslets. The interesting case occurs due to the effect of quantization since it causes multiple focal points. Note that the impulse train indexed by n , when $k \neq 1$, introduces shifts, which are a fraction of x_0 . So, the spots appear on the x -axis with x_0/k distance away from each other on each focal plane f/k . Since all impulse trains are infinite in extent, we see that the focused spots at a certain distance are periodic over the x -axis. So, Eq. (2.17) is a collection of points in three dimensional free space [52].

Eq. (2.17) can be illustrated by Fig. 2.4, where the circles along the optical axis of each lenslet specifies the multiple focal points, and along the x -axis, at each focal length, periodically positioned spots are present due to higher diffraction orders. For a single lenslet pattern in the lenslet array, any focused spot it yields along the x -axis, except the ones that lie on its optic axis, are higher diffraction orders at the focal planes. Thus, each lenslet creates multiple depth focal points, together with higher diffraction orders. In other words, when the generated Fresnel field from the impulsive pattern propagates in the free space, at certain distances, again periodic and impulsive patterns are formed [67].

Now we look at the case of a finite size SLM. In this case, the locations of the focused spots will not change. However, limited SLM aperture will introduce a low pass filter over the intensities of these spots. Depending on the aperture size, the intensities of the focused spots are modulated by a sinc function $W\left(\frac{x}{\lambda f_k}\right) = \frac{Kx_0}{\lambda f_k} \text{sinc}\left(\frac{x}{\lambda f_k} Kx_0\right) = \frac{Kk}{X} \text{sinc}\left(\frac{xKk}{X}\right)$. This is due to a rectangular window function $w(x) = \text{rect}\left(\frac{x}{Kx_0}\right)$, which is the aperture function of the SLM that contains K discrete lenses along one direction. Such a modulation will diminish the power associated with some of these multiple focused spots and thus reduce their visibility [52].

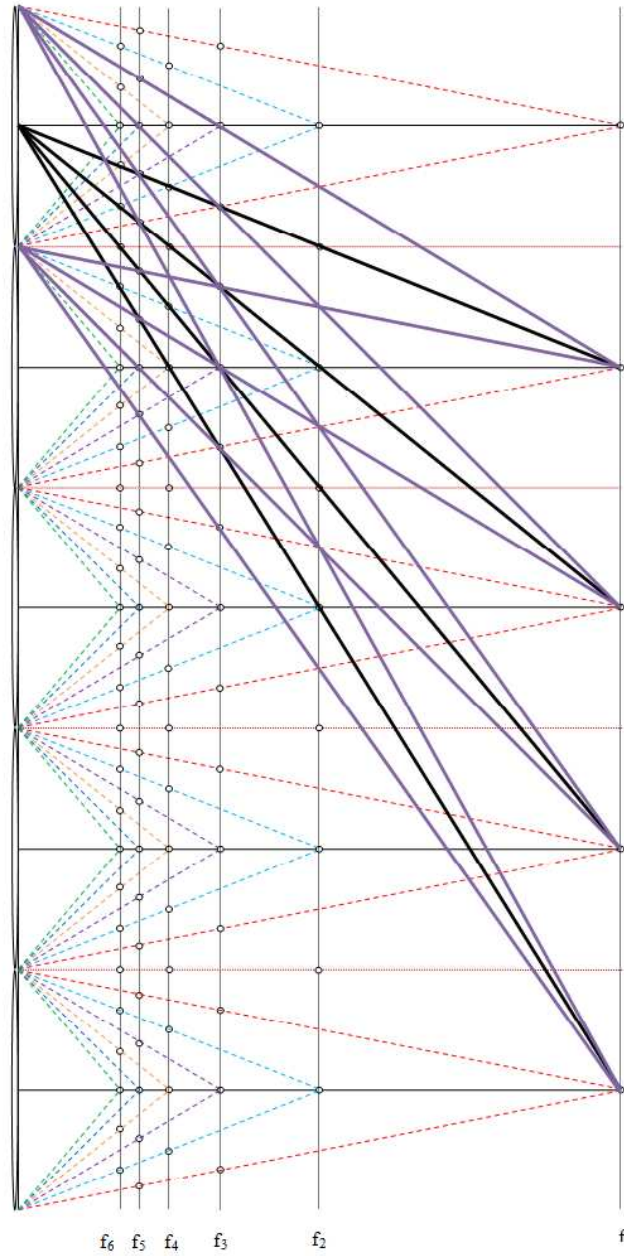


Figure 2.4: Multiple focal points and higher diffraction orders. The focal points are shown by small circles. Dashed lines show the converging waves towards multiple focal points from a single lenslet. Solid lines show the converging waves towards higher diffraction orders at the fundamental focal plane. (Not all lines are shown in order not to clutter the drawing.) (Reprinted from “Integral imaging using phase-only LCoS spatial light modulators as Fresnel lenslet arrays,” Ali Özgür Yöntem and L. Onural, *J. Opt. Soc. Am. A* vol. 28, no. 11, pp.2359-2375, 2011. ©2011 OSA.)

2.3 Numerical Results

As we mentioned in the previous section, we performed a series of computer simulations to show the multiple focuses and diffraction orders. First we ran the simulations for a single lenslet. The lenslet profile is generated using Eq. (2.7). As described in Sec. 2.1, we determined N , the total number of samples along one dimension of the lenslet, by using the relation $f = N\frac{X^2}{\lambda}$ where $\lambda = 532nm$ and $X = 8\mu m$. To obtain a single lenslet, we limit n_1, n_2 in Eq. (2.7) to be in the interval $[-\frac{N}{2}, \frac{N}{2} - 1]$. For a lenslet with $f = 14.4mm$, N is equal to 120 and for a lenslet with $f = 43.3mm$, N is equal to 360. We want to show the effect of quantization on the lenslet phase ($\text{mod } 2\pi$) by mapping this data linearly between 0 and 255. The results for these two single lenslets are shown in Fig. 2.5 and Fig. 2.7 respectively [52].

We assumed a plane wave as the incident light on the lenslets whose phase patterns are shown in Fig. 2.5 and Fig. 2.7. We performed wave propagation simulations using the Fresnel diffraction kernel. We use the DFT method to compute the convolution to find outputs of the discrete systems. However, our discretized signals have a support that span both sides of the axes; i.e. n_1, n_2 can take zero, positive or negative values. Therefore, we must modify the commonly used DFT definition to operate also on such signals [52, 73]. Suppose that for a finite length signal $x_D[\mathbf{n}]$, $n_1, n_2 = -N/2, \dots, N/2 - 1$ we define the modified finite length $D\hat{F}T$, $X_D[\mathbf{k}] = D\hat{F}T\{x_D[\mathbf{n}]\}$, $k_1, k_2 = -N/2, \dots, N/2 - 1$ as follows: Let the periodic $\tilde{X}_D[\mathbf{k}]$ be given by,

$$\tilde{X}_D[\mathbf{k}] = \sum_{n_1=0}^{N-1} \sum_{n_2=0}^{N-1} \tilde{x}_D[\mathbf{n}] e^{-j\frac{2\pi}{N}\mathbf{k}^T\mathbf{n}} \quad k_1, k_2 \in (-\infty, \infty) \quad (2.18)$$

and k_1, k_2 are integers. Here, $\tilde{X}_D[\mathbf{k}]$ and $\tilde{x}_D[\mathbf{n}]$ are periodic extensions of finite length $X_D[\mathbf{k}]$ and $x_D[\mathbf{n}]$, respectively, which are given as, $\tilde{X}_D[k_1 - N/2, k_2 - N/2] = X_D[(k_1)_{\text{mod}N} - N/2, (k_2)_{\text{mod}N} - N/2]$, and $\tilde{x}_D[n_1 - N/2, n_2 - N/2] = x_D[(n_1)_{\text{mod}N} - N/2, (n_2)_{\text{mod}N} - N/2]$, where n_1, n_2 are integers in $(-\infty, \infty)$ and consequently, $X_D[\mathbf{k}]$ is one period over $k_1, k_2 = -N/2, \dots, N/2 - 1$ of $\tilde{X}_D[\mathbf{k}]$ and $x_D[\mathbf{n}]$ is one period over $n_1, n_2 = -N/2, \dots, N/2 - 1$ of $\tilde{x}_D[\mathbf{n}]$ [73]. In order to avoid aliasing that might be caused

by the periodicity associated with DFT, while using this method, the computation window size should be selected sufficiently larger than the signal window in both directions. Outside the signal window, we chose to pad the computation window with zeros (opaque borders). Thus, we compute the linear convolution of the signals by approximating the circular convolution by padding zeros in the computation array. Moreover, this way, we simulate the case where those points on the object surface are the only possible source points. The Fresnel diffraction kernel is used to model wave propagation. 2D $D\hat{F}T$ and 2D $ID\hat{F}T$ of the matrices are computed using 2D FFT and 2D IFFT algorithms, respectively [52, 73].

In order to speed up the computations, we used the Fresnel kernel in the spatial frequency domain given by Eq. (2.3). We discretize Eq. (2.3) by substituting \mathbf{f} with $\mathbf{U}\mathbf{k}$ and we obtain

$$g_{D,\theta}[\mathbf{k}] \triangleq H_z^{Fr}(\mathbf{f}) \Big|_{\mathbf{f}=\mathbf{U}\mathbf{k}} = \exp(-j\theta\mathbf{k}^T\mathbf{U}^T\mathbf{U}\mathbf{k}) \quad (2.19)$$

where $\mathbf{k} = [k_1 \ k_2]^T$ and $k_1, k_2 = -N/2, \dots, N/2 - 1$, $U = \begin{bmatrix} 1/(NX) & 0 \\ 0 & 1/(NX) \end{bmatrix}$ is the 2D rectangular sampling matrix in the spatial frequency domain. N is the total number of pixels along one side of the discrete 2D calculation array, X is the spatial sampling period and $\theta = \pi\lambda z$ and z is the propagation distance parameter. We omitted the phase constant, which appears in Eq. (2.3), in order not to clutter the computations [52, 73].

Let us denote the signal window by $t[\mathbf{n}]$. This is centered inside the computation window, $w_t[\mathbf{n}]$. The output of the propagation (diffraction field) is given by

$$t_{d_i}[\mathbf{n}] = ID\hat{F}T \left\{ D\hat{F}T \{w_t[\mathbf{n}]\} g_{D,\chi_i}[\mathbf{k}] \right\} \quad (2.20)$$

where $\mathbf{n} = [n_1 \ n_2]^T$ and $\mathbf{k} = [k_1 \ k_2]^T$ represent the discrete spatial domain variables and the discrete spatial frequency domain variables, respectively, and n_1, n_2, k_1, k_2 are integers where we choose the range for n_1, n_2, k_1 and k_2 as $[-360, 359]$. The parameters χ_i is given as $\pi\lambda z_i$. Our computation window, is 720-sample wide in both directions which is six times the lenslet with $f = 14.4mm$ and two times the lenslet with $f = 43.3mm$ [52].

The simulation calculates the field at certain distances until the fundamental focal point. So, we sampled the z -axis with equal separations of $z_i = i\frac{f}{L}$ in the interval $\left[0, \frac{(L-1)f}{L}\right]$ where $L = 500$ is the total number of samples along the z -axis for each $\chi_i = \pi\lambda z_i$. For each distance, z_i , a 2D diffraction pattern, $t_{d_i}[\mathbf{n}]$, is obtained. So, by combining all such 2D diffraction patterns, we obtain a 3D diffraction volume. We are interested in the locations of focal points. For display purposes, we take the 2D cross-section of this 3D field, that is, we extracted the discrete values on the n_2 -axis at $n_1 = 0$ at each z . The results of the propagation with the constraints explained above are shown in Fig. 2.6 and in Fig. 2.8 for lenslets with focal lengths $14.4mm$ and $43.3mm$, respectively. We converted the sample values in the 2D array to actual physical dimensions and labeled the axes in the figures, accordingly. The multiple focal points and diffraction orders are clearly seen in the xz -plane, as expected [52].

Now we proceed to simulate a lenslet array by limiting the lenslet array pattern in the interval $\left[-\frac{3N}{2}, \frac{3N}{2} - 1\right]$ (three lenslets on each axis). Again we simulated the propagation of the input lenslet array phase pattern illuminated by a plane wave. As in the previous simulations, we obtained the 2D (x, z) cross-section of the propagated field. The results of the free space propagation for this lenslet array is presented in Fig. 2.10. Each lenslet in the array has a focal length of $14.4mm$. We used the same equation, Eq. (2.20), to calculate the diffraction field. This time, a periodic input pattern at the input yielded periodic diffraction orders of multiple focal points [67]. The figure shows that by adding more and more lenslets, we can observe the phenomenon as described in the analysis given in Sec. 2.2, where the theoretical results are presented by Eq. (2.17) [52].

As mentioned in Sec. 2.2, we showed that the multiple image planes are associated with the multiple focal length phenomenon due to nonlinearity introduced by quantization. To show this effect, we used a 3×3 lenslet array, each lenslet having a focal length of $43.3mm$. The window size of the lenslet array, $LA_D[\mathbf{n}]$, is 1080×1080 samples. The entire computation window size is 1920×1920 samples. The lenslet array is centered in the computation array, $w_{LA}[\mathbf{n}]$, of size 1920×1920 samples with zeros are padded around the lenslet array. The mask is letter "A", which is centered again in a computation array of size 1920×1920 samples. The

background is black while the letter is white. We multiplied this mask with a normally distributed pseudorandom phase to simulate a diffuse object [52]. To obtain the elemental images at the multiple image planes, we first computed the propagation result, $t_{d_1}[\mathbf{n}]$, from the input $w_t[\mathbf{n}]$ until the lenslet array plane, where the propagation distance is $4f$. Then, we multiplied the propagated field with the pixelated and quantized lenslet array profile, $w_{LA}[\mathbf{n}]$. And then, we propagated the resulting pattern, $t_{d_2}[\mathbf{n}]$, to two different distances $4f/3$ and $4f/7$ to obtain $t_{d_3}[\mathbf{n}]$ and $t_{d_4}[\mathbf{n}]$ respectively. The entire simulation can be summarized by

$$\begin{aligned}
t_{d_1}[\mathbf{n}] &= ID\hat{F}T \left\{ D\hat{F}T \{w_t[\mathbf{n}]\} g_{D,\alpha}[\mathbf{k}] \right\} , \\
t_{d_2}[\mathbf{n}] &= t_{d_1}[\mathbf{n}]w_{LA}[\mathbf{n}] , \\
t_{d_3}[\mathbf{n}] &= ID\hat{F}T \left\{ D\hat{F}T \{t_{d_2}[\mathbf{n}]\} g_{D,\beta_1}[\mathbf{k}] \right\} , \\
t_{d_4}[\mathbf{n}] &= ID\hat{F}T \left\{ D\hat{F}T \{t_{d_2}[\mathbf{n}]\} g_{D,\beta_2}[\mathbf{k}] \right\} .
\end{aligned} \tag{2.21}$$

where $\alpha = \pi\lambda 4f$, $\beta_1 = \pi\lambda(4f/3)$ and $\beta_2 = \pi\lambda(4f/7)$ and where n_1, n_2, n_3, n_4 are in the interval $[-960, 959]$ [52]. In Fig. 2.11, the image obtained by taking the absolute value of $t_{d_3}[\mathbf{n}]$ is shown. As it can be seen from the figure that there are nine elemental images due to nine lenslets [52]. There is a background noise which is present because of the out of focus terms, which are caused by the multiple focal length properties of the lenslets where it is theoretically given by the term $\sum_k a_k \mathcal{H}_{-\gamma_k}(\frac{x}{\lambda g})$ in Eq. (3.11), at this distance. At this image plane, which we call the main image plane, the images of “letter A” are brighter. Thus their visibility is not disturbingly affected by the superimposed out of focus images. When we focus to the other distance, $4f/7$, we obtain Fig. 2.12 which shows the absolute value of $t_{d_4}[\mathbf{n}]$. At this distance the “letter A” is again focused, as expected. On this plane, we observe twenty five images. Nine of them are shown in Fig. 2.8 by squares. These are due to the multiple focal point property of the lenslets [52]. However, there are intermediate images between the images inside the squares. These are present due to the higher diffraction orders created by the pixelated structure of the lenslets [52]. There are similar distortions at this imaging plane as in the main image plane. Since on this plane the images are smaller, thus they have small power, the out of focus fringes degrade the visibility significantly. So, a zoomed in version of the central elemental images and the intermediate image right to it are shown in Fig. 2.13 [52].

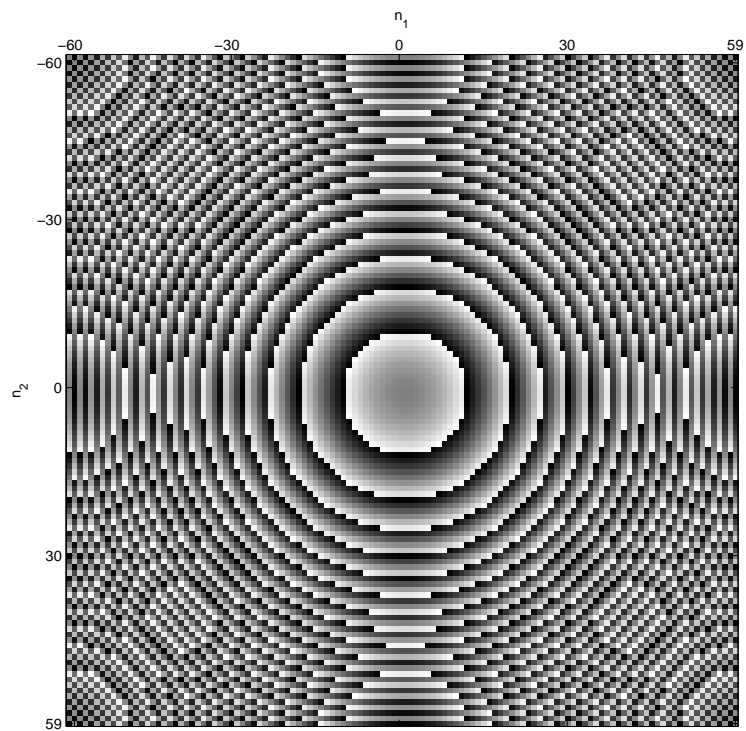


Figure 2.5: Pixelated and quantized lens with $f = 14.4mm$. Sampling period is $8\mu m$, $\lambda = 532nm$ and array dimension is 120×120 pixels. (Reprinted from “Integral imaging using phase-only LCoS spatial light modulators as Fresnel lenslet arrays,” Ali Özgür Yöntem and L. Onural, J. Opt. Soc. Am. A vol. 28, no. 11, pp.2359-2375, 2011. ©2011 OSA.)

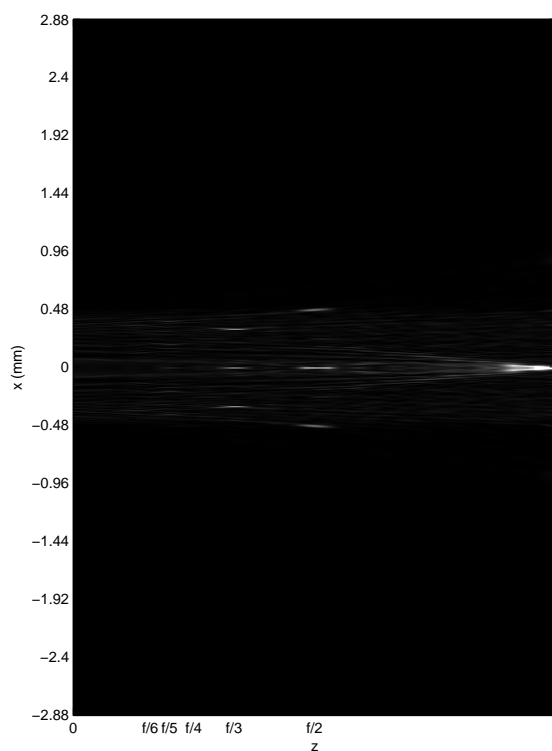


Figure 2.6: Magnitude square of the cross-section of the field due to the pixelated and quantized lenslet, with $f = 14.4\text{mm}$, under plane wave illumination. The SLM is on the left. The bright areas indicate the multiple focal points and higher diffraction orders. The brightest area on the right is the fundamental focal point. (For visual purposes, we adjusted the brightness of the figure.) (Reprinted from “Integral imaging using phase-only LCoS spatial light modulators as Fresnel lenslet arrays,” Ali Özgür Yöntem and L. Onural, J. Opt. Soc. Am. A vol. 28, no. 11, pp.2359-2375, 2011. ©2011 OSA.)

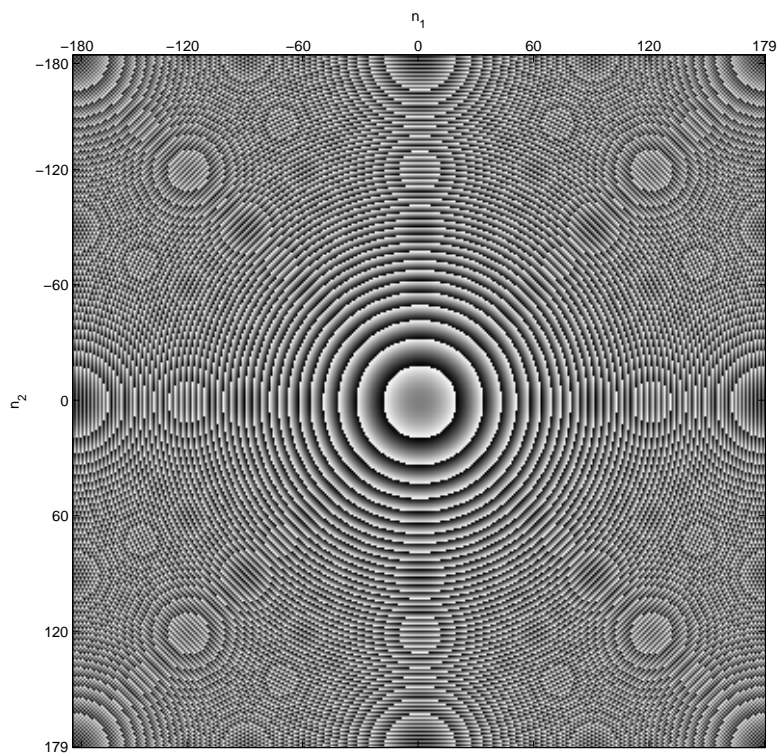


Figure 2.7: Sampled lens with $f = 43.3mm$. Sampling period is $8\mu m$, $\lambda = 532nm$ and array dimension is 360×360 pixels. (Reprinted from “Integral imaging using phase-only LCoS spatial light modulators as Fresnel lenslet arrays,” Ali Özgür Yöntem and L. Onural, J. Opt. Soc. Am. A vol. 28, no. 11, pp.2359-2375, 2011. ©2011 OSA.)

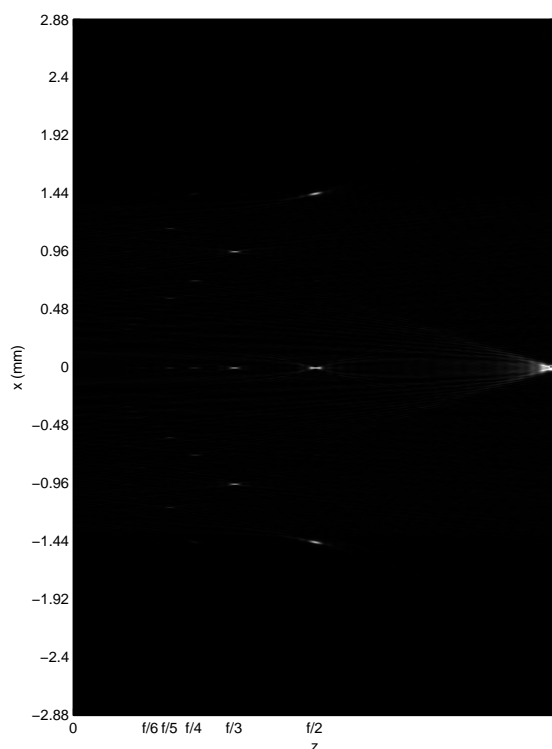


Figure 2.8: Magnitude square of the cross-section of the field due to the pixelated and quantized lenslet, with $f = 43.3\text{mm}$, under plane wave illumination. The bright areas indicate the multiple focal points and higher diffraction orders. The brightest area on the right is the fundamental focal point. (For visual purposes, we adjusted the brightness of the figure.) (Reprinted from “Integral imaging using phase-only LCoS spatial light modulators as Fresnel lenslet arrays,” Ali Özgür Yöntem and L. Onural, J. Opt. Soc. Am. A vol. 28, no. 11, pp.2359-2375, 2011. ©2011 OSA.)

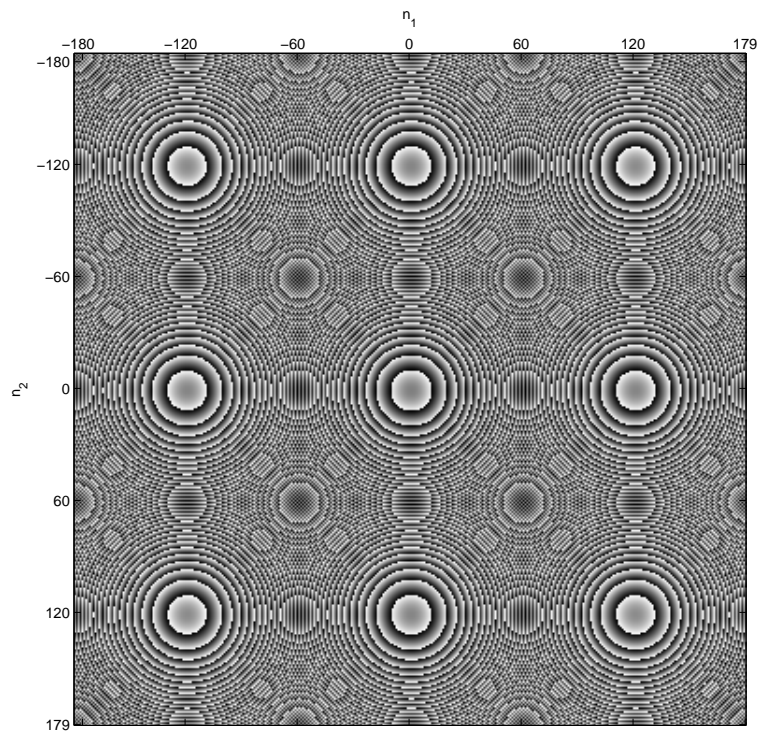


Figure 2.9: Array of lenslets consisting of pixelated lenslets with $f = 14.4mm$. Total array size is 360×360 pixels. Each lenslet in the array has the same properties defined as in Fig. 2.5. The array can be obtained either by replicating a single lenslet in both directions or by intentionally introducing an aliasing in the calculation of a pattern for an array with dimensions having 360×360 pixels and a focal length of $14.4mm$. (Reprinted from “Integral imaging using phase-only LCoS spatial light modulators as Fresnel lenslet arrays,” Ali Özgür Yöntem and L. Onural, J. Opt. Soc. Am. A vol. 28, no. 11, pp.2359-2375, 2011. ©2011 OSA.)

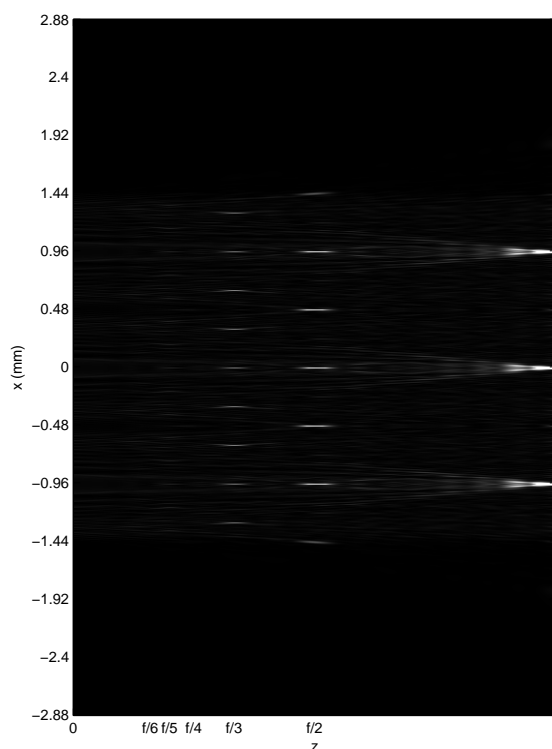


Figure 2.10: Magnitude square of the cross-section of the field due to the array of lenslets consisting of sampled lenslets, with $f = 14.4\text{mm}$, under plane wave illumination. Bright areas indicate the multiple focal points and higher diffraction orders. The brightest areas on the right are the fundamental focal points corresponding to each lenslet. (For visual purposes, we adjusted the brightness of the figure.) (Reprinted from “Integral imaging using phase-only LCoS spatial light modulators as Fresnel lenslet arrays,” Ali Özgür Yöntem and L. Onural, J. Opt. Soc. Am. A vol. 28, no. 11, pp.2359-2375, 2011. ©2011 OSA.)

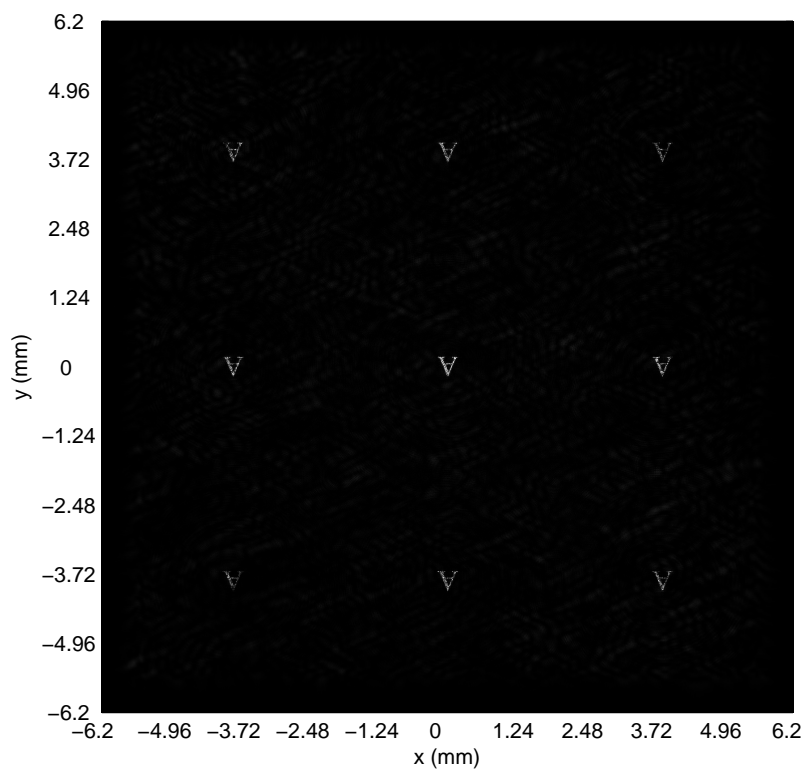


Figure 2.11: Image of the absolute value of $d_3[\mathbf{n}]$. There are nine elemental images due to nine lenslets of the letter “A”. There is a background noise due to the random phase on the input mask plus the out of focus images introduced the multiple focal length properties of the lenslets. The noise do not effect the images’ visibility too much. (For visual purposes, we adjusted the brightness of the figure.) (Reprinted from “Integral imaging using phase-only LCoS spatial light modulators as Fresnel lenslet arrays,” Ali Özgür Yöntem and L. Onural, J. Opt. Soc. Am. A vol. 28, no. 11, pp.2359-2375, 2011. ©2011 OSA.)

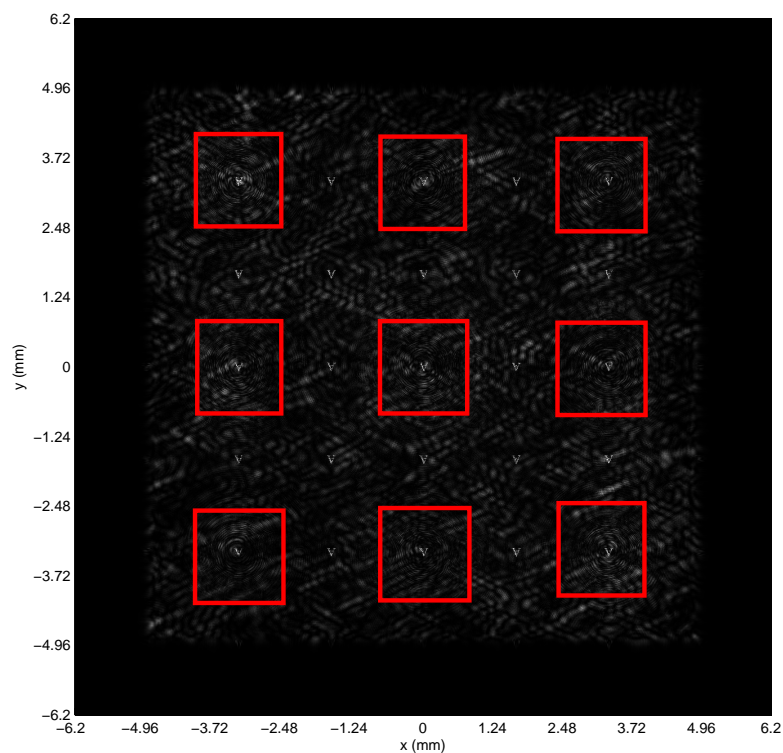


Figure 2.12: Image of the absolute value of $d_4[\mathbf{n}]$. The elemental images, which are depicted inside the rectangles, of the letter “A” are seen together with the higher diffraction orders between the elemental images. A zoomed in version of the central elemental image is given in Fig. 2.13. We observe a similar background noise. However, the visibility of elemental images are now degraded significantly due to the noise. This is because of the smaller size elemental images with less power. (For visual purposes, we adjusted the brightness of the figure.) (Reprinted from “Integral imaging using phase-only LCoS spatial light modulators as Fresnel lenslet arrays,” Ali Özgür Yöntem and L. Onural, J. Opt. Soc. Am. A vol. 28, no. 11, pp.2359-2375, 2011. ©2011 OSA.)

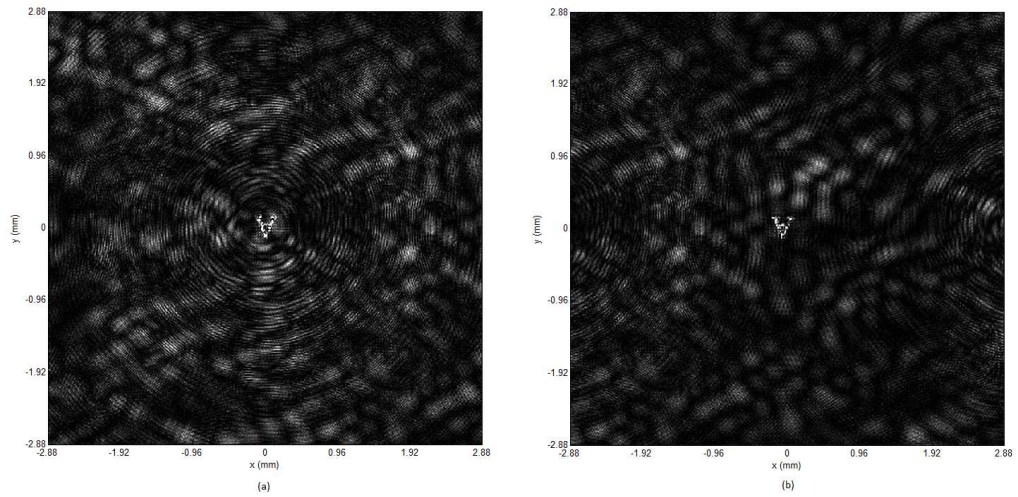


Figure 2.13: (a) Zoomed in elemental image corresponding to the central part of Fig. 2.12. (b) Zoomed in elemental image corresponding to the image right to the central part of Fig. 2.12. (For visual purposes, we adjusted the brightness of the figure.) (Reprinted from “Integral imaging using phase-only LCoS spatial light modulators as Fresnel lenslet arrays,” Ali Özgür Yöntem and L. Onural, J. Opt. Soc. Am. A vol. 28, no. 11, pp.2359-2375, 2011. ©2011 OSA.)

Chapter 3

ANALYSIS OF INTEGRAL IMAGING CAPTURE SYSTEM WITH DIGITAL LENS ARRAY

3.1 Capture System Analysis

This section provides the analytical results which give the elemental images of a 3D object defined by impulsive source points. We choose to represent a 3D object by a number of regularly located slices along the optical axis and at each slice we have object points defined as 2D impulsive source points. In the analysis of the capture system we start from the light which propagates from an object to the SLM plane. The propagated field is then multiplied with the phase profile, which is the lenslet array profile written on the SLM. Resulting field is then propagated to the recording plane. We will also follow a similar derivation steps as in Sec. 2.2 with the additional step of the calculation of the propagation from the object. The object field arriving at the SLM plane replaces the plane wave illumination used in the formulation of the previous section. Again we will use the Fresnel based wave propagation model. For simplicity, a 3D input object is modeled as a point cloud. Here we again assume that in the derivations the SLM

has impulsive pixels and add the effect of rectangular pixels later. The capture system scheme is shown in Fig. 3.1. The distance d is measured from a chosen theoretical reference plane on which the closest point on the object to the lenslet array plane is located. The distance g is measured from the lenslet array plane to the CCD plane. These distances are chosen such that they satisfy the imaging equation $1/f = 1/d + 1/g$ for a single lenslet with focal length f .

The point cloud, which is the input of the system, is defined as

$$t(x, z) = \sum_i t_i \delta(x - x_i, z - z_i) . \quad (3.1)$$

t_i 's are the complex valued source amplitudes with uniform magnitude. Therefore, we assume that the object consists of self-luminous point sources. The complex field just before the lenslet array is given by the sum of the convolutions of the propagation kernel with each point source in the point cloud. We define the propagation distance for each point as $z_i = d + \Delta z_i$. On the lenslet array plane, since the physical device consists of pixels, we assume that the light falling onto a pixel is integrated to yield a constant value. Thus, we get the propagated field at the lenslet array plane as,

$$\begin{aligned} h_{z_i}^{LP}(x) &= t_i h_{z_i}(x) * s(x) * \delta(x - x_i) \\ &= t_i \left[\int h_{z_i}(x - \eta) s(\eta) d\eta \right] * \delta(x - x_i) \\ &= t_i \left[\int h_{z_i}(x) \exp(-j2\alpha_i x \eta) \hbar_{\alpha_i}(\eta) s(\eta) d\eta \right] * \delta(x - x_i) \\ &= t_i h_{z_i}(x) \left[\int \hbar_{\alpha_i}(\eta) s(\eta) \exp(-j2\alpha_i x \eta) d\eta \right] * \delta(x - x_i) \\ &= \left\{ t_i h_{z_i}(x) \left[\mathcal{H}_{\alpha_i} \left(\frac{x}{\lambda z_i} \right) * S \left(\frac{x}{\lambda z_i} \right) \right] \right\} * \delta(x - x_i) \\ &= [t_i h_{z_i}(x) V(x)] * \delta(x - x_i) \\ &= t_i h_{z_i}(x - x_i) V(x - x_i) \end{aligned} \quad (3.2)$$

where $\alpha_i = \frac{\pi}{\lambda z_i} = \frac{\pi}{\lambda(d + \Delta z_i)}$ and $V(x) = (j\lambda z_i)^{1/2} \hbar_{-\alpha_i}(x) * S \left(\frac{x}{\lambda z_i} \right)$ where we used the Fourier transform property, $\mathcal{H}_{\alpha_i} \left(\frac{x}{\lambda z_i} \right) = \left(j \frac{\pi}{\alpha_i} \right)^{1/2} \exp \left(-j \frac{(2\pi x / (\lambda z_i))^2}{4\alpha_i} \right) = (j\lambda z_i)^{1/2} \hbar_{-\alpha_i}(x)$, for quadratic phase functions given in [67]. The propagated field is the low pass filtered version of $h_g(x)$ by the pixel function $s(x)$. The samples

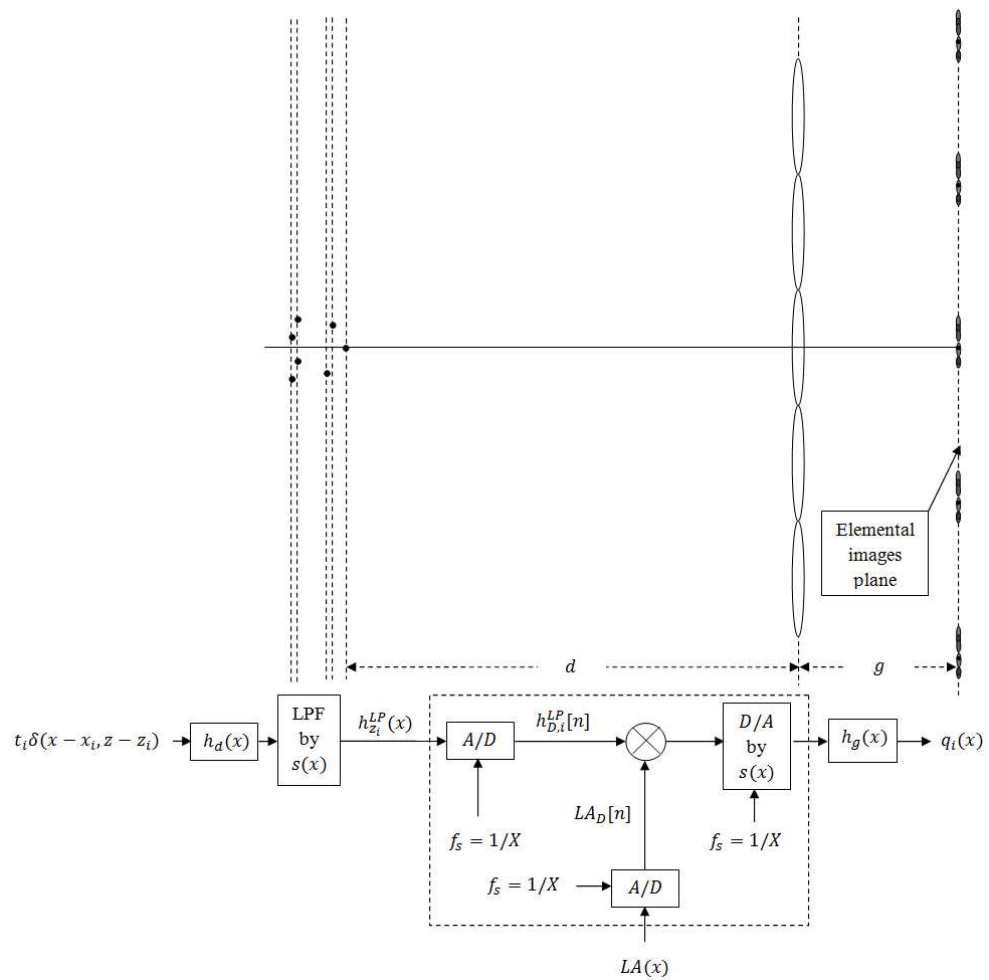


Figure 3.1: Capture setup (Revised from “Integral imaging using phase-only LCoS spatial light modulators as Fresnel lenslet arrays,” Ali Özgür Yöntem and L. Onural, J. Opt. Soc. Am. A vol. 28, no. 11, pp.2359-2375, 2011. ©2011 OSA.)

of this field,

$$h_{D,i}^{LP}[n] \triangleq h_{z_i}^{LP}(x) \Big|_{x=nX} \quad (3.3)$$

represent the discrete pixel values on the SLM. Each such sample is then multiplied by the discrete lenslet array phase distribution $LA_D[n]$, which is given by

$$LA_D[n] = \left[p(x) l^Q(x) * \sum_r \delta(x - rx_0) \right]_{x=nX} \cdot \quad (3.4)$$

The resulting discrete complex field is converted to an analog signal by convolving with the pixel function. Next, this analog complex field is propagated for a distance g to find the field on the recording plane. Finally, we take the magnitude square of the field to simulate the intensity recording.

First let us look at the impulse response of the system for an impulse located at (x_i, z_i) . The impulse response of the capture system can be written as

$$q_i(x) = \left\{ \sum_n h_{D,i}^{LP}[n] LA_D[n] \delta(x - nX) \right\} * s(x) * h_g(x) \cdot \quad (3.5)$$

The pixel function, $s(x)$, converts the discrete pattern into a continuous field by zero-order hold interpolation. Since the systems are linear and shift invariant, we can interchange the order of the convolutions $s(x)$ and $h_{z_i}(x)$ given as,

$$q_i(x) = \left\{ \sum_n h_{D,i}^{LP}[n] LA_D[n] h_g(x - nX) \right\} * s(x) \cdot \quad (3.6)$$

So, we first find the propagation result, where the details of the derivation are given in Appendix B. The final result of the impulse response can be written as (see Appendix B)

$$q_i(x) = P_i \left(\frac{x}{\lambda g} \right) * s(x) * \left[\sum_k a_k \mathcal{H}_{-\gamma_k} \left(\frac{x}{\lambda g} \right) \right] * x_g \sum_n \delta(x - nx_g) * \Upsilon_i(x) \cdot \quad (3.7)$$

In Eq. (3.7), the last term

$$\begin{aligned} \Upsilon_i(x) = \sum_r c(x) \left\{ \left\{ v \left(\frac{x}{\lambda g} \right) \exp [j2\beta(x_i - rx_0)x] \right\} \right. \\ \left. * \delta \left[x - \left(1 + \frac{g}{z_i} \right) rx_0 + \frac{g}{z_i} x_i \right] \right\} \quad (3.8) \end{aligned}$$

where we obtain $v\left(\frac{x}{\lambda g}\right) = (j\lambda z_i)\tilde{h}_\beta\left(\sqrt{\frac{z_i}{g}}x\right)s\left(-\frac{z_i}{g}x\right)$ by using again the Fourier transform property, $\mathcal{H}_{-\alpha_i}\left(\frac{x}{\lambda g}\right) = \left(j\frac{\pi}{\alpha_i}\right)^{1/2}\exp\left(j\frac{(2\pi x/(\lambda g))^2}{4\alpha_i}\right) = (j\lambda z_i)^{1/2}\tilde{h}_\beta\left(\sqrt{\frac{z_i}{g}}x\right)$, for quadratic phase functions given in [67] and $c(x) = h_g(x - rx_0)t_i h_{z_i}(x_i - rx_0)$, is a weighted impulse train which gives the perfect mapping (imaging) at locations $\left(1 + \frac{g}{z_i}\right)rx_0 - \frac{g}{z_i}x_i$ of the input point to multiple output points. This would be the imaging of a lenslet array consisting of perfect thin lenses. However, because of the low pass filtering caused by the pixel function at the input, this term gives blurred spots. The term $x_g \sum_n \delta(x - nx_g)$, which is a scaled impulse train due to sampling of the lenslets, causes multiple diffraction orders and it replicates the points at locations $\left(1 + \frac{g}{z_i}\right)rx_0 - \frac{g}{z_i}x_i$ where $\left(1 + \frac{g}{z_i}\right)x_0$ is the elemental image separation and $-\frac{g}{z_i}x_i$ is the image point location. x_g is given as $\frac{\lambda g}{X}$. Substituting $(1/f - 1/d)^{-1}$ for g we get $x_g = \left(\frac{1}{1-f/d}\right)x_0$ which is equal to $(1 + g/d)x_0$. For sufficiently large d and small object depth, the elemental image separation $\left(1 + \frac{g}{z_i}\right)x_0 \approx \left(1 + \frac{g}{d}\right)x_0$. So, we get nearly the same separation periodicity for the elemental images and the higher diffraction orders of the elemental images. For those object points near to the distance d , we will have elemental images which are imaged well. For other object points, which are further away from d , the separation of the higher diffraction orders will be slightly less than the elemental images separation. This might cause intermingled elemental images. In reality, for the central diffraction order, a human observer may not notice this effect. However, for higher orders this artefact might be noticeable. Furthermore, these far away points might be out of focus at the imaging plane because of the limited depth of field, caused by the term $P_i\left(\frac{x}{\lambda g}\right)$; this will be explained later. Thus, for a certain setup, it is possible to obtain good elemental images by satisfying the above constraints. Moreover, higher diffraction orders will have less intensity because of the rectangular pixels and the SLMs' finite size as discussed previously in Sec. 2.2. So, these artefacts will not disturb the elemental images at the central diffraction order. The term $\sum_k a_k \mathcal{H}_{-\gamma_k}\left(\frac{x}{\lambda g}\right)$ is introduced because of the multiple focal point property of the lenslets. In fact, this is another artefact term at the main image plane caused by the out of focus small images formed at multiple image planes related to the focal distances f/k of higher-order lenslets due to quantization. $s(x)$ is the pixel

function, which introduces an inherent apodization [41]. The first term in the Eq. (3.7), $P_i\left(\frac{x}{\lambda g}\right) = P\left(\frac{x}{\lambda g}\right) * \mathcal{H}_{\theta_i}\left(\frac{x}{\lambda g}\right)$, is the generalized pupil function which takes defocussing due to different depths of the point sources at the input plane into account. The function $\mathcal{H}_{\theta_i}\left(\frac{x}{\lambda g}\right)$ is responsible for the defocussing. $P\left(\frac{x}{\lambda g}\right)$ is the Fourier transform of the pupil function. This function is a limiting factor for the extent of $q_i(x)$. The constant θ_i is given as $\beta + \alpha_i = -\frac{\pi}{\lambda} \frac{\Delta z_i}{d(\Delta z_i)}$. Therefore, the overall response of the system to the point cloud is given by

$$q(x) = \sum_i q_i(x) \quad (3.9)$$

by adding the response of each source in the point cloud. Here we assume that each point is a source and therefore the field on it is independent of other source points. Finally, in order to obtain the elemental images, we simulate the intensity recording process by taking the magnitude square of the $q(x)$ as

$$I(x) = |q(x)|^2 = \left| \sum_i q_i(x) \right|^2. \quad (3.10)$$

Up until now, we showed the rigorous analysis of obtaining the elemental images of 3D impulsive image points using the kernel given by Eq. (2.10). However, we have to simplify Eq. (3.10) in order to interpret it easily. The general case presented here can be easily reduced to simpler versions by imposing certain assumptions on Eq. (3.10) related to the physical or simulation environments. First assumption is that the object depth is small compared to the calculation distance percentage-wise. In this case, the term $\frac{1}{\sqrt{j\lambda z}}$ in the Fresnel kernel can be assumed to be a constant as a consequence of a rather thin volume (restricting z within an interval with a small percentage change). So, we can leave this constant out of our analysis. The second assumption is made on the exclusion of the phase term $\exp\left(j\frac{2\pi}{\lambda}z\right)$. We have to be careful on this assumption since the phase term is more sensitive compared to the constant term $\frac{1}{\sqrt{j\lambda z}}$. However, this term may be still omitted if either one of two conditions are met: For the first case, suppose that all object points are restricted to have discrete depth values, z_i such that $\frac{2\pi}{\lambda}z_i$ is an integer multiple of 2π (the trivial case is when all object points lie on the same plane). This is a convenient and feasible restriction for computer generated

objects since the implied restriction on z_i 's result in a very small (equal to wavelength) step size compared to the physical size of a typical object. Even if the first condition is not satisfied, we may still drop the phase term from the kernel if the following condition is satisfied: Suppose that the object points are diffusing, that is, the complex amplitudes of the object points have random phase values. The assumption here is valid for most physical and synthetic objects. Dropping the phase term $\exp(j\frac{2\pi}{\lambda}z)$ is equivalent to a multiplication of the amplitude by $\exp(-j\frac{2\pi}{\lambda}z)$. But adding a constant to a random phase, which is modulo 2π radians, will not change the uniformly distributed random characteristics of the phase of the object complex amplitude. Such a simpler version of the Eq. (3.10) is used in [52] with the assumption that such conditions are met.

To simplify $I(x)$, we may further assume that the elemental images do not overlap and $P\left(\frac{x}{\lambda g}\right) * s(x)$ diminishes with respect to x such that each elemental image is imaged just behind the corresponding lenslet. We also assume that intensities of the responses of each source point can be superposed. All source points contribute to each and every image point on the image plane. However, we assume that only one source point corresponding to that image point has significant contribution at a particular location while the contribution from all other points is negligible. Under the specified assumptions, the magnitude square removes the phase terms $j\hbar_\beta\left(\sqrt{\frac{z_i}{g}}x\right)\exp[j\beta(x_i - rx_0)x]$ and $c(x)$ in $\Upsilon_i(x)$ $\left(\frac{z_i}{g}\right)s\left(-\frac{z_i}{g}x\right)$ remains as the only convolving term in Eq. (3.10). Also, the impulse train $x_g^2\sum_n\delta(x - nx_g)$ introduces a constant weight, x_g^2 , after the magnitude square operation. These impulses specify the locations of the imaged points. Thus, the impulse train indicated by $x_g^2\sum_n\delta(x - nx_g)$ and the impulse train in $\Upsilon_i(x)$ in Eq. (3.7) can be taken out of the magnitude square operation. The spot size of the imaged points are determined by convolution of the magnitude square of the function $\Gamma(x) = P_i\left(\frac{x}{\lambda g}\right) * s(x) * \sum_k a_k \mathcal{H}_{-\gamma_k}\left(\frac{x}{\lambda g}\right)$ and $\left(\frac{z_i}{g}\right)s\left(-\frac{z_i}{g}x\right)$. The Eq. (3.10), under above restrictions, is approximated as

$$I(x) \approx \sum_i \left\{ |\Gamma(x)|^2 * \left(\frac{z_i}{g}\right)s\left(-\frac{z_i}{g}x\right) * x_g^2 \sum_n \delta(x - nx_g) * \sum_r \delta\left[x - \left(1 + \frac{g}{z_i}\right)rx_0 + \frac{g}{z_i}x_i\right] \right\}. \quad (3.11)$$

which is given in [52].

To confirm this result we check the case where we use an analog lenslet array. If we have had an analog lenslet array, summation over k , the impulse train (indexed with n) due to sampling, the convolution with the pixel function $s(x)$ and the low pass filtering with $\left(\frac{z_i}{g}\right) s\left(-\frac{z_i}{g}x\right)$ would be dropped in Eq. (3.11). So, the result simplifies to the previous result given in [19], [25] which is given as

$$I(x) = \sum_i \left\{ \left| P_i \left(\frac{x}{\lambda g} \right) \right|^2 * \sum_r \delta \left[x - \left(1 + \frac{g}{z_i} \right) r x_0 + \frac{g}{z_i} x_i \right] \right\} \quad (3.12)$$

3.2 Display System

The reconstruction process is similar to the capture process where the distances g and d are interchanged, that is, the distance between the input, in this case a 2D plane consisting of an array of elemental images, and the lenslet array is measured as g while the distance between the reference plane on the reconstructed object/scene and the lenslet array is d . This is shown in Fig. 3.2. We can think that the light distribution $I(x)$ is input to this system. The input is only on a single plane consisting of a point cloud whereas the output consists of several planes. Each point in the point cloud will be reconstructed by carrying out a similar derivation as in the Sec. 3.1. The object is perceived with a pseudoscopic 3D reconstruction, that is, the points nearer to the pickup lenses will be far away from the reconstruction lenses forming a depth reversed object.

3.3 Optical Results

We constructed a simplified integral imaging system and conducted experiments with this system to confirm the computer simulations and theoretical analysis given in Sections 2.3 and 3.1, respectively. Since careful alignment of both parts (capture and display) are needed to match the elemental images captured by the CCD array to the LCD at the display setup to have a good reconstruction,

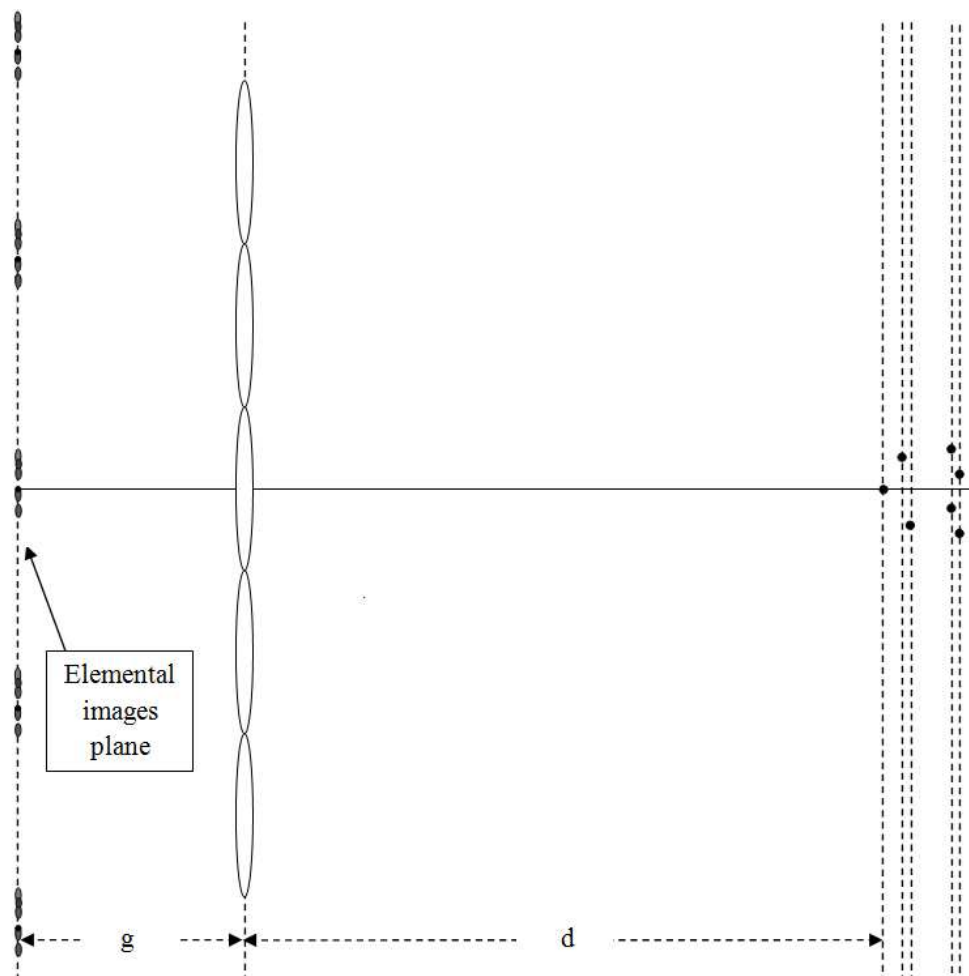


Figure 3.2: Display setup (Reprinted from “Integral imaging using phase-only LCoS spatial light modulators as Fresnel lenslet arrays,” Ali Özgür Yöntem and L. Onural, J. Opt. Soc. Am. A vol. 28, no. 11, pp.2359-2375, 2011. ©2011 OSA.)

we chose to construct our overall integral imaging system in one single stage as shown in Fig. 3.3. The display part immediately follows the capture part in this experimental setup. A picture of the setup is shown in Fig. 3.4. Furthermore, in the optical setup, we used a green 10W 4×5 LED array from Edipower, as the object instead of using a 3D object (Fig. 3.5), where we masked some LEDs to form the letter “C” shape. LEDs fit into a square of $7 \times 7mm^2$ area. One reason for us to choose an LED array is the undiffracted light at the output of the display. Since the SLMs have a limited diffraction efficiency, the observable reconstruction will have a quite limited power. When we used a passive 3D object illuminated by an external source in the experiments, we were able to observe elemental images on the diffuser at the elemental images plane. However, since there is an undiffracted light at the background together with the elemental images and since the intensities of the elemental images are lower compared to the undiffracted light, the visibility was poor. So, it was difficult to observe the reconstruction with these elemental images from a passive (illuminated) object at the display part of the proposed setup. When we used the LED array we still observe the undiffracted light at the background. But this time, intensities of the focused images are much brighter. The other reason to use a single color 2D LED array instead of a 3D object is the chromatic aberration introduced by the lenslets. Since, we calculated the lenslets for a certain wavelength, 532nm, an object illuminated with a white light causes elemental images to have chromatic aberration. There are some proposed methods to compensate for chromatic aberration [70]. However, in our experiments we chose to use a self-luminous object with a single color; our aim was to check the presented analysis. A single wavelength light source from a self-luminous LED array is easier to observe because the undiffracted light intensity will not dominate and there will be no chromatic aberrations. We used the lenslet array given in Fig. 2.2 on both SLMs in the capture and display part.

In the capture part, the object was imaged at the object plane with a projector lens, which is taken from an EPSON EMP TW-520 projector, to shrink the size of the real object and to collect and confine the light into a conical volume. The LED array is placed just behind the objective lens. The objective lens is adjusted such that the imaging distance from the objective to the object plane is $45mm$.

The image of the LEDs covers a $4 \times 4\text{mm}^2$ area on the image plane. The small sized real image of the object is then imaged by the lenslet array on SLM₁ to the diffuser plane where we observed the elemental images shown in Fig. 3.7. The distance from the object plane to the surface of SLM₁ is 188mm and the distance from the SLM surface to the diffuser is 68mm . In theory, the lenslets should have exactly 43.3mm focal length in free space propagation. However, in our system we use beam splitters in front of the SLMs, so, the actual focal length of the lenslets is shifted to approximately 55.3mm . So, we first try to find the elemental image plane (the plane where the elemental images seen the sharpest) and place the diffuser at this plane. And then, we measured the distance from the SLM₁ surface to the diffuser and placed the second SLM, accordingly. The elemental images fit into a rectangle of approximately $10\text{mm} \times 150\text{mm}$ area. One elemental image size is about $2\text{mm} \times 2\text{mm}$. The visibility of the elemental image set was good. As discussed in Sec. 3.1, we were also able to see the higher diffraction orders caused by the pixelated structure of the SLM. These orders are intermingled because of the difference between the elemental image separation period and the higher diffraction order separation period. Because of the finite SLM size, the intensities of the first diffraction orders are weaker than the central order, but stronger compared to the other higher orders. We masked higher diffraction orders even if they do not strongly affect the display part.

The display part starts from the diffuser. Since the elemental images were imaged directly on the diffuser, we did not need any other display device like in the conventional systems. So, we were able to observe the reconstructed image, which is shown in Fig. 3.8, by directly looking at the second lenslet array on SLM₂. We put another diffuser at the reconstruction distance. The distance of this diffuser to the elemental image plane is the same as the distance from the object plane to the elemental images plane. The reason for this second diffuser is to show that the reconstructed image is real. In fact, we were able to see the reconstruction well with bare eye without any diffuser. The quality of the reconstruction was quite high since we did not use a pixelated device (i.e. LCD) to display the elemental images. However, the resulting intensity is lowered by the beam splitters. Each beam splitter in the system lowers the input light intensity

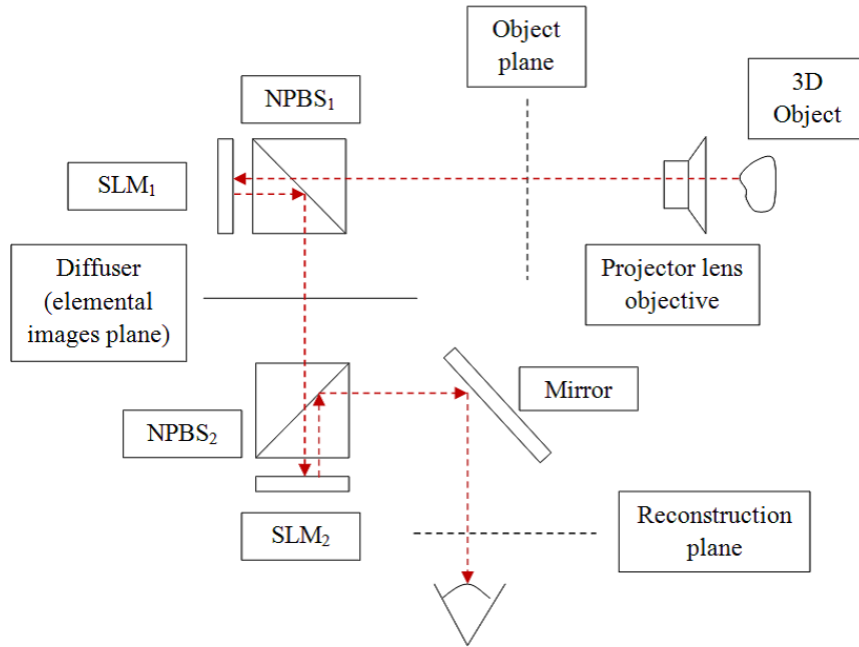


Figure 3.3: Experimental setup (Reprinted from “Integral imaging using phase-only LCoS spatial light modulators as Fresnel lenslet arrays,” Ali Özgür Yöntem and L. Onural, *J. Opt. Soc. Am. A* vol. 28, no. 11, pp.2359-2375, 2011. ©2011 OSA.)

by at least half and the light travels through each beam splitter twice. However, the light intensity at the output is acceptable. This experiment showed us that we can use phase-only SLMs with lenslet array phase pattern written on them to replace analog lenslet arrays in integral imaging systems. Such a system can easily be integrated into current digital projection systems.

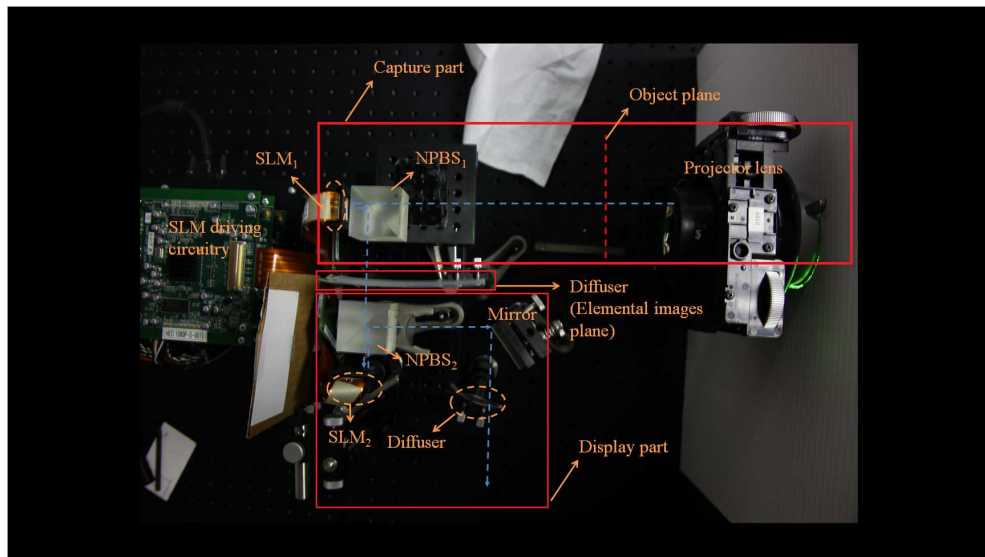


Figure 3.4: Top view of the optical setup: upper rectangle shows the capture part and lower square shows the display part. In between, a small rectangle shows the diffuser, which acts as a capture and display device, on the elemental images plane. The object is behind the white cardboard on the right before the projector lens. The cardboard prevents the light from the LED array to spread everywhere. The vertical dashed line after the projector lens shows the object plane. Dashed lines with the arrows shows the optical path. The small diffuser after the mirror is used to show that the image at the calculated reconstruction distance is real. (Reprinted from “Integral imaging using phase-only LCoS spatial light modulators as Fresnel lenslet arrays,” Ali Özgür Yöntem and L. Onural, J. Opt. Soc. Am. A vol. 28, no. 11, pp.2359-2375, 2011. ©2011 OSA.)

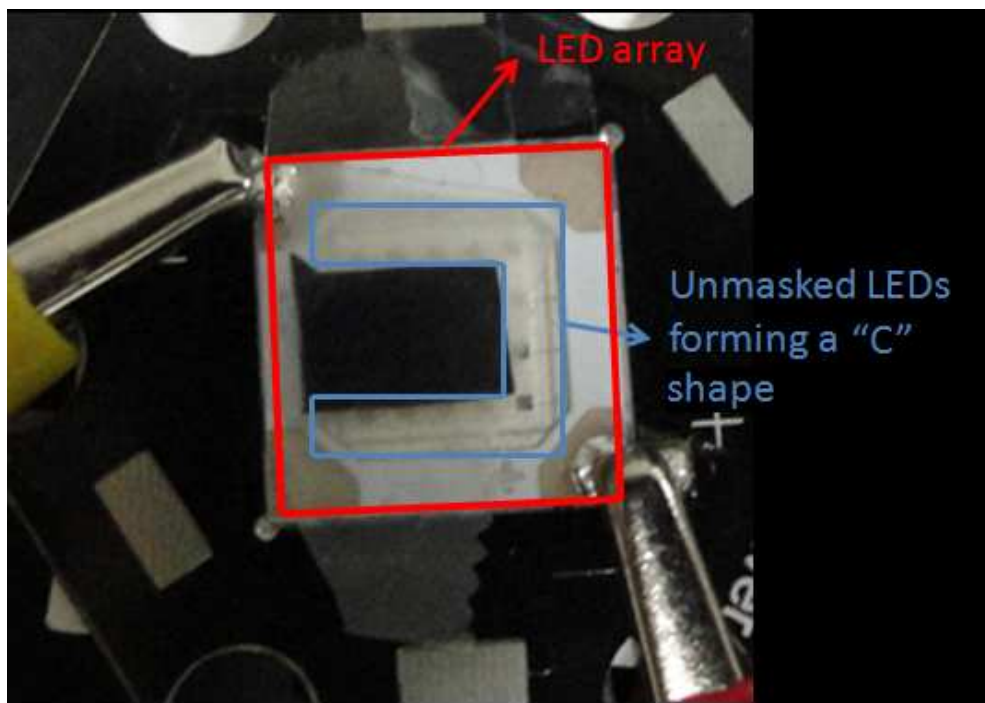


Figure 3.5: LED array that we used as the object. We put a black mask over the inner LEDs to form a (mirror image) “C” shaped object. (Reprinted from “Integral imaging using phase-only LCoS spatial light modulators as Fresnel lenslet arrays,” Ali Özgür Yöntem and L. Onural, J. Opt. Soc. Am. A vol. 28, no. 11, pp.2359-2375, 2011. ©2011 OSA.)



Figure 3.6: An image of the LED array on the object plane: the object is first imaged onto this plane by a projector lens to control both the depth and the size of the object. (Reprinted from “Integral imaging using phase-only LCoS spatial light modulators as Fresnel lenslet arrays,” Ali Özgür Yöntem and L. Onural, J. Opt. Soc. Am. A vol. 28, no. 11, pp.2359-2375, 2011. ©2011 OSA.)

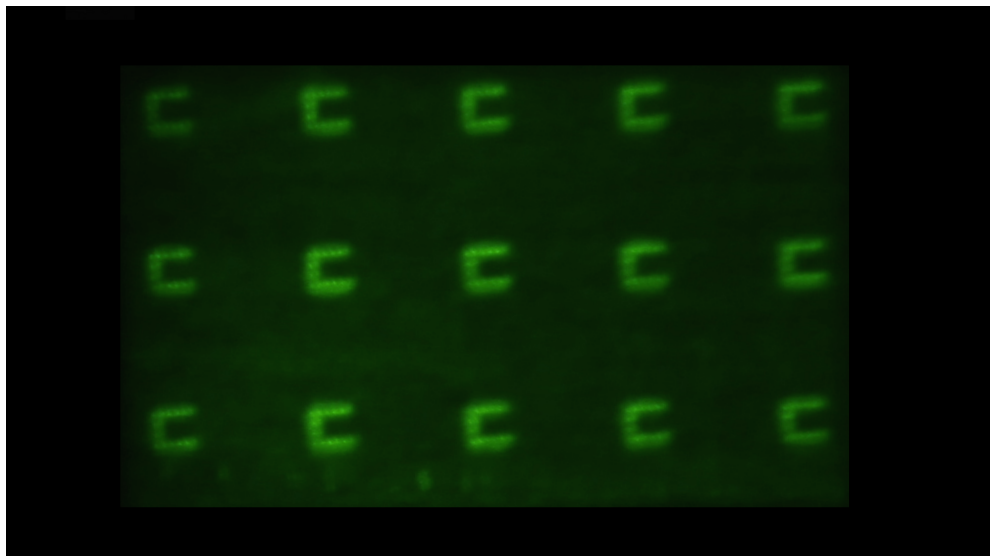


Figure 3.7: Optically captured elemental images (“Integral imaging using phase-only LCoS spatial light modulators as Fresnel lenslet arrays,” Ali Özgür Yöntem and L. Onural, J. Opt. Soc. Am. A vol. 28, no. 11, pp.2359-2375, 2011. ©2011 OSA. Reprinted with permission.)

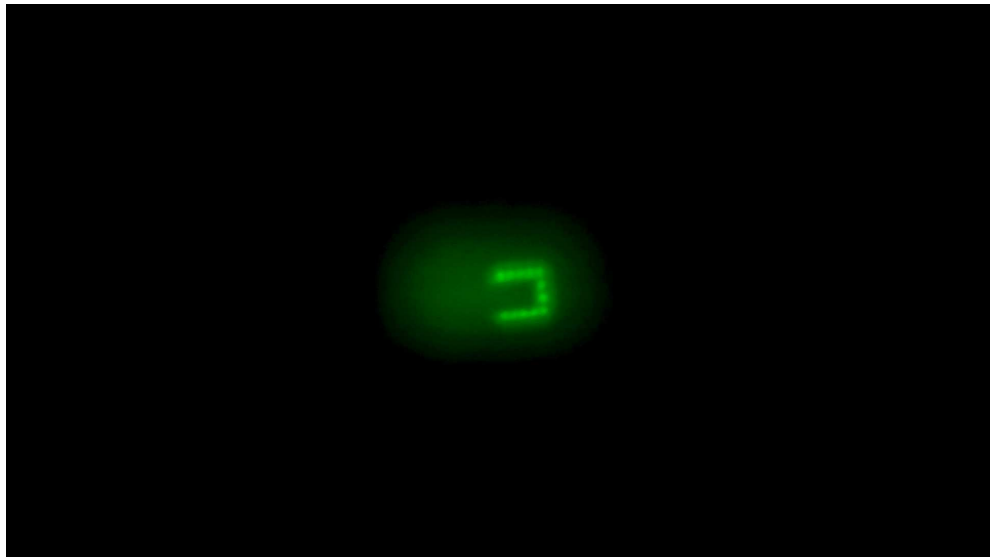


Figure 3.8: Optical reconstruction (Reprinted from “Integral imaging using phase-only LCoS spatial light modulators as Fresnel lenslet arrays,” Ali Özgür Yöntem and L. Onural, J. Opt. Soc. Am. A vol. 28, no. 11, pp.2359-2375, 2011. ©2011 OSA.)

Chapter 4

DISPLAY OF HOLOGRAPHIC RECORDING USING INTEGRAL IMAGING SYSTEM WITH DIGITAL LENS ARRAY

In this chapter, we present the method for elemental image generation from holographic data and an integral imaging optical setup to reconstruct 3D images from the computer generated elemental images. The holographic data may be acquired either by optical means or computed using digital techniques. We present our method in the following subsection. In the second subsection, we present the algorithm and in the third subsection we present four examples. In the first example, we obtain the elemental images of two letters at different depths. We first generated the diffraction patterns (computer generated holograms) of the letters. The complex diffraction pattern is then used as the input to our algorithm. The output of the algorithm gives the elemental image set of these letters at the imaging distance. For the second example, we obtain the elemental images of a 3D pyramid shaped object. In the third example, we obtain the set of elemental

images as the output from a digitally captured optical holographic data which is obtained using a diffraction tomography technique [57]; the object is an epithelium cell. The last example is another physical data obtained by conventional holographic methods. In the fourth subsection, we describe the optical setup which we used to reconstruct the 3D image from elemental images. And finally in the last subsection, we present the results of the optical reconstructions with the proposed optical setup. Thus, we show that the obtained elemental images can be used for optical reconstruction. Fortunately, at least on the display side, we do not have additional speckle noise problem since we use incoherent illumination for the optical reconstructions. The object sizes and display distances should match the optical setup requirements. Thus, the holographic data should be further processed if the object sizes and the distances do not match the display system. This processing is especially needed for optically captured holographic data.

4.1 The Method

Suppose we have digitally recorded holographic data (diffraction data) of a 3D object; a setup is shown in Fig. 4.1(a). Since, our aim is to display 3D image of a holographically recorded object/scene data by using an integral imaging technique, we need to convert the holographic data to elemental images. An in-line hologram of a 3D object is related to the diffraction field of that object [51]. This diffraction field can either be obtained digitally by calculating the propagation of light field scattered from the object or captured by optical means. In Fig. 4.1(a), a sketch of the diffraction pattern at $z = z_0$ of a cube is shown. In Fig. 4.1(b), a generic setup is demonstrated to holographically reconstruct the 3D image of the original object. In a digital holographic display system, diffraction field is sampled and written on a SLM. When the SLM is illuminated by a laser light source, an observer can perceive the 3D image [74]. For the integral imaging setup, to find the elemental images of a 3D object numerically, we used the algorithm shown by the block diagram depicted in Fig. 4.2(c) that represents the capture setup of a generic integral imaging system shown in Fig. 4.2(a). We

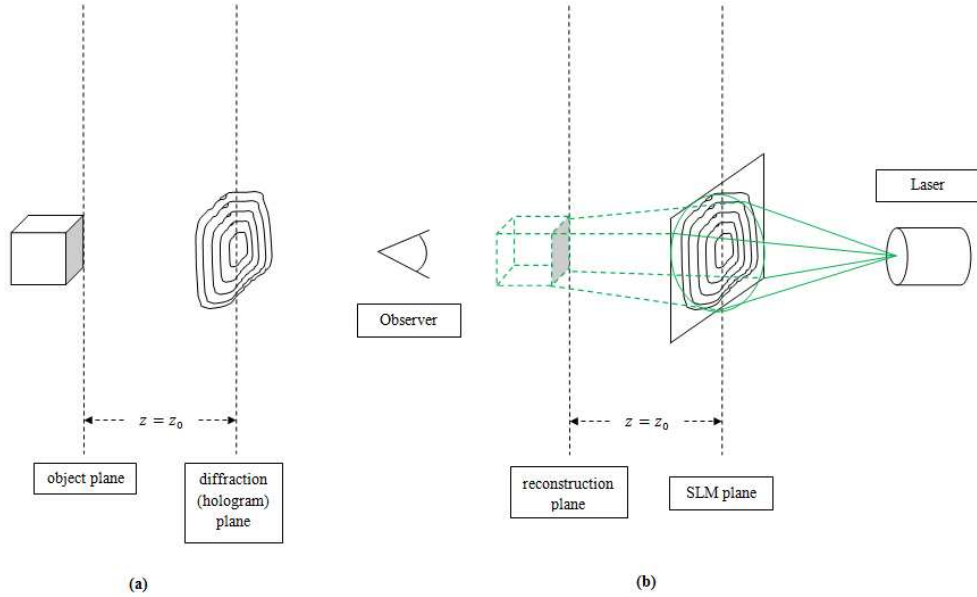


Figure 4.1: (a) A generic sketch of holographic recording. The diffraction pattern at $z = z_0$ is captured. (b) A generic sketch of 3D image reconstruction from the captured hologram. (Reprinted from “Integral imaging based 3D display of holographic data,” Ali Özgür Yöntem and L. Onural, *Opt. Express* vol. 20, no. 22, pp.24175-24195, 2012. ©2012 OSA.)

assume that the light field scattered from the object is available as diffraction data at the input. We obtained the elemental images by first calculating the Fresnel propagation of this data to the lenslet array plane, $z = d$, and then by multiplying this field by the lenslet array phase pattern, and finally, by computationally propagating the resulting field once more by a distance $z = g$, where $1/g = 1/f - 1/d$, f is the focal length of a single lenslet [52]. In Fig. 4.2(b), reconstruction of the 3D image at the display part of a generic integral imaging system is shown. The observer perceives a pseudoscopic 3D reconstruction due to the nature of direct pick-up method used in the capture part of the integral imaging system. It is easy to process the elemental images to set orthoscopic 3D images instead of pseudoscopic version [16]. To relate the diffraction data of a 3D object and the elemental images of the same 3D object, let us examine the setups in Fig. 4.1(a) and Fig. 4.2(a). Suppose that the wavelength is the same during recording and reconstruction. In the integral imaging system, the diffraction pattern just before the lenslet array is needed to find the elemental images as described above.

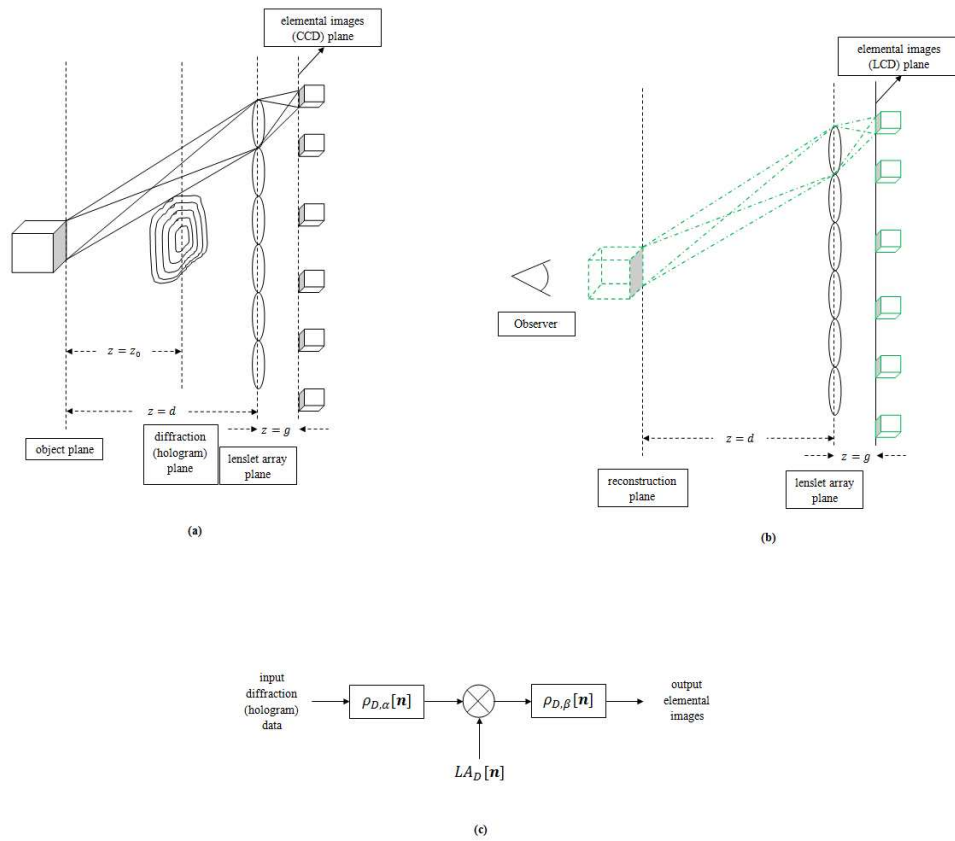


Figure 4.2: (a) A generic integral imaging data capture setup. The diffraction pattern in Fig.4.1 (a) is also depicted. For the same object with the same physical dimensions, the diffraction patterns in both systems are the same. (b) A generic Integral imaging display setup. The reconstruction is pseudoscopic due to employed direct pick-up method.(c) Designed model to calculate elemental images from diffraction (hologram) data. (Reprinted from “Integral imaging based 3D display of holographic data,” Ali Özgür Yöntem and L. Onural, Opt. Express vol. 20, no. 22, pp.24175-24195, 2012. ©2012 OSA.)

If we have the 2D diffraction field at a certain distance, we can find the 2D diffraction field of the same object at another distance by calculating the free space propagation. So, the field just before the lenslet array is related to the diffraction pattern at the distance $z = z_0$ and can be found by propagating this diffraction field by another distance $z = d - z_0$. However, we might have an input diffraction pattern obtained from a holographic setup with a different wavelength than the one used in the integral imaging display system. In that case we need to pre-process the input data.

The impulse response of the continuous Fresnel kernel is given by Eq. (2.3). The scalar wave propagation can be modeled as a linear shift invariant system with the impulse response given by Eq. (2.4). Naturally, discretizations are needed for computer simulations. For this reason we model the analog system given in Fig. 4.2(a) as a discrete system given in Fig. 4.2(c). Here the two blocks represent discrete linear shift invariant systems with impulse responses $\tilde{h}_{D,\alpha}[\mathbf{n}]$ and $\tilde{h}_{D,\beta}[\mathbf{n}]$. So, we can use convolution to compute the response of the system to a discrete input.

In the model, we first convolve the input data by the discrete kernel $\tilde{h}_{D,\alpha}[\mathbf{n}]$ where $\alpha = \frac{\pi}{\lambda d}$ and then multiply by the lenslet array phase distribution $LA_D[\mathbf{n}]$ and we finally obtain the elemental images by convolving the result by $\tilde{h}_{D,\beta}[\mathbf{n}]$ where $\beta = \frac{\pi}{\lambda g}$. Note that we omitted the constants in the discrete versions of the kernel in order not to clutter the computations. This is also discussed in Sec. 3.1. The discretization issues related to diffraction are discussed in [51].

It will be helpful to have a prior information about the physical parameters (wavelength, capture distance, capture device pixel period) of the holographic recording process. If there is a mismatch between the recording parameters and the display parameters, we should process the hologram to match the parameters of these two steps. In case of a mismatch between the physical parameters of the holographic recording step and our display, the matching process is equivalent to equating the corresponding discrete Fresnel kernels. To find the relation between the kernels, let us assume that $\tilde{h}_{D,\alpha_1}[\mathbf{n}]$ represents the propagation associated with the holographic input setup parameters and the kernel $\tilde{h}_{D,\alpha_2}[\mathbf{n}]$ represents

the propagation with the integral imaging setup parameters. If we equate the quadratic phases in $\hbar_{D,\alpha_1}[\mathbf{n}]$ and $\hbar_{D,\alpha_2}[\mathbf{n}]$, we can find the relation that matches the physical parameters. Let $\exp[j\alpha_1 X_1^2 \mathbf{n}^T \mathbf{n}]$ be the quadratic phase in the Fresnel kernel representing the 2D diffraction field of the holographic setup where $\alpha_1 = \frac{\pi}{(\lambda_1 z_1)}$, λ_1 is the wavelength, z_1 is the propagation distance, X_1 is the sampling period of the field in both directions. $\mathbf{n} = [n_1 \ n_2]^T$ where n_1, n_2 are integers. Let $\exp[j\alpha_2 X_2^2 \mathbf{n}^T \mathbf{n}]$ be the quadratic phase in the Fresnel kernel representing the 2D diffraction field of the integral imaging setup where $\alpha_2 = \frac{\pi}{(\lambda_2 z_2)}$. If we equate the parameters of these functions $\forall n$, we get, $\alpha_1 X_1^2 = \alpha_2 X_2^2$ thus $\frac{\pi}{(\lambda_1 z_1)} X_1^2 = \frac{\pi}{(\lambda_2 z_2)} X_2^2$. So, we can find that $z_2 = z_1 \cdot \frac{\lambda_1}{\lambda_2} \cdot \frac{X_2^2}{X_1^2}$ [73].

During the process, we wish to first back propagate the holographic data to a location which we call the “origin”. The origin is defined as the effective depth of the nearest point of the object to the lenslet array. So, back-propagating the input data by z_2 is equivalent to placing the 3D object effectively at the origin as in Fig. 4.2(a) [73]. This way we can obtain a focused elemental images set at the output. If we do not have the prior information about the physical capture setup parameters, we can still find the object field at the origin. This time, first we find a focused image from the hologram by making propagations back and forth by using our setup’s parameters. This is like a camera autofocus. When we obtain a focused image we can determine the origin. And then we can use the complex object field at the origin as the input data.

4.2 The Algorithm

The algorithm is given by the flowchart shown in Fig. 4.3. The input of the algorithm is diffraction data. Additional preprocessing steps may be needed depending on the nature of input data and the desired quality of the output display. For example, if the input is not from an object with a diffusing surface, we may need to multiply the associated field with a random phase to improve the visibility at the output. Also, for the cases where the recording physical parameters do not match with the display system parameters and where the object size is

small compared to the display size, we may need to pre-process the data. The procedures for such cases will be discussed in detail later in this section. However, here we should mention that for all these cases, we first want to find the complex object field at the origin and then apply the specified processes. Actually, this step is not a necessity. On the contrary, we can generate the elemental images with the given diffraction pattern directly. To cover all cases by a single uniform step, we first back-propagate all input to the origin, and then apply the fixed process as described in Fig.2(c). This will then directly give the elemental images regardless of the properties of the original data.

Again, we use the DFT method to compute the convolution to find outputs of the discrete systems as in Sec. 2.3. This time, in our examples, the signal window sizes are chosen smaller than 1920×1920 while the computation window sizes are chosen as 3840×3840 . We choose the range for n_1, n_2, k_1 and k_2 as $[-1920, 1919]$ in our examples. Again $w_t[\mathbf{n}]$ is the computational window and $t[\mathbf{n}]$ is centered inside $w_t[\mathbf{n}]$.

On the lenslet array plane, we generate the lenslet array complex phase pattern given as in [52]. A single lenslet of the array is given by Eq. (2.7), which is obtained by discretizing Eq. (2.6), by setting the parameter $\gamma = \frac{\pi}{\lambda f}$. The discrete variables, n_1, n_2 , are in the interval $[-M/2, M/2 - 1]$. Again we chose the focal length as $f = M \frac{\lambda^2}{\lambda}$ to cover the entire normalized frequency range in the interval $[-\pi, \pi)$ radians where M is the length of one side of a lenslet. A 2D array of lenslets, $LA_D[\mathbf{n}]$, is generated by replicating $l_{D,-\gamma}[\mathbf{n}]$ in both directions in a rectangular fashion. $LA_D[\mathbf{n}]$ is centered within the computation window $w_{LA}[\mathbf{n}]$. Also, the lenslet array is large enough to image most of the light scattered from the object. $w_{LA}[\mathbf{n}]$ is multiplied by the diffraction pattern of the object, $t_d[\mathbf{n}]$, which is given by

$$t_d[\mathbf{n}] = IDFT \left\{ DFT \{ w_t[\mathbf{n}] \} g_{D,\theta}[\mathbf{k}] \right\} \quad (4.1)$$

where $\theta = \pi \lambda d$.

Focal length of the lenslets is chosen such that it satisfies the imaging equation $1/f = 1/g + 1/d$ and proper magnification ratios are obtained at the imaging plane. To give numerical examples, we chose $f = 10.8mm$ and $d = 7f$. Finally,

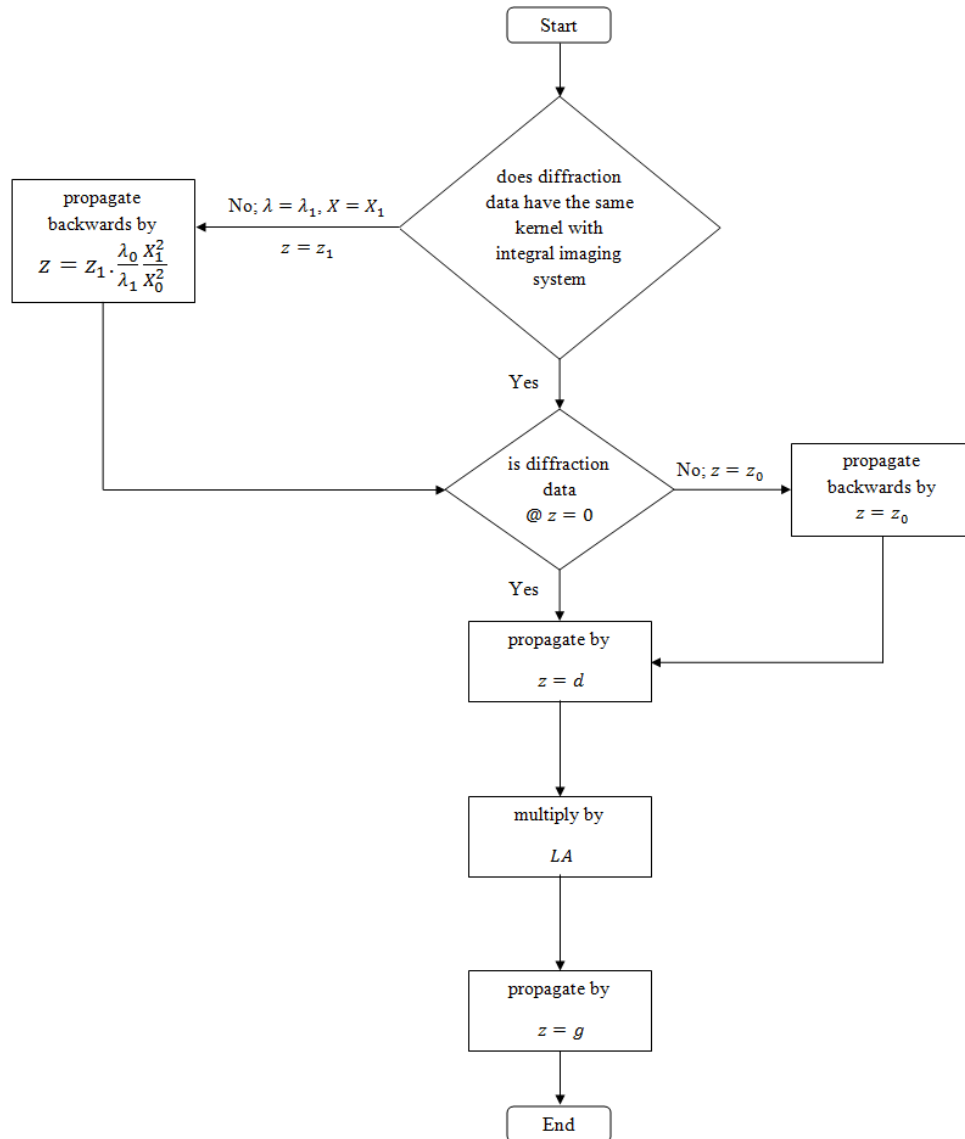


Figure 4.3: The algorithm to generate elemental images from a diffraction pattern. (Reprinted from “Integral imaging based 3D display of holographic data,” Ali Özgür Yöntem and L. Onural, Opt. Express vol. 20, no. 22, pp.24175-24195, 2012. ©2012 OSA.)

we calculate the diffraction pattern due to the resulting complex field of the multiplication $w_{LA}[\mathbf{n}]t_d[\mathbf{n}]$ at the imaging depth, g . The resultant complex diffraction pattern is given by

$$p[\mathbf{n}] = ID\hat{F}T \left\{ D\hat{F}T \left\{ w_{LA}[\mathbf{n}] t_d[\mathbf{n}] \right\} g_{D,\sigma}[\mathbf{k}] \right\} \quad (4.2)$$

where $\sigma = \pi\lambda g$. Taking the square magnitude of this pattern simulates the discrete intensity recording,

$$I[\mathbf{n}] = |p[\mathbf{n}]|^2. \quad (4.3)$$

As a result, we obtain computer generated elemental images of the 3D object.

4.3 The Examples

Now we will proceed with the examples of three different input diffraction patterns, as a proof of the concept; we chose three examples. In the reconstructions, we demonstrate the depth of focus, viewing angle and parallax of our display, qualitatively. The first example is a set of two planar letters; the letters are at different depths. Such an example is extensively used in the literature [45, 46, 48]. This example helps us to understand whether we are able to distinguish different depths in the reconstructions. Also, it gives an idea about the depth of focus of the lenslets. Our second example is an extension of the first one. We sliced down a pyramid object to create several planar objects. This time our aim is to show the parallax that can be obtained using our display. Since, we have a depth variation in the object, it is easier to observe the parallax effect. The last example presents the most important aspect of our method. We used a digitally obtained optical diffraction tomography data as the input of our method. We can generate elemental images even from such physical data.

In the first example, we have two different digital letters at two different depths. One letter is located at the origin, and the other one is located at $z = -5f$ where $f = 10.8mm$. These letters are separated along the x -axis by $2.6mm$. The amplitude of the object points on the letters are taken as 1 and the other points outside the letters are 0. Let the letter located at distance $z = -5f$

is represented by the computation window $w_{t_1}[\mathbf{n}]$ and the other is represented by $w_{t_2}[\mathbf{n}]$. So, we have two slices in the space. To find $w_t[\mathbf{n}]$ we perform the following computation:

$$w_t[\mathbf{n}] = ID\hat{F}T \left\{ D\hat{F}T \{ w_{t_1}[\mathbf{n}] R_1[\mathbf{n}] \} g_{D,\chi}[\mathbf{k}] \right\} + \{ w_{t_2}[\mathbf{n}] R_2[\mathbf{n}] \} \quad (4.4)$$

where $\chi = \pi\lambda(5f)$, $R_i[\mathbf{n}]$, $i \in \{1, 2\}$, is a random matrix with entries $R_i[\mathbf{n}] = [r_{n_1 n_2}]$ where $r_{n_1 n_2} = \exp(-j2\pi\mathcal{X})$ and where \mathcal{X} is a random variable uniformly distributed in $[0, 1]$. Thus, the window $w_{t_1}[\mathbf{n}]$ is first multiplied by a random phase $R_1[\mathbf{n}]$ and then propagated by an effective distance of $5f$. The result is added to $w_{t_2}[\mathbf{n}]$ which is also multiplied by another random phase factor. The second slice is not propagated since it is already located at the origin. The assumption is that, the multiple diffraction effects from each slice of the object are negligible. Thus, each slice is assumed to contribute to the diffraction field independently of others. This is because, the multiplication with the random phase simulates diffusing surfaces, and thus, ensures that the light traveling in the space well scatters almost everywhere. Each object slice will block a negligible fraction of the scattered light from previous object slices. Therefore, the light scattered from each object slice will reach the lenslet array plane and imaged on the recording plane. Thus, the object become visible at the reconstructions with minimal degradation due to obstruction.

To note that, the object at $z = -5f$ distance will be $5f$ in front the object at the origin in the reconstruction. So, the object at the origin will be reconstructed at $d = 7f$, which is the distance we chose while generating the elemental images, and the other object will be observed at $12f$. The generated elemental images set is given in Fig. 4.4. The second example is a pyramid object. This time we have several slices of a pyramid object; a sketch is shown in Fig. 4.5. Only six slices are shown in Fig. 4.5 for clarity. However, we chose to simulate with nine slices. Only the base part of the pyramid is a full frame. And only the tip of the pyramid is a single square patch. At each other slice, we have square patches located at the corners on the edges. When looking from the center, each slice containing square patches can be seen clearly, that is, any patch do not obscure the others including the base frame and the tip. This is a coarse quantization of a wire-frame pyramid structure. To make a reconstruction where the tip is at the



Figure 4.4: Computed and recorded elemental images of two letters at different depths and positions. (We enhanced the brightness of the figure for visual purposes. This is achieved by stretching the contrast. The figure is also used on the LCD display of the integral imaging setup as is. Similar enhancement procedure is used in Figs. 4.6, 4.8 and 4.17-4.20. In Figs. 4.17-4.20, we enhanced only the computer simulation results.) (Reprinted from “Integral imaging based 3D display of holographic data,” Ali Özgür Yöntem and L. Onural, *Opt. Express* vol. 20, no. 22, pp.24175-24195, 2012. ©2012 OSA.)

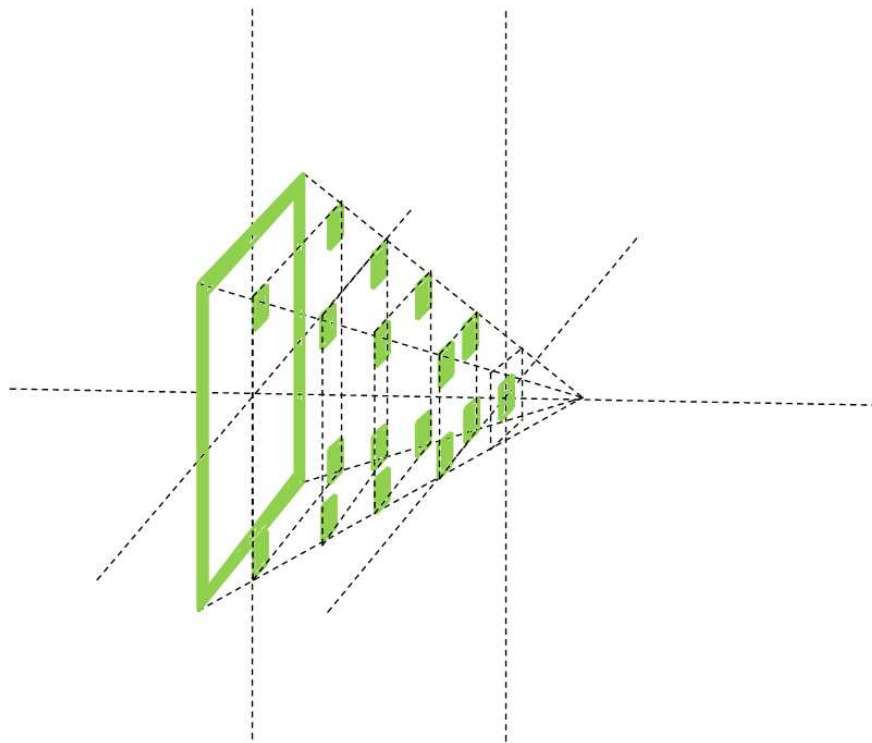


Figure 4.5: A sketch of the pyramid object. A square pyramid is sampled (sliced) over the z -axis. Base part is a square frame while the edges and the tip of the pyramid are small square patches. For display purposes we showed six slices of the object whereas in the simulations we used nine slices. (Reprinted from “Integral imaging based 3D display of holographic data,” Ali Özgür Yöntem and L. Onural, *Opt. Express* vol. 20, no. 22, pp.24175-24195, 2012. ©2012 OSA.)

front and the base frame is at the back, the base frame ($w_{t_0}[\mathbf{n}]$) is located at the origin and tip ($w_{t_8}[\mathbf{n}]$) is located at $z = 24mm$. We chose such a size because, we had a similar size physical wire-frame pyramid, which is also used in [75], to compare the optical reconstructions. The base frame of this physical pyramid is a square with an edge size of $8mm$. In the simulations, the pixel size of this edge is 960 pixels. The width of the patches and the wire-frame is 60 pixels. $w_t[\mathbf{n}]$ is computed as,

$$w_t[\mathbf{n}] = \sum_{i=0}^8 IDFT \left\{ DFT \left\{ w_{t_i}[\mathbf{n}] R_i[\mathbf{n}] \right\} g_{D,\chi}[\mathbf{k}] \right\} \quad (4.5)$$

where $\chi = \pi\lambda(i\Delta)$ and $\Delta = 24mm/8 = 3mm$. Note that $g_{D,\chi}[\mathbf{k}] = 1$ when $\chi = 0$. Fig.4.6 shows the elemental images of the pyramid object.

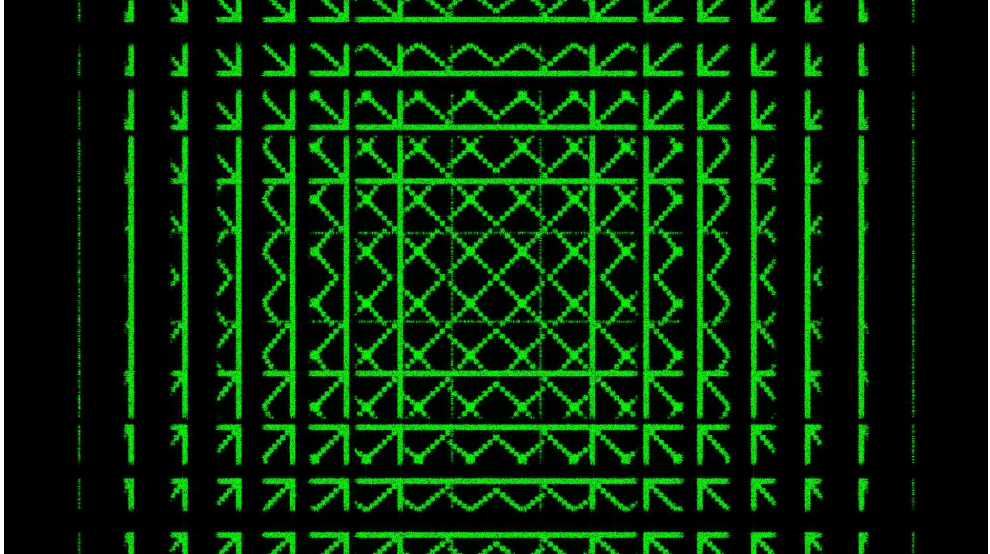


Figure 4.6: Computed and recorded elemental images of the pyramid object. (We enhanced the brightness of the figure for visual purposes.) (Reprinted from “Integral imaging based 3D display of holographic data,” Ali Özgür Yöntem and L. Onural, Opt. Express vol. 20, no. 22, pp.24175-24195, 2012. ©2012 OSA.)

The third example is a physically captured diffraction data obtained by a diffraction tomography technique [57]. The object is an epithelium cell, which is mostly a transparent (phase) object. The object has a small depth compared to the recording distance. So, it is harder to see the 3D volume and perceive the parallax for this object. Moreover, a coherent illumination is used while obtaining

the diffraction pattern. Furthermore, the size of the data is small pixel-wise, so, we zoomed the input data to perceive a larger object. All of these issues are handled as follows: To zoom the object, we interpolated the 2D signal. To do that, we upsampled the original diffraction data, $t_{captured}[\mathbf{n}]$, by a factor of two in both directions ($K = 2$) and then low pass filtered the result and obtained $t_{interpolated}[\mathbf{n}]$ as,

$$t_{upsampled}[\mathbf{n}] = \begin{cases} t_{captured} \left[\frac{n_1}{K}, \frac{n_2}{K} \right], & \frac{n_1}{K} \text{ and } \frac{n_2}{K} \text{ are integers} \\ 0, & \text{else} \end{cases}$$

$$t_{interpolated}[\mathbf{n}] = t_{upsampled}[\mathbf{n}] * LPF_{\frac{\pi}{K}}[\mathbf{n}]$$

where $LPF_{\frac{\pi}{K}}$ is the low pass filter with pass band $\frac{\pi}{K}$ convolving $t_{upsampled}[\mathbf{n}]$. This method does not degrade the diffraction pattern. The result can be seen in Fig. 4.7. The diffraction data was captured at a certain distance, $z = z_1$. First, we will propagate this data backwards to the origin as it is shown in the flowchart in Fig. 4.3. However, since we upsampled the data, the parameter η of the kernel changes and the required propagation distance become $z = K^2 z_1 \frac{\lambda_1 X_1^2}{\lambda X^2}$. The new physical distance parameter is affected by square of the upsampling factor since other physical parameters related (wavelength, pixel period) to η are kept constant. So, back propagation from the modified data will result in a distortion on the depth of the object. For example, if the original object had a spherical shape and we reconstruct the modified diffraction data, then the reconstructed object would have an ellipsoidal shape. So, the object field obtained by back propagation will now have a distorted depth values. Thus, the pre-processed signal (complex field) becomes,

$$t_{object}[\mathbf{n}] = IDFT \left\{ DFT \{ t_{interpolated}[\mathbf{n}] \} g_{D,\chi}[\mathbf{k}] \right\}, \quad (4.6)$$

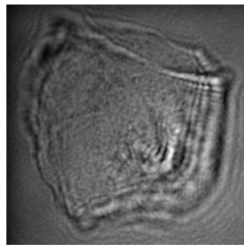
where $\chi = \pi \lambda \left(K^2 z_1 \frac{\lambda_1 X_1^2}{\lambda X^2} \right)$. We now, insert this signal into the center of the computation window $w_t[\mathbf{n}]$, thus, we have the diffraction field at the origin. At this point, the complex diffraction data contains the three-dimensional information of the object.

In order to improve the visibility of the object, and also to use the full viewing angle of the display device, we choose to multiply the complex diffraction data with a random phase. A diffusive surface is much more visible than a bright one.

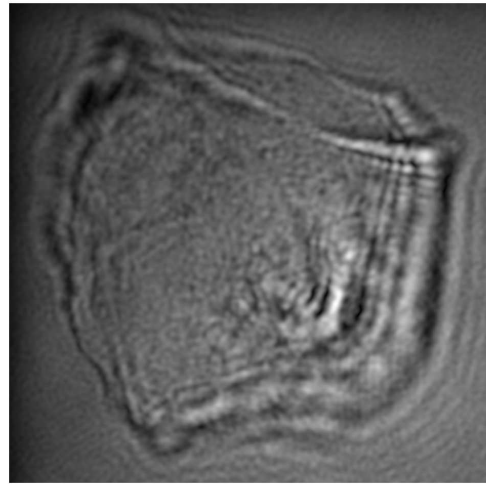
Moreover, the light will reach to and be imaged by most of the lenslets, increasing the viewing angle. Here, one should be careful while doing this operation since it might destroy the three-dimensional information. This can be visualized as putting a diffusive glass in front of an object. The parts closer to the glass can be seen well while the far away points will be obscure. Depending on the depth of the object, only certain parts of the object are seen in focus if the magnitude of this field is imaged. For this example, most of the object is in focus at the origin, and fortunately, this operation improves the performance of our method. For those objects that have a rather large depth, this method may not work. Even if this step is skipped, the method would still work. However, this time, only those lenslets closer to the center of the lenslet array will image the 3D object. The ones at the periphery will not generate any image since the light from the object will not reach them. This will decrease the viewing angle of the reconstructed 3D image. So, multiplication by a random phase helps us to use the maximum viewing angle. We multiply $w_t[\mathbf{n}]$ with a random phase $R[\mathbf{n}]$. For this last example the elemental images are shown in Fig. 4.8. Note that, the elemental images obtained for the epithelium cell is filtered by a simple high pass filter to sharpen the edges and enhance the details of the object. We filtered the signal by a half band high pass filter. This improved the reconstruction quality, which is determined by subjective assessments. All of the examples need slightly different preprocessing. However, once we obtained $w_t[\mathbf{n}]$, the rest of the algorithm is the same for all cases.

For the last example, we followed the similar steps as in the previous one. However, this time, it is not a diffraction tomography data. The hologram is from a toy object shown in Fig. 4.9.

This time the object data size is larger than our display device pixel size. So, we did not interpolated this data and directly used it. However, we preprocessed the hologram data in order to remove the DC term which is present do to the reference beam used in the capturing process. We filtered the hologram data with a narrow band low pass filter to eliminate this and obtained $t_{DC_{removed}}[\mathbf{n}]$. It is necessary to improve the visual quality of the reconstruction. The reconstruction of the hologram data is given in Fig. 4.10.



(a)



(b)

Figure 4.7: (a) The amplitude picture of the diffraction pattern of the epithelium cell. (b) The upsampled (interpolated and low pass filtered) version of (a). (The hologram data, from which this reconstruction was obtained, was courtesy of cole Polytechnique Fdrale de Lausanne within the Real 3D project.) (Reprinted from “Integral imaging based 3D display of holographic data,” Ali Özgür Yöntem and L. Onural, *Opt. Express* vol. 20, no. 22, pp.24175-24195, 2012. ©2012 OSA.)

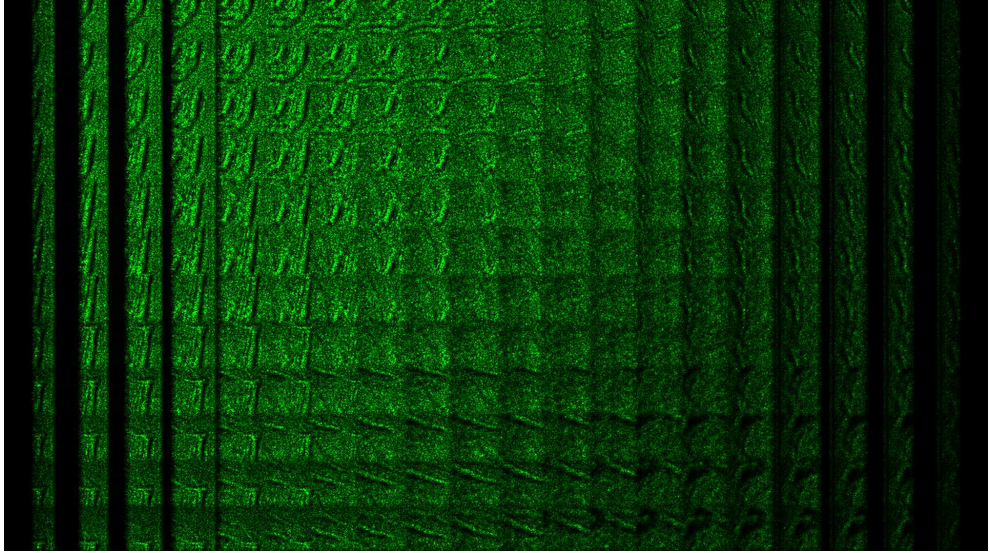


Figure 4.8: Computed and recorded elemental images of the epithelium cell. (We enhanced the brightness of the figure for visual purposes.) (The hologram data, from which this reconstruction was obtained, was courtesy of cole Polytechnique Fdrale de Lausanne within the Real 3D project.) (Reprinted from “Integral imaging based 3D display of holographic data,” Ali Özgür Yöntem and L. Onural, *Opt. Express* vol. 20, no. 22, pp.24175-24195, 2012. ©2012 OSA.)

As it can be seen in the Fig. 4.10, there is noise present in the reconstruction. This is due to the coherent light source (laser) used during the recording. The input consists of diffusing surfaces. The complex field, $t_{object}[\mathbf{n}]$, that we insert at the center of the computation window, $w_t[\mathbf{n}]$, is

$$t_{object}[\mathbf{n}] = ID\hat{F}T \left\{ D\hat{F}T \{ t_{DC_{removed}}[\mathbf{n}] \} g_{D,\chi}[\mathbf{k}] \right\} , \quad (4.7)$$

where $\chi = \pi\lambda \left(z_1 \frac{X^2}{X_1^2} \right)$ and $z = z_1 \frac{X^2}{X_1^2}$ is the recording distance. This time the wavelength is the same in both capture and display systems. With these parameters we obtain the elemental images shown in Fig. 4.11.

We also performed reconstruction simulations and compared them with the optical reconstructions. To simulate the reconstructions, we computed our algorithm in the reverse order. Therefore, this time the input of the algorithm is the intensity distribution of the elemental images, $I[\mathbf{n}]$, at a single plane. We first multiplied the elemental images with a random phase $R[\mathbf{n}]$ and then propagate the result to a distance $z = g$, where the lenslet array is located. The complex



Figure 4.9: Toy object (The hologram data, from which this reconstruction was obtained, was courtesy of National University of Ireland, Maynooth within the Real 3D project.)

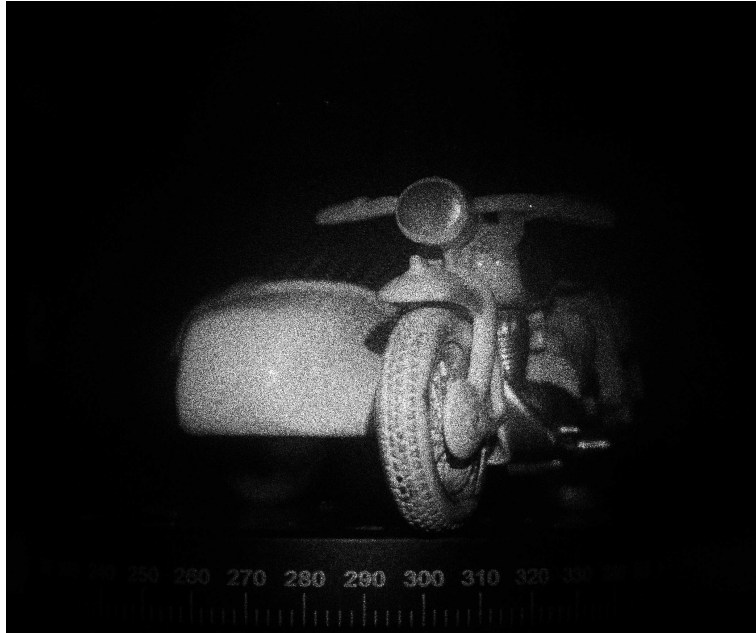


Figure 4.10: Reconstructed hologram of the toy object. (The hologram data, from which this reconstruction was obtained, was courtesy of National University of Ireland, Maynooth within the Real 3D project.)

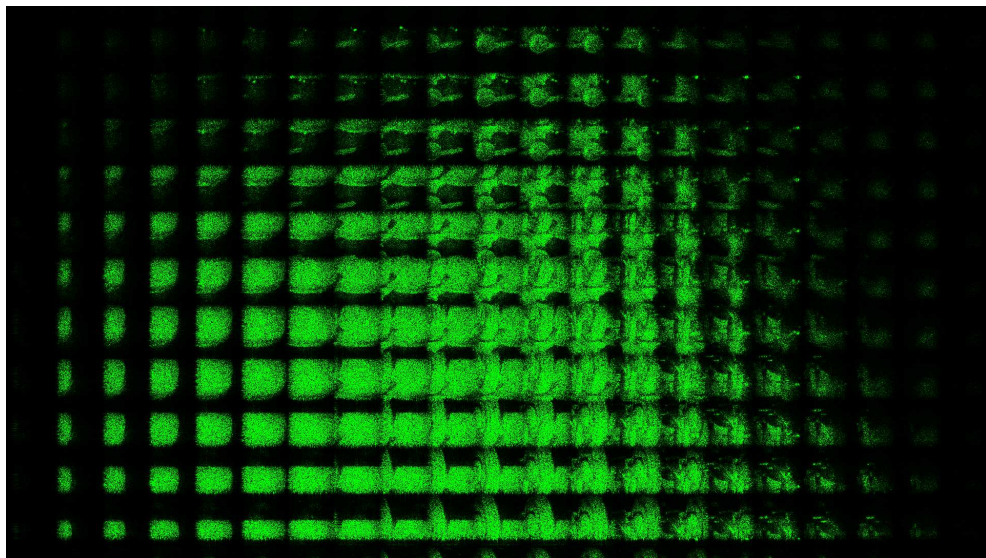


Figure 4.11: Elemental images of the toy object. (The hologram data, from which this reconstruction was obtained, was courtesy of National University of Ireland, Maynooth within the Real 3D project.)

field just before the lenslet arrays is given by

$$t_d[\mathbf{n}] = IDFT \left\{ DFT \{ I[\mathbf{n}] R[\mathbf{n}] \} g_{D,\sigma}[\mathbf{k}] \right\} . \quad (4.8)$$

We multiply this field with the lenslet array pattern, $w_{LA}[\mathbf{n}]$, as in the previous case. Finally, we propagate the field just after the lenslet array to a distance $z = d + \Delta d$, where d is the closest distance from the points on the object to the lenslet array and Δd is the additional distance to focus on the far away object points. We can focus at a certain plane by selecting this distance. The intensity distribution on the focused plane is given by

$$r[\mathbf{n}] = \left| IDFT \left\{ DFT \{ w_{LA}[\mathbf{n}] t_d[\mathbf{n}] \} g_{D,\chi}[\mathbf{k}] \right\} \right|^2 \quad (4.9)$$

where $\chi = \pi\lambda(d + \Delta d)$. The simulation results for the reconstructions are given in Section 4.5.

4.4 The Optical Setup

The optical setup is depicted in Fig. 4.12. We display the elemental images on a Samsung T240 monitor. The resolution of the monitor is 1920×1200 pixels. Our elemental image set size is 1920×1080 pixels. So, we fit the image by leaving 60 pixels from top and bottom blank. The pixel size of the monitor is $0.27mm$ and the dimensions of the active area that we used was $518mm \times 292mm$. The lenslet array is written on a Holoeye HEO 1080P phase-only LCoS SLM, which is a high definition 1920×1080 pixels reflective type SLM. We write 20×12 lenslets on the SLM. Each lenslet has a size of 90×90 pixels with a focal length $f = 10.8mm$. Pixel size of the SLM is $8\mu m$, thus each lenslet size is $0.72mm \times 0.72mm$. With that many lenslets we can only fit a lenslet array with full size lenslets to an active area of 1800×1080 pixels on the SLM. The unused parts (60 pixel each) are left blank equally on the left and right side of the SLM. Thus, the active area size for the lenslet array was $14.4mm \times 8.64mm$. The lenslet array is shown in Fig. 4.13.

Our setup is a typical integral imaging display setup. However, due to the size difference between the lenslet array and the LCD screen, we need to scale the

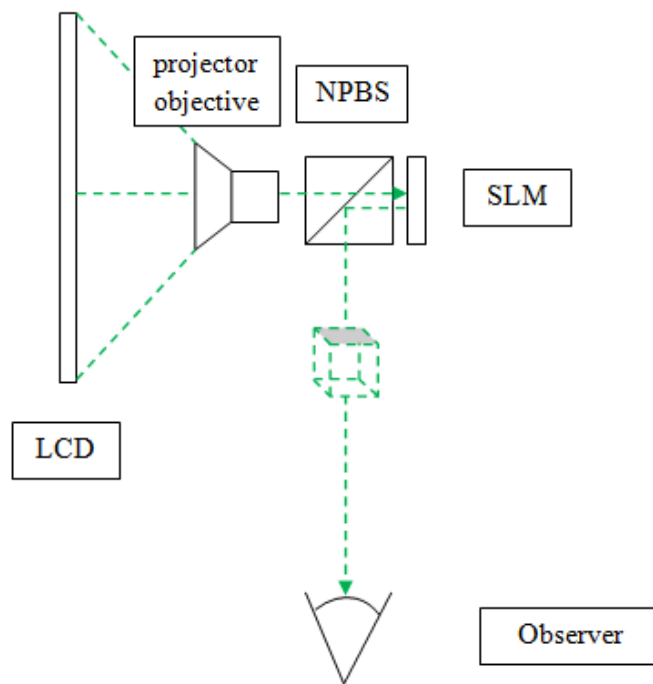


Figure 4.12: The optical setup (Reprinted from “Integral imaging based 3D display of holographic data,” Ali Özgür Yöntem and L. Onural, Opt. Express vol. 20, no. 22, pp.24175-24195, 2012. ©2012 OSA.)

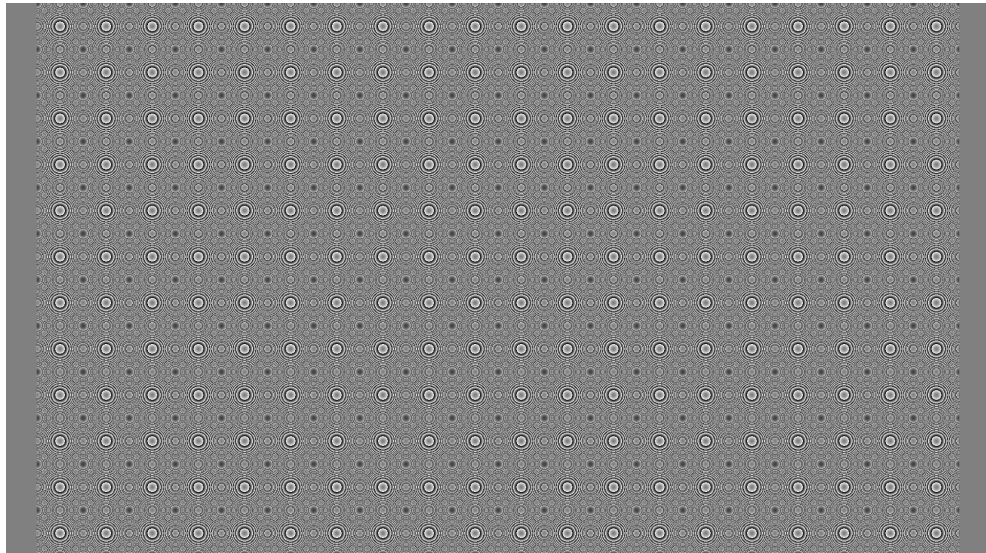


Figure 4.13: A Fresnel lenslet array pattern with 12×20 lenslets. Each lenslet has a focal length of 10.8mm . We excluded the lenslet on either side of the array since they would be cropped if we have included them. Instead we left 60 pixels blank from either side of the array that is written on the 1920×1080 pixels phase only LCoS SLM. (Reprinted from “Integral imaging based 3D display of holographic data,” Ali Özgür Yöntem and L. Onural, *Opt. Express* vol. 20, no. 22, pp.24175-24195, 2012. ©2012 OSA.)

elemental images on the LCD screen by the help of a projector objective. For this reason, we used a projector objective which is disassembled from a Epson EMP-TW520 projector. Since the SLM is reflective type, we put a non-polarizing beam splitter (NPBS) to illuminate and observe the reconstructed image. However, the NPBS changes the focal point of the lenslets [52]. Thus, for fine tuning, we tried to find a focused reconstruction while changing the position of the projector objective. The reconstructions are observed at the expected distances. The entire system, its close-up view and the view from the viewing zone perspective are shown in Fig. 4.14, Fig. 4.15 and Fig. 4.16, respectively.

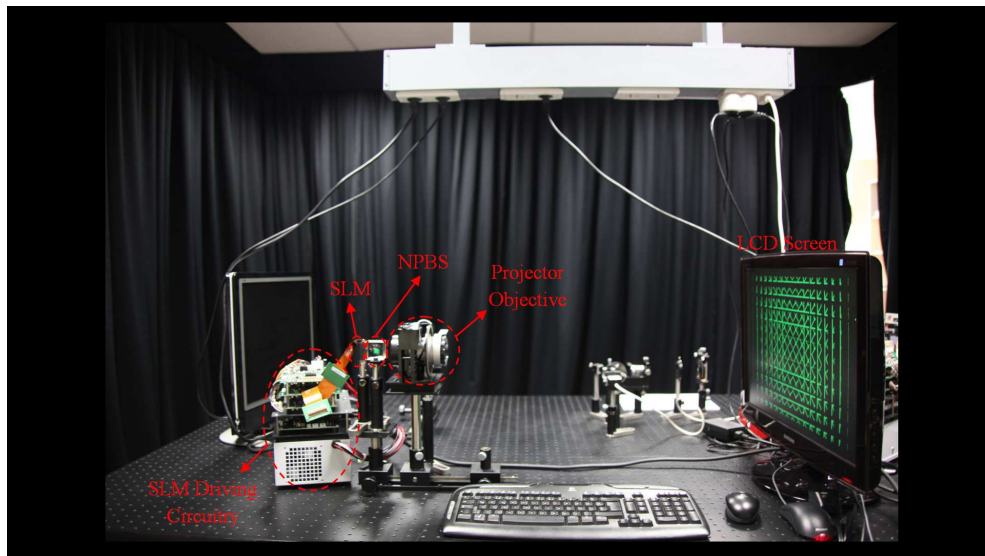


Figure 4.14: Picture of the entire optical setup. (Reprinted from “Integral imaging based 3D display of holographic data,” Ali Özgür Yöntem and L. Onural, *Opt. Express* vol. 20, no. 22, pp.24175-24195, 2012. ©2012 OSA.)

4.5 Numerical and Optical Results

We compared the computer simulation results and the optical reconstructions. Here we present the results for each example given in Section 4.3.

Our first example was two letters at different depths and location. To determine the focused planes we put two cards with “Bilkent University” label on them as shown in Fig. 4.16. The card, where the label is horizontally aligned, is

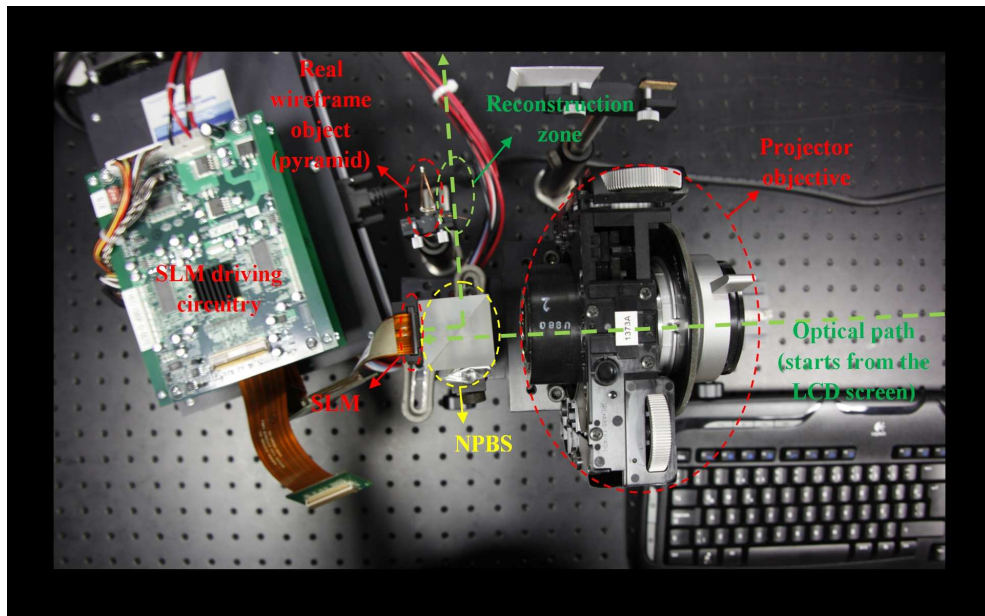


Figure 4.15: Top view of the optical setup. There is a wireframe pyramid object next to the reconstruction zone. It is used to compare the reconstructed 3D images of the pyramid object. (Reprinted from “Integral imaging based 3D display of holographic data,” Ali Özgür Yöntem and L. Onural, *Opt. Express* vol. 20, no. 22, pp.24175-24195, 2012. ©2012 OSA.)

located $8.4f$ distance away from the SLM surface. The one with the label, which is vertically aligned, is located approximately at $13f$ away from the SLM surface. When we display the elemental images in Fig. 4.4, we observed the reconstructions as in Fig. 4.17. In this figure, the top images are computer simulation results while the bottom images are the optical reconstructions. The images on the left shows the reconstructed object at $8.4f$ while the right images are the reconstructions of the object at $13f$. The letter “A” is seen sharper than the letter “Z”. This is due to the depth of focus of the lenslets. We exaggerate the distances to show that the system works. For a closer capture distance, for the letter “Z”, the reconstructions would be sharper. As we explained in Sec. 4.4, the NPBS shifts the focal distance of the lenslets. We also confirmed these shifted location by computer simulations.

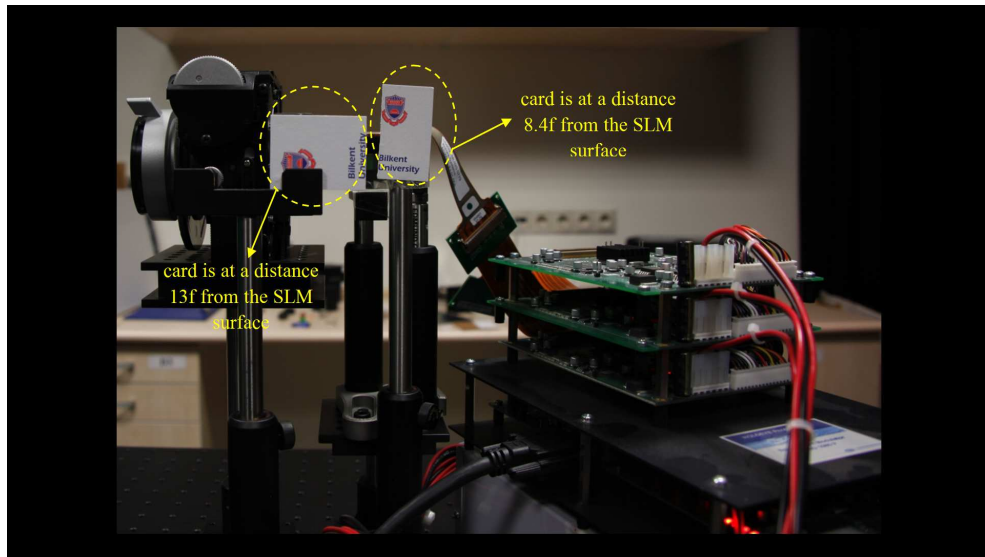


Figure 4.16: The viewing zone of the optical setup. We placed cards labeled as “Bilkent University” at different distances in order to check the reconstruction distances. (Reprinted from “Integral imaging based 3D display of holographic data,” Ali Özgür Yöntem and L. Onural, *Opt. Express* vol. 20, no. 22, pp.24175-24195, 2012. ©2012 OSA.)

For the second object, the pyramid, we performed two experiments. The first experiment is to show the depth of the object and the second one is to show the parallax. In Fig. 4.15, we show how we modified the setup. In Fig. 4.18, left images are the computer simulation results and the right images are the optical

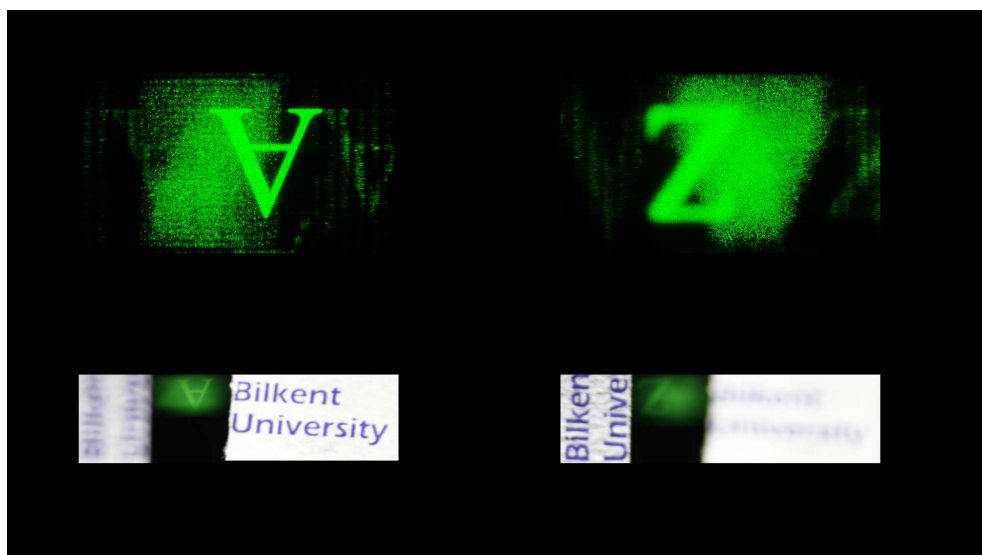


Figure 4.17: 3D reconstruction from the elemental images of Fig. 4.4. At the top, digital reconstructions are shown while at the bottom we observe the optical counterparts. On the left side, the camera, which took this picture, was focused to a distance $8.4f$ and on the right side, it was at $13f$. (We enhanced the brightness of the computer simulation results for visual purposes.) (Reprinted from “Integral imaging based 3D display of holographic data,” Ali Özgür Yöntem and L. Onural, *Opt. Express* vol. 20, no. 22, pp.24175-24195, 2012. ©2012 OSA.)

reconstructions together with a physical wireframe pyramid object with the same size as the reconstruction. The top two images show the focusing to the tip of the pyramid. The depth of the object is $24mm$ as mentioned in Section 4.2. The base part of the pyramid, which is located $8.4f$ away from the SLM surface, is shown in focus in the bottom part of Fig. 4.18. For the parallax experiment, we shoot photos from three different viewing angles from left to right. We focused to the tip in order to show the parallax better. In Fig. 4.19, the top three images are computer simulations for the parallax, while the bottom pictures are the optical reconstructions. This effect can be seen better with the optical reconstructions. However, the viewing angle of the system, is limited with the maximum diffraction angle of the SLM device, $\omega = \frac{\lambda}{X} = \frac{532nm}{8\mu m} = 0.067rad \approx 4^\circ$, [47, 54]. The aliased components appear when we go to higher angles to observe the reconstruction. This is seen both in the optical reconstruction and in the computer simulations. Viewing angle of this system can be improved by decreasing the pixel period, X , of the SLM device or by introducing multiple SLM circular configurations [21, 22, 76].

The third example was the epithelium cell object. The top image in Fig. 4.20 shows the computer simulation results. The bottom image shows the reconstruction at $8.4f$. Since the object has a small depth, it is not possible to observe a 3D effect or the parallax. However, we showed with this last example that it is possible to convert holographic recording, regardless of the acquisition method (numerical data generation or digital recording of optical data), to elemental images and reconstruct them successfully by numerical or optical means.

For the last example, the toy object, the numerical and optical reconstructions of these elemental images are given in Fig. 4.21 and Fig. 4.22, respectively.

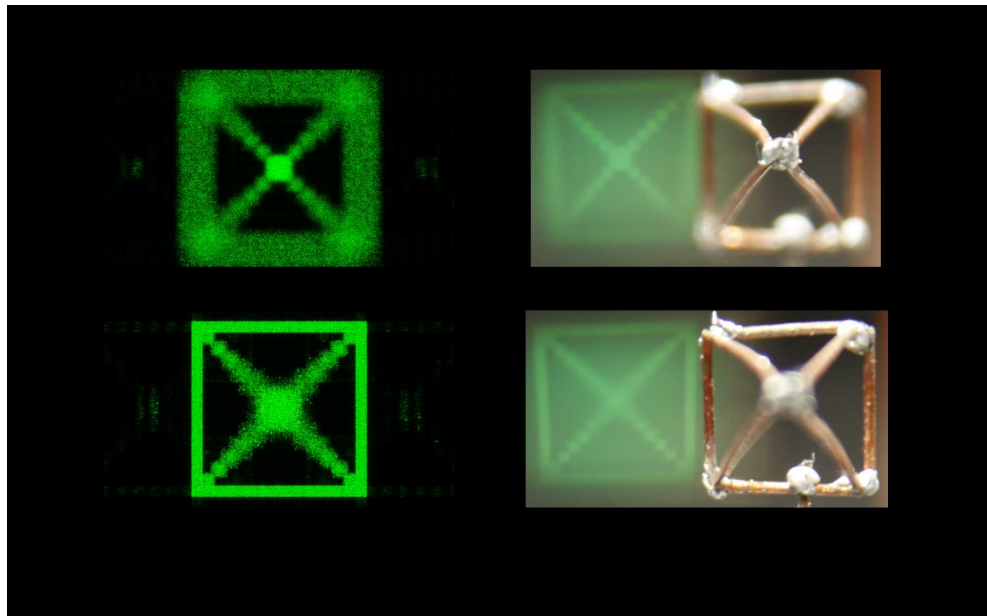


Figure 4.18: 3D reconstruction from the elemental images of Fig. 4.6. Images at the left are digital reconstructions. Images at the right are optical reconstructions. The top images are focused to the tip of the pyramid object and the images at the bottom are focused to the base of the object. It is clearly seen that the physical (wire) object and the reconstructed 3D images match. (We enhanced the brightness of the computer simulation results for visual purposes.) (Reprinted from “Integral imaging based 3D display of holographic data,” Ali Özgür Yöntem and L. Onural, *Opt. Express* vol. 20, no. 22, pp.24175-24195, 2012. ©2012 OSA.)

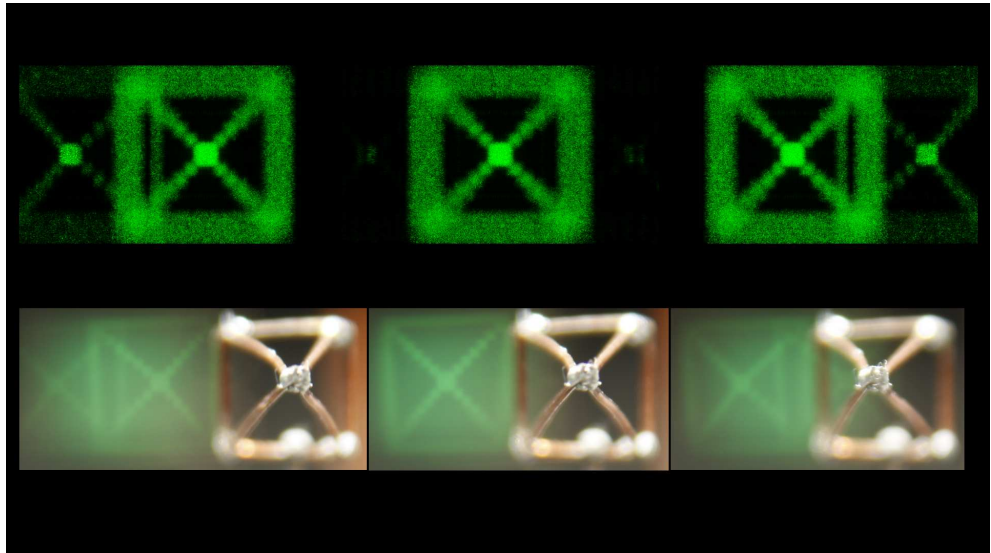


Figure 4.19: The pictures of the pyramid image taken from three different angles. (All are focused to the tip of the pyramid.) The pictures at the top are the digital reconstructions and the bottom ones are the optical reconstructions. The pictures show the parallax and the viewing angle. (We enhanced the brightness of the computer simulation results for visual purposes.) (Reprinted from “Integral imaging based 3D display of holographic data,” Ali Özgür Yöntem and L. Onural, *Opt. Express* vol. 20, no. 22, pp.24175-24195, 2012. ©2012 OSA.)

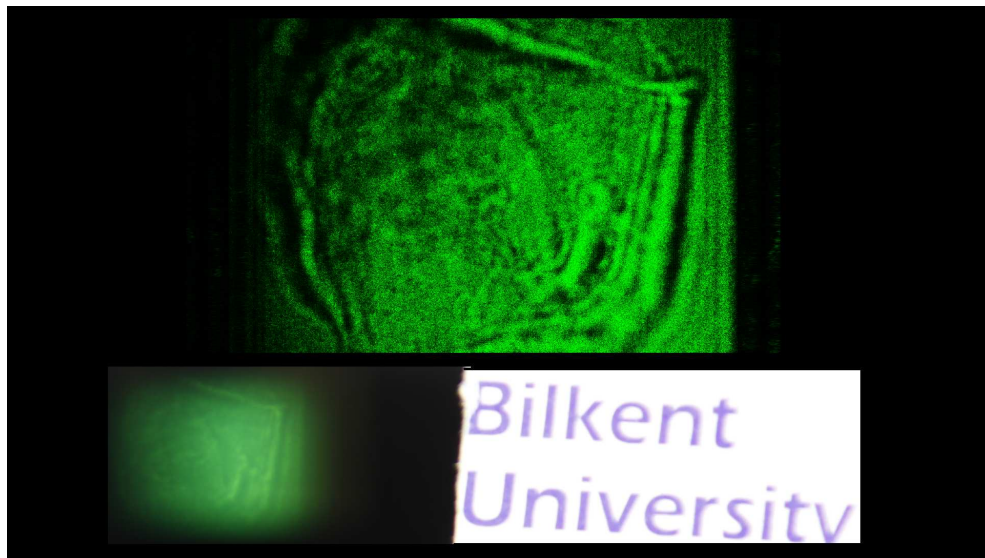


Figure 4.20: Reconstruction from the elemental images of Fig. 4.8. Top picture is the digital reconstruction whereas the bottom one shows the optical reconstruction. Since the object thickness is small relative to the reconstruction distance, a 3D depth is not perceived. However, the planar looking thin object still floats in 3D space. (We enhanced the brightness of the computer simulation results for visual purposes.) (The hologram data, from which this reconstruction was obtained, was courtesy of cole Polytechnique Fdrale de Lausanne within the Real 3D project.) (Reprinted from “Integral imaging based 3D display of holographic data,” Ali Özgür Yöntem and L. Onural, *Opt. Express* vol. 20, no. 22, pp.24175-24195, 2012. ©2012 OSA.)



Figure 4.21: Numerical reconstructions of the elemental images of the toy object. (The hologram data, from which this reconstruction was obtained, was courtesy of National University of Ireland, Maynooth within the Real 3D project.)



Figure 4.22: Optical reconstructions of the elemental images of the toy object. (The hologram data, from which this reconstruction was obtained, was courtesy of National University of Ireland, Maynooth within the Real 3D project.)

We also present the results of the numerical and optical reconstruction of a STAR WARS action figure “Storm Trooper”. The elemental images are again obtained from a physical holographic recording. The input data is similar to the last example given in Sec. 4.3. However, the parameter in the diffraction calculation in Eq. (4.7) is $\chi = \pi\lambda_1 \left(z_1 \frac{x^2}{X_1^2} \right)$. The numerical reconstruction of the hologram data is shown in Fig. 4.23. The elemental images of the holographic data is shown in Fig. 4.24. Finally, the numerical and optical reconstructions of these elemental images are depicted in Fig. 4.25 and Fig. 4.26, respectively.



Figure 4.23: Digital reconstruction of the hologram of STAR WARS action figure: Storm Trooper. (The hologram data, from which this reconstruction was obtained, was courtesy of National University of Ireland, Maynooth within the Real 3D project.)

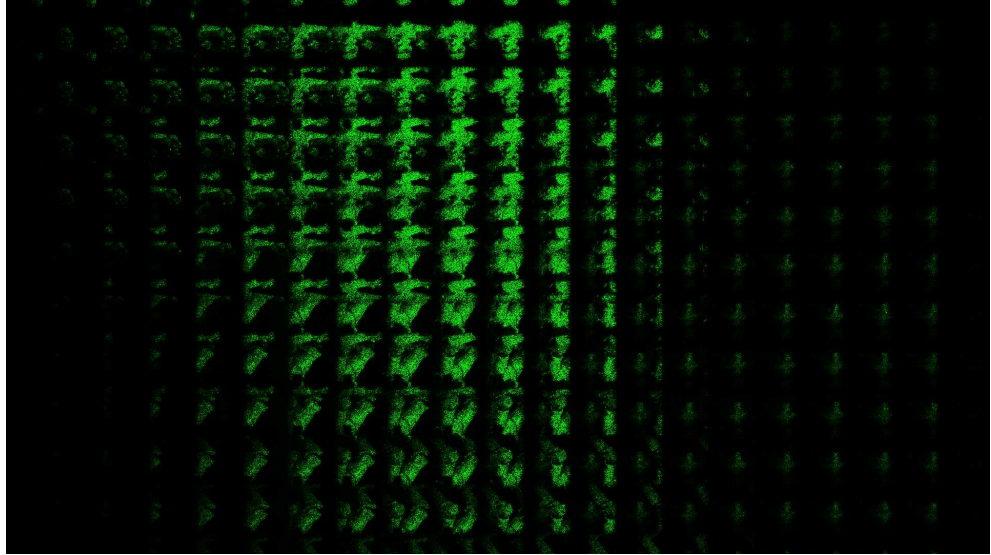


Figure 4.24: Elemental images obtained from the holographic data of the “Storm Trooper” action figure. (The hologram data, from which this reconstruction was obtained, was courtesy of National University of Ireland, Maynooth within the Real 3D project.)

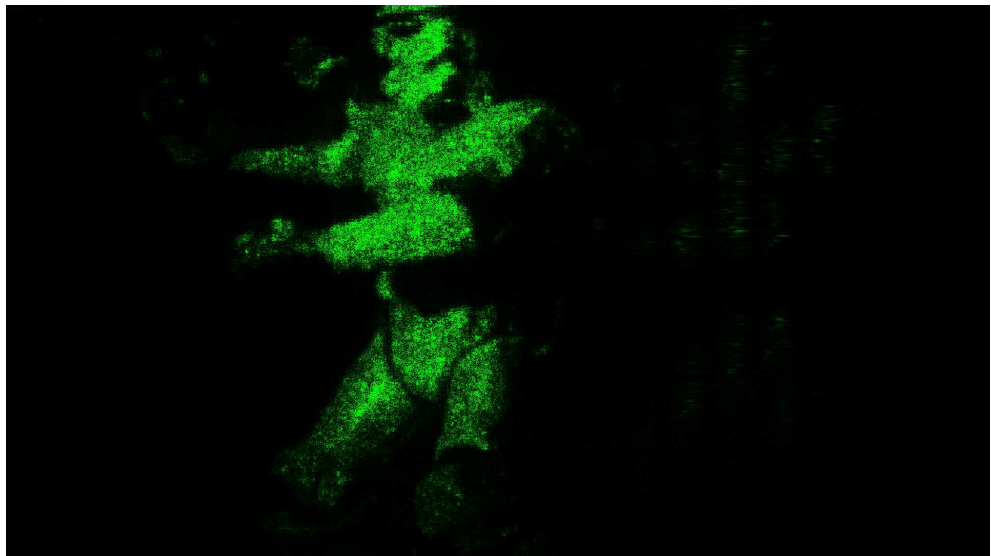


Figure 4.25: Numerical reconstruction of the elemental images in Fig. 4.24. (The hologram data, from which this reconstruction was obtained, was courtesy of National University of Ireland, Maynooth within the Real 3D project.)



Figure 4.26: Optical reconstruction of the elemental images in Fig. 4.24. (The hologram data, from which this reconstruction was obtained, was courtesy of National University of Ireland, Maynooth within the Real 3D project.)

Chapter 5

OBTAINING ORTHOSCOPIC ELEMENTAL IMAGES FROM PSEUDOSCOPIC ELEMENTAL IMAGES

In this short chapter, we will present a practical solution to pseudoscopic reconstruction problem by applying similar steps as in our numerical elemental image generation method. We will also demonstrate the numerical and optical results. In the results, we will use the same example as in the previous section: two letters at two different depths.

5.1 The Pseudoscopic-Orthoscopic Conversion Method

We introduced an intermediate conversion step by simply simulating the two-step optical solution given by [15, 32, 61]. In the computations, we applied wave propagation tools [52, 73], instead of ray tracing methods [29–31]. Fig. 5.1 shows

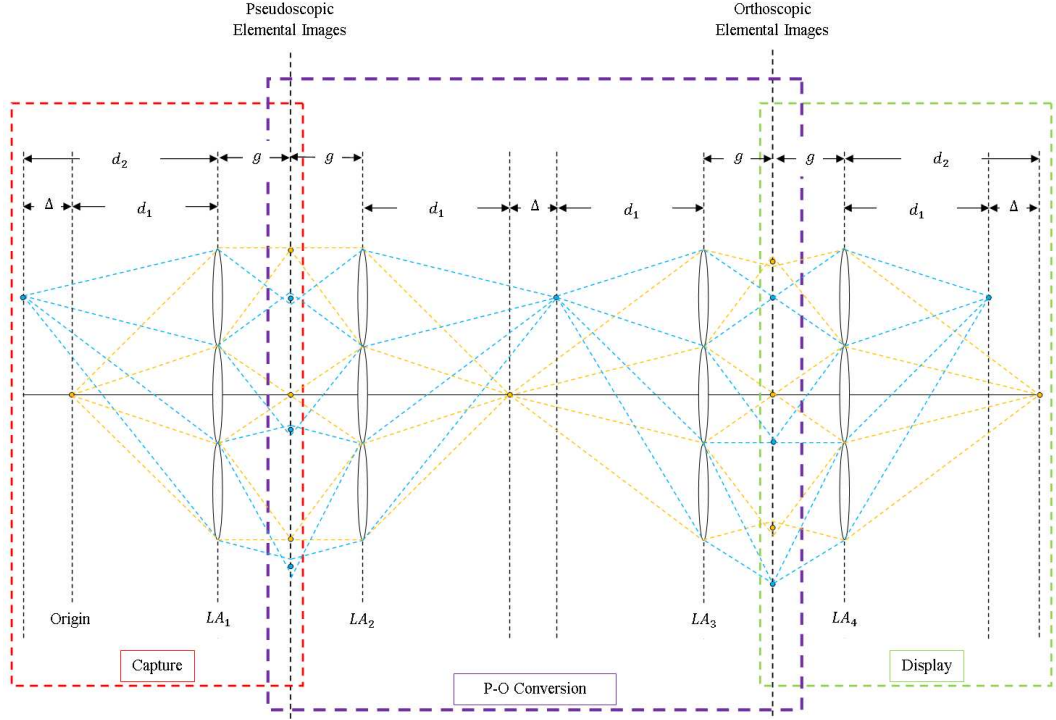


Figure 5.1: Orthoscopic reconstruction process

the steps to obtain an orthoscopic 3D reconstruction. The dashed box on the left (colored in red) is the standard elemental image generation (capture) process. The dashed box at the right (colored in green) shows the reconstruction (display) process. The dashed box in the middle (colored in violet) is the pseudoscopic to orthoscopic conversion process. The conversion process is symmetrical in terms of the distances. The input of this process is an elemental image set which gives a pseudoscopic reconstruction. The output is another elemental image set that gives orthoscopic reconstruction of the original 3D object.

In our experiments, we optically reconstructed the 3D images of the objects using our display proposed Sec. 4.4. We conducted the experiments with both elemental image sets. For comparison, we also obtained the numerical results using Eqs. (4.8) and (4.9). The input 3D object can either be synthetically generated or physically obtained. The generation of the elemental images from the input 3D object is a computational process. The model for the orthoscopic elemental image generation is given in Fig. 5.2. In Fig. 5.2(a), the standard operation to obtain pseudoscopic elemental images is depicted. The input to the

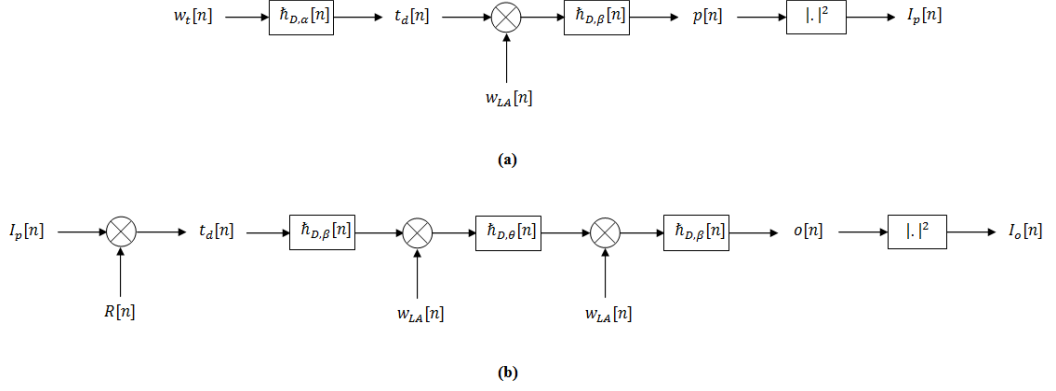


Figure 5.2: Orthoscopic elemental image generation process model

model is the diffraction field located at the origin, which is the effective depth of the nearest point of the object to LA_1 as given in Fig. 5.1. This distance is measured as d_1 . The input diffraction field is propagated to the lenslet array plane using Eq. (4.1). The resultant diffraction field, $t_d[\mathbf{n}]$, is multiplied with the window, $w_{LA}[\mathbf{n}]$, containing the lenslet array pattern and then, it is propagated once more to a distance g using Eq. (4.2). Finally, we obtain the pseudoscopic elemental images, $I_p[\mathbf{n}]$, by taking the square magnitude of the resulting field, $p[\mathbf{n}]$. Until this point we have simulated the left dashed box given in Fig. 5.1.

The simulation model of the intermediate part in Fig. 5.1 is given in Fig. 5.2(b). The process is as follows: first, we multiplied $I_p[\mathbf{n}]$ with a random phase, $R[\mathbf{n}]$. The field, $o[\mathbf{n}]$, is obtained from this resultant complex field, $t_d[\mathbf{n}]$ by the following operations:

$$\begin{aligned}
 t_{d_1}[\mathbf{n}] &= ID\hat{F}T \left\{ D\hat{F}T \{ w_t[\mathbf{n}] \} g_{D,\beta'}[\mathbf{k}] \right\} , \\
 t_{d_2}[\mathbf{n}] &= t_{d_1}[\mathbf{n}] w_{LA}[\mathbf{n}] , \\
 t_{d_3}[\mathbf{n}] &= ID\hat{F}T \left\{ D\hat{F}T \{ t_{d_2}[\mathbf{n}] \} g_{D,\theta'}[\mathbf{k}] \right\} , \\
 t_{d_4}[\mathbf{n}] &= t_{d_3}[\mathbf{n}] w_{LA}[\mathbf{n}] , \\
 o[\mathbf{n}] &= ID\hat{F}T \left\{ D\hat{F}T \{ t_{d_4}[\mathbf{n}] \} g_{D,\beta'}[\mathbf{k}] \right\}
 \end{aligned} \tag{5.1}$$

where $\beta' = \pi\lambda g$ and $\theta' = \pi\lambda(2d_1 + \Delta)$. Finally, the intensity, $I_o[\mathbf{n}]$, of $o[\mathbf{n}]$ gives the orthoscopic elemental images of the original 3D object.

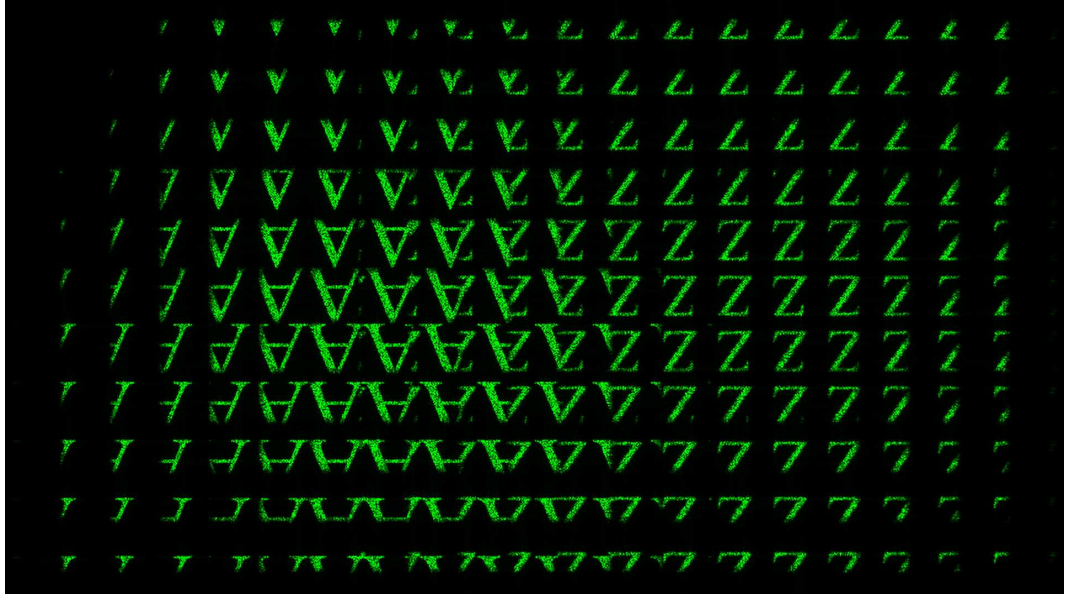


Figure 5.3: Pseudoscopic elemental images

5.2 Examples and Results

This time we will slightly change the object positions. As we mentioned in Sec. 4.5, the lenslets have a limited depth of focus. So, only a certain depth of an object/scene with a large depth will be sharply reconstructed. We exaggerated the depths at that section. Now, we will bring the letters closer. We put the letter “A” again at $d_1 = 7f$ and we placed letter “Z” at $\Delta = 3f$ behind. We separated the letters in the transversal plane, enough to distinguish the focused and unfocused parts. Again we used the lenslet array given in Fig. 4.13. The computed pseudoscopic and orthoscopic elemental images are given in Fig. 5.3 and Fig. 5.4 respectively.

The numerical reconstructions for these elemental images are given in Fig. 5.5. The first row of the image is the pseudoscopic reconstructions and the second row is the orthoscopic reconstructions. In the first column, the focused images at the distance $7f$ are presented whereas in the second column, the focused images at $10f$ are shown.

The optical reconstructions of the elemental images are shown in Fig. 5.6.



Figure 5.6: Optical reconstructions of the elemental images in Fig. 5.3 and Fig. 5.4 are shown. The results are placed in the same way as in Fig. 5.5.

The reconstructed images are placed in the same way as in Fig. 5.5. The results clearly show that the method works. The usual focal shifting due to the NPBS is observed in the optical reconstructions. So, the optical reconstruction distances are again different from the numerical ones. However, the order of the letters on the z -axis are preserved.

Chapter 6

CONCLUSIONS

We proposed two integral imaging systems. These systems use diffractive optical elements unlike the conventional ones. Since the implemented systems have digital lenslets, we have reviewed the analysis of a discrete lenslet. Such a lenslet causes multiple focal points and higher diffraction orders of these focal points at each focal distance. Multiple focal points are caused by the quantization whereas the higher diffraction orders are caused by the pixelated structure.

When we look at the case of an array of such lenslets, we observe that the multiple focal points and higher diffraction orders from each such lenslet in the array coincide if the period of the lenslet is chosen to be equal to the lenslet size.

It is easy to numerically generate, any type of lenslet array by changing the physical parameters like focal length, size and even the phase distribution. To realize these synthetic lenslet arrays physically, we need electronically controllable devices. One easy way to obtain such lenslet arrays is to write numerically generated Fresnel lenslet array patterns on a phase-only LCoS spatial light modulator. As a consequence, we obtain discrete lenslet arrays.

We analyzed the capture part of such an integral imaging setup. We used a discrete lenslet array to image 3D impulsive source points and we obtained an elemental image set at the main image plane. There are additional image

planes present due to multiple focal length property of discrete lenslets. These higher-order images introduce additional artefact terms on the elemental images in addition to the blurring as a consequence of out of focus term due to the limited depth of focus of the lenslets. It is possible to reduce the effects of such artefacts by selecting the focal length of the lenslets such that they cover the entire normalized frequency range and the imaging distance (the distance between the lenslet array and a reference plane on the closest point of the object to the lenslet array) much larger than the object depth.

We performed wave propagation simulations of discrete lenslets based on Fresnel diffraction kernel. The results support the theoretical analysis. We also performed a simulation to image a diffusive planar object. As it is expected, we obtained elemental images at multiple planes. We observed the artefacts indicated by the theoretical analysis on the obtained elemental images. The severity of the artefacts are significant on the image planes at the fractions of the main image plane.

We implemented the first proposed integral imaging setup. In order to eliminate alignment problems between the capture and the display setups, we constructed the integral imaging setup such that the display part immediately follows the capture part and shares the elemental image plane. At the transition plane, we placed a diffuser. The diffuser replaced the capture device (CCD) and the display device (LCD) used in the conventional setups. The crucial analog element of the system, that is the lenslet array, was realized as a phase pattern written on a phase-only LCoS SLM in both parts of the system. We used one such SLM at the capture part and another one at the display part of the system. The SLMs are reflective type. So, non-polarizing beams splitters (NPBS) are placed before the SLMs. The NPBS shift the focal lengths of the lenslets. Therefore, theoretical imaging distances are different than the practical ones. Furthermore, the NPBS decreases the light throughput of the system at least by 50%. To control the depth and size of the input objects, we placed a projector objective between the capturing SLM and the input object. When a passive 3D object is illuminated by an external source, because of the limited diffraction efficiency of the SLM

device, an undiffracted light at the background together with the elemental images is visible. Furthermore, the intensities of the elemental images were lower compared to this undiffracted light. This makes it difficult to observe the reconstruction at the display part. The lenslet array causes chromatic aberration since a single SLM is designed to work best for a single wavelength. However, the system successfully images a self-luminous object obtained by masking a 2D single wavelength LED array. Experimental results show that within the physical limitations (maximum diffraction angle, which is dependent on the pixel period and total number of pixels) of the SLM device, a good optical reconstruction is possible with the proposed system. Thus, we have implemented an integral imaging system with a full digital capture and display lenslet arrays. Most of the integral imaging systems require special type of lenslets (i.e. phase apodized) to improve the quality of the integral imaging system. These are generally hard and costly to manufacture. With our proposed system, it is possible to construct cost efficient and simple integral imaging systems.

For digital applications, i.e. games, animations, etc., where we do not need to shoot real data, we only need digital data to display on a screen. We obtained computer generated elemental images by using wave propagation methods, instead of the commonly used method ray tracing, to generate elemental images from digitally available 3D data (synthetic or digitally recorded holographic data). Thus, it is possible to relate holographic data to elemental images data. We showed several examples including digitally captured holographic data.

We also used discrete lenses for our second proposed integral imaging system which is display-only. This system uses a LCD screen to display computer generated elemental images and these elemental images are shrunk in size to match the size of the SLM which is used to realize the discrete lenslet array. Again we placed NPBS before the reflective type SLM. Imaging distance again changed because of the shift of the focal length. The amount of light throughput is again lowered by the NPBS. However, this time the severity of the optical loss is low compared to the first system. Optical reconstructions of 3D images of synthetic and physical objects are obtained from this display setup. Both digitally simulated reconstructions (obtained using diffraction calculations) and optical reconstructions

are compared for these examples. With these several examples we showed several properties of the display, such as depth of focus, viewing angle which is limited by the maximum diffraction angle of the SLM, transversal and depth resolution of the display, etc. Therefore, our proposed display system and the method for obtaining elemental images make it possible to display holographic recordings on an integral imaging display setup.

The direct reconstruction of elemental images results in reverse depth (pseudoscopic) image, that is, closer object points are observed as far away points in the image. We solve pseudoscopic image problem of the integral imaging method by applying a modified version of our algorithm on one of the proposed solutions in the previous studies. Our algorithm converts an elemental image set that gives pseudoscopic reconstruction to another set of elemental images that gives orthoscopic image reconstruction. Therefore, we showed that we can also use wave propagation methods to obtain elemental images that give correct depth information. Numerically and optically obtained reconstructions using resulting elemental images are consistent.

Our results show that fully digital integral imaging systems are possible by using digital lenslet arrays realized by electro-optical devices.

Bibliography

- [1] I. Sexton and P. Surman, "Stereoscopic and autostereoscopic display systems," *IEEE Signal Proc. Mag.*, vol. 16, pp. 85–99, 1999.
- [2] P. Benzie, J. Watson, P. Surman, I. Rakkolainen, K. Hopf, H. Urey, V. Sainov, and C. von Kopylow, "A survey of 3DTV displays: techniques and technologies," *IEEE T. Circ. and Syst. Vid.*, vol. 17, pp. 1647–1658, 2007.
- [3] G. B. Esmer, *Calculation of scalar optical diffraction field from its distributed samples over the space*. PhD thesis, Dept. of Electrical and Electronics Engineering, Bilkent University, 2010.
- [4] D. Gabor, "Holography, 1948-1971," *P. IEEE*, vol. 60, pp. 655–668, 1972.
- [5] B. E. A. Saleh and M. C. Teich, *Fundamentals of Photonics*. New York: John Wiley and Sons, Inc., 1991.
- [6] C. Quan, X. Kang, and C. J. Tay, "Speckle noise reduction in digital holography by multiple holograms," *Opt. Eng.*, vol. 46, pp. 1158011–1158016, 2007.
- [7] J. G.-Sucerquia, J. A. H. Ramirez, and D. V. Prieto, "Reduction of speckle noise in digital holography by using digital image processing," *Optik*, vol. 116, pp. 44–48, 2005.
- [8] T. Baumbach, V. K. E. Kolenovic, and W. Juptner, "Improvement of accuracy in digital holography by use of multiple holograms," *Appl. Optics*, vol. 45, pp. 6077–6085, 2006.

- [9] T. Ito and K. Okano, “Color electroholography by three colored reference lights simultaneously incident upon one hologram panel,” *Opt. Express*, vol. 12, pp. 4320–4325, 2004.
- [10] F. Yaraş and L. Onural, “Color holographic reconstruction using multiple slms and led illumination,” *P. SPIE*, vol. 7237, pp. 72370O1–72370O5, 2010.
- [11] N. A. Dodgson, “Autostereoscopic 3D displays,” *IEEE Computer Society*, pp. 31–36, 2005.
- [12] H. Urey, K. Chellappan, E. Erden, and P. Surman, “State of the art in stereoscopic and autostereoscopic displays,” *P. IEEE*, vol. 99, pp. 540–555, 2011.
- [13] L. Onural, *3D Video Technologies: An Overview of Research Trends*. Bellingham, Washington: SPIE Press, 2011.
- [14] G. Lippmann, “La photographie integrale,” *C.R.Hebd. Seances Acad. Sci.*, vol. 146, pp. 446–451, 1908.
- [15] H. E. Ives, “Optical properties of a Lippman lenticulated sheet,” *Opt. Soc. Am.*, vol. 21, pp. 171–176, 1931.
- [16] F. Okano, H. Hoshino, H. A. Jun, and I. Yuyama, “Real-time pickup method for a three-dimensional image based on the integral photography,” *Appl. Optics*, vol. 36, pp. 1–14, 1997.
- [17] T. Okoshi, “Optimum design and depth resolution of lens-sheet and projection-type three-dimensional displays,” *Appl. Opt.*, vol. 10, pp. 2284–2291, 1971.
- [18] C. B. Burckhardt, “Optimum parameters and resolution limitation of integral photography,” *J. Opt. Soc. Am.*, vol. 58, pp. 71–76, 1968.
- [19] R. Martinez-Cuenca, G. Saavedra, M. Martinez-Corral, and B. Javidi, “Integral imaging with improved depth of field by use of amplitude-modulated microlens arrays,” *Appl. Optics*, vol. 43, pp. 5806–5813, 2004.

- [20] Y. Frauel, A. Castro, and B. Javidi, “Integral imaging with large depth of field using an asymmetric phase mask,” *Opt. Soc. Am.*, vol. 15, 2007.
- [21] Y. Kim, J.-H. Park, S.-W. Min, S. Jung, H. Choi, and B. Lee, “Wide-viewing-angle integral three-dimensional imaging system by curving a screen and a lens array,” *Appl. Optics*, vol. 44, pp. 546–552, 2005.
- [22] J. Hyun, D.-C. Hwang, D.-H. Shin, B.-G. Lee, and E.-S. Kim, “Curved projection integral imaging using an additional large-aperture convex lens for viewing angle improvement,” *ETRI J.*, vol. 31, pp. 105–110, 2009.
- [23] B. Lee, S. Jung, and J.-H. Park, “Viewing-angle-enhanced integral imaging by lens switching,” *Opt. Lett.*, vol. 27, pp. 818–820, 2002.
- [24] R. Martnez-Cuenca, H. Navarro, G. Saavedra, B. Javidi, and M. Martnez-Corral, “Enhanced viewing-angle integral imaging by multiple-axis telecentric relay system,” *Opt. Express*, vol. 15, pp. 16255–16260, 2007.
- [25] W. D. Furlan, M. Martinez-Corral, and B. Javidi, “Analysis of 3-D integral imaging displays using the wigner distribution,” *J. Disp. Technol.*, vol. 2, pp. 180–185, 2006.
- [26] R. Martnez-Cuenca, G. Saavedra, M. Martnez-Corral, and B. Javidi, “Enhanced depth of field integral imaging with sensor resolution constraints,” *Opt. Express*, vol. 12, pp. 5237–5242, 2004.
- [27] J.-S. Jang and B. Javidi, “Large depth-of-focus time-multiplexed three-dimensional integral imaging using lenslets with non-uniform focal lengths and aperture sizes,” *IEEE LEOS Ann. Mtg.*, vol. 1, pp. 258–259, 2004.
- [28] J.-S. Jang, F. Jin, and B. Javidi, “Three-dimensional integral imaging with large depth of focus by use of real and virtual image fields,” *Opt. Lett.*, vol. 28, pp. 1421–1423, 2003.
- [29] M. Martnez-Corral and B. Javidi, “Formation of real, orthoscopic integral images by smart pixel mapping,” *Opt. Express*, vol. 13, pp. 9175–9180, 2005.

- [30] H. Navarro, R. Martinez-Cuenca, G. Saavedra, M. Martinez-Corral, and B. Javidi, “3D integral imaging display by smart pseudoscopic-to-orthoscopic conversion (spoc),” *Opt. Express*, vol. 18, pp. 25573–25583, 2010.
- [31] J.-Y. Jang, S.-H. Park, S. Cha, and S.-H. Shin, “Three-dimensional integral imaging for orthoscopic real image reconstruction,” *P. SPIE*, vol. 5636, pp. 379–386, 2005.
- [32] J. Arai, F. Okano, H. Hoshino, and I. Yuyama, “Gradient-index lens-array method based on real-time integral photography for three-dimensional images,” *Appl. Optics*, vol. 37, pp. 2034–2045, 1998.
- [33] Z. Wnag, S. H. Eng, and K. Alameh, “Design and optimization of programmable lens array for adaptive optics,” *P. SPIE*, vol. 6414, 2007.
- [34] L. Zhao, N. Bai, X. Li, L. S. Ong, Z. P. Fang, and A. K. Asundi, “Efficient implementation of a spatial light modulator as a diffractive optical microlens array in a digital shack-hartmann wavefront sensor,” *Appl. Optics*, vol. 45, pp. 90–94, 2006.
- [35] E. Carcole, J. Campos, and S. Bosch, “Diffraction theory of Fresnel lenses encoded in low resolution devices,” *Appl. Optics*, vol. 33, pp. 162–174, 1994.
- [36] M. K. Giles, “Applications of programmable spatial light modulators,” *Society of Optical and Quantum Electronics*, 1996.
- [37] H. Dai, K. X. Y. Liu, X. Wang, and J. Liu, “Characteristics of lcos phase only spatial light modulator and its applications,” *Opt. Commun.*, vol. 238, pp. 269–276, 2004.
- [38] J. A. Davis, D. M. Cottrell, R. A. Lilly, and S. W. Connely, “Multiplexed phase-encoded leses written on spatial light modulators,” *Opt. Soc. Am.*, vol. 14, pp. 420–422, 1989.
- [39] D. M. Cottrell, J. A. Davis, T. R. Hedman, and R. A. Lilly, “Multiple imaging phase-encoded optical elements written as programmable spatial light modulators,” *Appl. Optics*, vol. 29, pp. 2505–2509, 1990.

- [40] J.-S. Jang and B. Javidi, “Three-dimensional integral imaging with electronically synthesized lenslet arrays,” *Opt. Lett.*, vol. 27, pp. 1767–1769, 2002.
- [41] M. J. Yzuel, J. Campos, A. Marquez, J. C. Escalera, J. A. Davis, C. Iemmi, and S. Ledesma, “Inherent apodization of lenses encoded on liquid-crystal spatial light modulators,” *Opt. Express*, vol. 39, pp. 6034–6039, 2000.
- [42] Y. Jeong, S. Jung, J.-H. Park, and B. Lee, “Reflection-type integral imaging scheme for displaying three-dimensional images,” *Opt. Lett.*, vol. 27, pp. 704–706, 2002.
- [43] Z. Kavehvasht, K. Mehrany, and S. Bagheri, “Improved resolution three-dimensional integral imaging using optimized irregular lens-array structure,” *J. Opt. Soc. Am.*, vol. 51, pp. 6031–6037, 2012.
- [44] S. S. Athineos, N. P. Sgouros, P. G. Papageorgas, D. E. Maroulis, M. S. Sangriotis, and N. G. Theofanous, “Photorealistic integral photography using a ray-traced model of capturing optics,” *J. Electron. Imaging*, vol. 15, 2006.
- [45] S.-W. Min, K. S. Park, B. Lee, Y. Cho, and M. Hahn, “Enhanced algorithm of image mapping method for computer-generated integral imaging system,” *Jpn. J. Appl. Phys.*, vol. 45, pp. L744–L747, 2006.
- [46] S.-H. Lee, S.-C. Kim, and E.-S. Kim, “Reconstruction of digital hologram generated by sub-image of integral imaging,” *P. SPIE*, vol. 6912, 2008.
- [47] S.-W. Min, S. Jung, J.-H. Park, and B. Lee, “Three-dimensional display system based on computer-generated integral photography,” *P. SPIE*, vol. 4297, pp. 187–195, 2001.
- [48] J.-K. Lee, S.-C. Kim, and E.-S. Kim, “Reconstruction of three-dimensional object and system analysis using ray tracing in practical integral imaging system,” *P. SPIE*, vol. 6695, 2007.
- [49] B.-N.-R. Lee, Y. Cho, K. Park, S.-W. Min, J.-S. Lim, M. C. Whang, and K. R. Park, “Design and implementation of a fast integral image rendering method,” *Lect. Notes Comput. Sc.*, vol. 4161, pp. 135–140, 2006.

- [50] U. Schnars and W. P. O. Juptner, “Digital recording and numerical reconstruction of holograms,” *Meas. Sci. Technol.*, vol. 13, pp. R85–R110, 2002.
- [51] L. Onural, “Sampling of the diffraction field,” *Appl. Optics*, vol. 39, pp. 5929–5935, 2000.
- [52] A. Ö. Yöntem and L. Onural, “Integral imaging using phase-only LCoS spatial light modulators as fresnel lenslet arrays,” *J. Opt. Soc. Am. A*, vol. 28, pp. 2359–2375, 2011.
- [53] J. W. Goodman, *Introduction to Fourier Optics*. New York: Mc-Graw-Hill, 1996.
- [54] T. Mishina, M. Okui, and F. Okano, “Generation of holograms using integral photography,” *P. SPIE*, vol. 5599, pp. 114–122, 2004.
- [55] R. V. Pole, “3-D imagery and holograms of objects illuminated in white light,” *Appl. Phys. Lett.*, vol. 10, pp. 20–22, 1967.
- [56] M. Hain, W. von Spiegel, M. Schmiedchen, and B. J. T. Tschudi
- [57] I. Bergoend, C. Arfire, N. Pavillon, and C. Depeursinge, “Diffraction tomography for biological cells imaging using digital holographic microscopy,” *P. SPIE*, vol. 7376, pp. 7376131–7376138, 2010.
- [58] D. Mas, J. Garcia, C. Ferreira, L. M. Bernardo, and F. Marinho, “Fast algorithms for free-space diffraction patterns calculation,” *Opt. Commun.*, vol. 164, pp. 233–245, 1999.
- [59] H. Kang, T. Fujii, T. Yamaguchi, and H. Yoshikawa, “Compensated phase-added stereogram for real-time holographic display,” *Opt. Eng.*, vol. 46, 2007.
- [60] T. Shimobaba, T. Ito, N. Masuda, Y. Abe, Y. Ichihashi, H. Nakayama, N. Takada, A. Shiraki, and T. Sugie, “Numerical calculation library for diffraction integrals using the graphic processing unit: the gpu-based wave optics library,” *J. Opt. A: Pure Appl. Opt.*, vol. 10, 2009.

- [61] J.-S. Jang and B. Javidi, “Two-step integral imaging for orthoscopic three-dimensional imaging with improved viewing resolution,” *Opt. Eng.*, vol. 41, pp. 2568–2571, 2002.
- [62] E. Şahin and L. Onural, “Scalar diffraction field calculation from curved surfaces via Gaussian beam decomposition,” *J. Opt. Soc. Am. A*, vol. 29, pp. 1459–1469, 2012.
- [63] L. Onural, “Exact solution for scalar diffraction between tilted and translated planes using impulse functions over a surface,” *J. Opt. Soc. Am. A*, vol. 28, pp. 290–295, 2011.
- [64] G. C. Sherman, “Application of the convolution theorem to Rayleigh’s integral formulas,” *J. Opt. Soc. Am.*, vol. 57, pp. 546–547, 1967.
- [65] E. Lalor, “Conditions for the validity of the angular spectrum of plane waves,” *J. Opt. Soc. Am.*, vol. 58, pp. 1235–1237, 1968.
- [66] L. Onural, A. Gotchev, H. M. Ozaktas, and E. Stoykova, “A survey of signal processing problems and tools in holographic three-dimensional television,” *IEEE T. Circ. and Syst. Vid.*, vol. 17, pp. 1631–1646, 2007.
- [67] L. Onural, “Some mathematical properties of the uniformly sampled quadratic phase function and associated issues in digital fresnel diffraction simulation,” *Opt. Eng.*, vol. 43, pp. 2557–2563, 2004.
- [68] E. C. Tam, “Smart electro-optical zoom lens,” *Opt. Lett.*, vol. 17, pp. 369–371, 1992.
- [69] J. Jahns and S. J. Walker, “Two-dimensional array of diffractive microlenses fabricated by thin film deposition,” *Appl. Optics*, vol. 29, pp. 931–936, 1990.
- [70] M. S. Millan, J. Oton, and E. Perez-Cabre, “Chromatic compensation of programmable fresnel lenses,” *Opt. Express*, vol. 14, pp. 6226–6242, 2006.
- [71] V. Laude, “Twiste-nematic liquid-crystal pixelated active lens,” *Opt. Commun.*, vol. 153, pp. 134–152, 1998.

- [72] L. Rayleigh, “On copying diffraction-gratings, and on some phenomena connected therewith,” *Philos. Mag.*, vol. 11, pp. 196–205, 1881.
- [73] A. Ö. Yöntem and L. Onural, “Integral imaging based 3d display of holographic data,” *Opt. Express*, vol. 20, pp. 24175–24195, 2012.
- [74] M. Kovachev, R. Ilieva, P. Benzie, G. B. Esmer, L. Onural, J. Watson, and T. Reyhan, *Holographic 3DTV displays using spatial light modulators*, in *Three-Dimensional Television-Capture, Transmission, Display*, H. Ozaktas, and L. Onural, eds., pp. 529–555. Springer, 2008.
- [75] L. Onural, F. Yaraş, and H. Kang, “Digital holographic three-dimensional video displays,” *P. SPIE*, vol. 99, pp. 576–589, 2011.
- [76] F. Yaraş, H. Kang, and L. Onural, “Circular holographic video display system,” *Opt. Express*, vol. 19, pp. 9147–9156, 2011.
- [77] A. V. Oppenheim, A. S. Willsky, and S. H. Nawab, *Signals and Systems Second Edition*. New York: Prentice-Hall, 1997.

Appendix A

Evaluation of Eq. (2.16)

The convolution of the function inside the curly brackets and $h_z(x)$ in Eq. (2.16) can be written as

$$\int \left[p(\eta)l^Q(\eta) * \sum_r \delta(\eta - rx_0) \right] \sum_n \delta(\eta - nX)h_z(x - \eta)d\eta. \quad (\text{A-1})$$

Above equation can be rewritten as,

$$\sum_r \int p(\eta - rx_0)l^Q(\eta - rx_0) \sum_n \delta(\eta - nX)h_z(x - \eta)d\eta \quad (\text{A-2})$$

and by a change of variables as $\eta = \sigma + rx_0$ we get

$$\begin{aligned} & \sum_r \int p(\sigma)l^Q(\sigma) \sum_n \delta(\sigma + rx_0 - nX)h_z(x - \sigma - rx_0)d\sigma \\ = & \sum_r \int p(\sigma)l^Q(\sigma) \sum_n \delta(\sigma + rx_0 - nX)h_z(x) \exp[-j2\chi x(\sigma + rx_0)] \\ & \exp[j\chi(\sigma + rx_0)^2]d\sigma. \end{aligned} \quad (\text{A-3})$$

where $\chi = \frac{\pi}{\lambda_z}$. Notice that, x_0 in the impulse train is equal to NX where N is an integer. Therefore $\sum_n \delta(\sigma + rx_0 - nX) = \sum_n \delta(\sigma - nX)$ for each r . Further

manipulations give

$$\begin{aligned}
& \sum_r \int p(\sigma) l^Q(\sigma) \sum_n \delta(\sigma - nX) h_z(x) \exp(-j2\chi x\sigma) \exp(-j2\chi r x_0) \\
& \quad \hbar_\chi(\sigma) \exp(j2\chi r x_0 \sigma) \exp(j\chi r^2 x_0^2) d\sigma \\
= & \sum_k a_k \int p(\sigma) \hbar_{-\gamma_k}(\sigma) \hbar_\chi(\sigma) \sum_n \delta(\sigma - nX) \sum_r h_z(x - r x_0) \exp(j2\chi r x_0 \sigma) \\
& \quad \exp(-j2\pi \frac{x}{\lambda z} \sigma) d\sigma \tag{A-4}
\end{aligned}$$

where we used Eq. (2.12) for $l^Q(\cdot)$. The summation over k is due to the response of multiple lenses with focal lengths f_k . Above equation can be recognized as a Fourier transform, of a product of functions, from variable σ to the spatial domain variable $\frac{x}{\lambda z}$. The Fourier transform can be written as

$$\mathcal{F}_{\sigma \rightarrow \frac{x}{\lambda z}} \left\{ \sum_k a_k p(\sigma) \hbar_{-\gamma_k}(\sigma) \hbar_\chi(\sigma) \sum_n \delta(\sigma - nX) \sum_r h_z(x - r x_0) \exp(j2\chi r x_0 \sigma) \right\} \tag{A-5}$$

where we define the Fourier transform and the inverse Fourier transform as

$$\begin{aligned}
F(\nu) = \mathcal{F}_{x \rightarrow \nu} \{f(x)\} &= \int_{-\infty}^{\infty} f(x) \exp(-j2\pi \nu x) dx \\
f(x) = \mathcal{F}_{\nu \rightarrow x}^{-1} \{F(\nu)\} &= \int_{-\infty}^{\infty} F(\nu) \exp(j2\pi \nu x) d\nu
\end{aligned}$$

Multiplications of the functions will result in convolutions after the Fourier transformation and we will get

$$\begin{aligned}
\sum_k a_k \left\{ P\left(\frac{x}{\lambda z}\right) * \mathcal{H}_{-\gamma_k}\left(\frac{x}{\lambda z}\right) * \mathcal{H}_\chi\left(\frac{x}{\lambda z}\right) * \frac{\lambda z}{X} \sum_n \delta\left(x - n \frac{\lambda z}{X}\right) \right. \\
\left. * \sum_r h_z(x - r x_0) \delta(x - r x_0) \right\}
\end{aligned}$$

in the spatial domain. We are interested in those cases where $\chi = \gamma_k$ that is $z = f_k$ in above equation. Thus we obtain,

$$\begin{aligned}
\sum_k a_k \left\{ P\left(\frac{x}{\lambda f_k}\right) * \mathcal{H}_{-\gamma_k}\left(\frac{x}{\lambda f_k}\right) * \mathcal{H}_{\gamma_k}\left(\frac{x}{\lambda f_k}\right) \right. \\
\left. * \frac{\lambda f_k}{X} \sum_n \delta\left(x - n \frac{\lambda f_k}{X}\right) * \sum_r h_{f_k}(x - r x_0) \delta(x - r x_0) \right\}
\end{aligned}$$

where the convolution $\mathcal{H}_{-\gamma_k} \left(\frac{x}{\lambda f_k} \right) * \mathcal{H}_{\gamma_k} \left(\frac{x}{\lambda f_k} \right) = 1$. The final result is thus,

$$q(x) = \sum_k \left\{ \left[P \left(\frac{x}{\lambda f_k} \right) * \frac{x_0}{k} \sum_n \delta \left(x - \frac{n}{k} x_0 \right) \right] * \left[\sum_r c_{k,r}(x) \delta(x - r x_0) \right] \right\} * s(x) \quad (\text{A-6})$$

where the constants are given as $\frac{\lambda f_k}{X} = \frac{NX}{k} = \frac{x_0}{k}$ and $c_{k,r}(x) = a_k h_{f_k}(x - r x_0)$.

Appendix B

Evaluation of Eq. (3.6)

If we expand the quadratic phase function in Eq. (3.6), we will get,

$$q_i(x) = \left\{ h_g(x) \sum_n h_{D,i}^{LP}[n] LA_D[n] \hbar_\beta(nX) \exp(-j2\beta xnX) \right\} * s(x)$$

where the summation is the so called discrete time Fourier transform [77] of the function

$$u[n] = h_{D,i}^{LP}[n] LA_D[n] \hbar_\beta(nX)$$

where $u[n]$ is the discrete version of $u_c(x) = h_{z_i}^{LP}(x) LA(x) h_g(x)$ for $x = nX$, n is an integer variable in $(-\infty, \infty)$. Using the relation between the continuous time Fourier transform $F_c(\nu)$ of the continuous function $f_c(x)$ and the discrete time Fourier transform $F(\hat{\nu})$ of the discrete function $f[n] = f_c(nX)$, that is given by

$$F(\hat{\nu})|_{\hat{\nu}=\nu X} = F_c(\nu) * \frac{1}{X} \sum_k \delta(\nu - k \frac{1}{X}) \quad (\text{B-1})$$

where $F(\hat{\nu}) = \sum_n f[n] \exp(-j\hat{\nu}n)$ and $F_c(\nu) = \int_{-\infty}^{\infty} f_c(\eta) \exp(-j2\pi\eta\nu) d\eta$. We can rewrite $q_i(x)$ as

$$q_i(x) = \left[h_g(x) U_c \left(\frac{x}{\lambda g} \right) \right] * x_g \sum_n \delta(x - nx_g) * s(x)$$

where $x_g = \frac{\lambda g}{X}$. The scaled impulse train is due to sampling of the lenslets that causes multiple diffraction orders. Up to this point we can explain the effect

of sampled lenslets at the output plane. However, we need to further analyze $\left[h_g(x)U_c\left(\frac{x}{\lambda g}\right) \right]$ to observe the effects of quantization. To do that, we first assume that the tails of the replicas of the continuous Fourier transform of the function is small so that they introduce negligible aliasing when they are summed. This is in fact true, because while the light travels from and through the physical optical elements, it does not spread too much in space. Thus, light cannot extend to very high angles. It is usually confined into a certain region. This can be seen as an inherent low pass filtering of the optical elements. Furthermore, the pixelated physical optical elements will diffract light into higher orders while the modulated light propagates. So, each replica will spread to a limited region and will be separated from each other by a certain distance. These two properties will result in reducing the aliasing components. Using the Fourier transform relations given above in Eq. (B-1), we expand $h_g(x)U_c\left(\frac{x}{\lambda g}\right)$ as

$$\begin{aligned}
h_g(x)U_c\left(\frac{x}{\lambda g}\right) &= h_\beta(x) \int h_{z_i}^{LP}(\eta) LA(\eta) \tilde{h}_\beta(\eta) \exp(-j2\pi \frac{x}{\lambda g} \eta) d\eta \\
&= h_g(x) \int h_{z_i}^{LP}(\eta) \left[p(\eta) l^Q(\eta) * \sum_r \delta(\eta - rx_0) \right] \\
&\quad \tilde{h}_\beta(\eta) \exp(-j2\pi \frac{x}{\lambda g} \eta) d\eta \\
&= h_g(x) \int [t_i h_{z_i}(\eta - x_i) V(\eta - x_i)] \left[\sum_r p(\eta - rx_0) l^Q(\eta - rx_0) \right] \\
&\quad \tilde{h}_\beta(\eta) \exp(-j2\pi \frac{x}{\lambda g} \eta) d\eta \\
&= h_g(x) \int t_i h_{z_i}(\eta) \exp(-j2\alpha_i \eta x_i) \exp(j\alpha_i x_i^2) V(\eta - x_i) \\
&\quad \left[\sum_r p(\eta - rx_0) l^Q(\eta - rx_0) \right] \tilde{h}_\beta(\eta) \exp(-j2\pi \frac{x}{\lambda g} \eta) d\eta.
\end{aligned}$$

We make a change of variables $\eta = \sigma + rx_0$ as in Appendix A to get

$$\begin{aligned}
h_g(x)U_c\left(\frac{x}{\lambda g}\right) &= \sum_r h_g(x) t_i \int_\sigma h_{z_i}(\sigma + rx_0) \exp[-j2\alpha_i(\sigma + rx_0)x_i] \exp(j\alpha_i x_i^2) \\
&\quad p(\sigma) l^Q(\sigma) [\tilde{h}_\beta(\sigma) \exp(j2\beta\sigma rx_0) \exp(j\beta r^2 x_0^2)] \\
&\quad \exp(-j2\beta x r x_0) \exp(-j2\pi \frac{x}{\lambda g} \sigma) V(\sigma + rx_0 - x_i) d\sigma
\end{aligned}$$

and then we expand some of the quadratic phase functions

$$\begin{aligned}
h_g(x)U_c\left(\frac{x}{\lambda g}\right) &= \sum_r h_g(x)t_i \int \frac{1}{\sqrt{j\lambda z_i}} \exp\left(-j\frac{2\pi}{\lambda}z_i\right) \hbar_{\alpha_i}(\sigma) \exp(j2\alpha_i\sigma r x_0) \\
&\quad \exp(j\alpha_i r^2 x_0^2) \exp(-j2\alpha_i\sigma x_i) \exp(-j2\alpha_i x_i r x_0) \\
&\quad \exp(j\alpha_i x_i^2) p(\sigma) l^Q(\sigma) \hbar_g(\sigma) \exp(j2\beta\sigma r x_0) \exp(j\beta r^2 x_0^2) \\
&\quad \exp(-j2\beta x r x_0) \exp(-j2\pi\frac{x}{\lambda g}\sigma) V(\sigma + r x_0 - x_i) d\sigma
\end{aligned}$$

Notice that the terms $h_g(x) \exp(-j2\beta x r x_0) \exp(j\beta r^2 x_0^2)$ can be rearranged as $h_g(x - r x_0)$. And also the terms

$$\frac{1}{\sqrt{j\lambda z_i}} \exp\left(-j\frac{2\pi}{\lambda}z_i\right) \exp(j\alpha_i r^2 x_0^2) \exp(-j2\alpha_i x_i r x_0) \exp(j\alpha_i x_i^2)$$

can be put into the compact form $h_{z_i}(x_i - r x_0)$. Rearranging the remaining exponential terms and gathering the summation terms over the variable r we finally get

$$\begin{aligned}
h_g(x)U_c\left(\frac{x}{\lambda g}\right) &= \int \hbar_{\theta_i}(\sigma) p(\sigma) l^Q(\sigma) \left[\sum_r c(x) V(\sigma + r x_0 - x_i) \right. \\
&\quad \left. \times \exp[j2\sigma(\theta_i r x_0 - \alpha_i x_i)] \right] \exp(-j2\pi\frac{x}{\lambda g}\sigma) d\sigma \quad (\text{B-2})
\end{aligned}$$

where $\theta_i = \beta + \alpha_i = -\frac{\pi}{\lambda} \frac{\Delta z_i}{d(d+\Delta z_i)}$ and $c(x) = h_g(x - r x_0) t_i h_{z_i}(x_i - r x_0)$. The above equation can be rewritten as

$$\begin{aligned}
\mathcal{F}_{\sigma \rightarrow \frac{x}{\lambda g}} &\left\{ \left[\hbar_{\theta_i}(\sigma) p(\sigma) \right] \left[\sum_k a_k \hbar_{-\gamma_k}(\sigma) \right] \right. \\
&\quad \left. \times \left[\sum_r c(x) V(\sigma + r x_0 - x_i) \exp[j2\sigma(\theta_i r x_0 - \alpha_i x_i)] \right] \right\} \cdot (\text{B-3})
\end{aligned}$$

Since the terms inside the right brackets are multiplied, the result of the Fourier transform will be convolution of corresponding Fourier transformed terms in the scaled spatial domain.

The Fourier transform of the last term is a weighted impulse train which gives the perfect mapping (imaging) at locations $\left(1 + \frac{g}{z_i}\right) r x_0 + \frac{g}{z_i} x_i$ of the input point to multiple output points. This would be the imaging of a lenslet array

consisting of perfect thin lenses. However, because of the low pass filtering caused by the pixel function at the input, this last term gives blurred spots. The Fourier transform of the function inside the last right brackets is given as

$$\Upsilon_i(x) = \sum_r c(x) \left\{ \left\{ v \left(\frac{x}{\lambda g} \right) \exp[j2\beta(x_i - rx_0)x] \right\} * \delta \left[x - \left(1 + \frac{g}{z_i} \right) rx_0 + \frac{g}{z_i} x_i \right] \right\} \quad (\text{B-4})$$

where we obtain $v \left(\frac{x}{\lambda g} \right) = (j\lambda z_i) \tilde{h}_\beta \left(\sqrt{\frac{z_i}{g}} x \right) s \left(-\frac{z_i}{g} x \right)$ by using the Fourier transform property, $\mathcal{H}_{-\alpha_i} \left(\frac{x}{\lambda g} \right) = \left(j \frac{\pi}{\alpha_i} \right)^{1/2} \exp \left(j \frac{(2\pi x / (\lambda g))^2}{4\alpha_i} \right) = (j\lambda z_i)^{1/2} \tilde{h}_\beta \left(\sqrt{\frac{z_i}{g}} x \right)$, for quadratic phase functions given in [67]. The Fourier transform of the second term $\sum_k a_k \mathcal{H}_{-\gamma_k} \left(\frac{x}{\lambda g} \right)$ is introduced because of the multiple focal point property of the lenslets. In fact, this is another artefact term at the main image plane caused by the smaller images formed at image planes related to other focal distances, f/k , of higher-order lenslets. The Fourier transform of the first term will be $P_i \left(\frac{x}{\lambda g} \right) = P \left(\frac{x}{\lambda g} \right) * \mathcal{H}_{\theta_i} \left(\frac{x}{\lambda g} \right)$ is the generalized pupil function which takes blurring due to different depths of the point sources at the input plane into account. The function $\mathcal{H}_{\theta_i} \left(\frac{x}{\lambda g} \right)$ is responsible for the defocussing. $P \left(\frac{x}{\lambda g} \right)$ is the Fourier transform of the pupil function. This function is also a limiting factor for the extent of $q_i(x)$. Finally, arranging all terms we can write $q_i(x)$ as

$$q_i(x) = P_i \left(\frac{x}{\lambda g} \right) * s(x) * \left[\sum_k a_k \mathcal{H}_{-\gamma_k} \left(\frac{x}{\lambda g} \right) \right] * x_g \sum_n \delta(x - nx_g) * \Upsilon_i(x) \cdot \quad (\text{B-5})$$

Appendix C

Derivation of 1D impulse response of the LSI system that represents free-space propagation between two parallel planes

Suppose that we have a 2D input function $f(x, y)$. We can find the response $g(x, y)$ of the system $h_z^{2D}(x, y)$ to $f(x, y)$ at a certain distance z by simply,

$$\begin{aligned} g(x, y) &= f(x, y) ** h_z^{2D}(x, y) \\ &= \int \int f(\zeta, \eta) h_z^{2D}(x - \zeta, y - \eta) d\zeta d\eta \end{aligned}$$

Now, assume that we only have a variation in the x direction in the input field, but there is no variation along y . Thus, above equation becomes

$$\begin{aligned} g(x, y) &= \int \left[\int c f(\zeta) h_z^{2D}(x - \zeta, \eta) d\eta \right] d\zeta \\ &= \int c f(\zeta) q(x - \zeta) d\zeta \end{aligned}$$

where $q(x - \zeta) = \int h_z^{2D}(x - \zeta, \eta) d\eta$. Substituting the 2D kernel to $q(x - \zeta)$ we obtain,

$$\begin{aligned} q(x - \zeta) &= \frac{1}{j\lambda z} \exp\left(j\frac{2\pi}{\lambda}z\right) \int \exp\left\{j\frac{\pi}{\lambda z} [(x - \zeta)^2 + \eta^2]\right\} d\eta \\ &= \frac{1}{j\lambda z} \exp\left(j\frac{2\pi}{\lambda}z\right) \exp\left[j\frac{\pi}{\lambda z} (x - \zeta)^2\right] \int \exp\left(j\frac{\pi}{\lambda z} \eta^2\right) d\eta. \end{aligned}$$

The integral can be calculated as by $\int_{-\infty}^{\infty} \exp(jkx^2) dx = \frac{\sqrt{\pi}}{\sqrt{-jk}}$. If we substitute $\frac{\pi}{\lambda z}$ for k , we will get the result of the integral as $\sqrt{j\lambda z}$. Thus, we will obtain $q(x - \zeta) = \frac{1}{\sqrt{j\lambda z}} \exp(j\frac{2\pi}{\lambda}z) \exp\left[j\frac{\pi}{\lambda z} (x - \zeta)^2\right]$ and therefore, 1D calculation kernel becomes $h_z(x) = \frac{1}{\sqrt{j\lambda z}} \exp(j\frac{2\pi}{\lambda}z) \exp\left(j\frac{\pi}{\lambda z} x^2\right)$.